POLYMER FUNCTIONALIZED SINGLE-WALLED CARBON NANOTUBE COMPOSITES AND SEMI-FLUORINATED QUATERNARY AMMONIUM POLYMER COLLOIDS AND COATINGS

By

ABHIJIT PAUL

Bachelor of Science in Chemistry
Assam University
Silchar, Assam
2001

Master of Science in Polymer Science
Tezpur University
Tezpur, Assam
2003

Submitted to the Faculty of the
Graduate College of the
Oklahoma State University
in partial fulfillment of
the requirements for
the Degree of
DOCTOR OF PHILOSOPHY
July, 2012

POLYMER FUNCTIONALIZED SINGLE-WALLED

CARBON NANOTUBE COMPOSITES

AND

SEMI-FLUORINATED QUATERNARY AMMONIUM

POLYMER COLLOIDS AND COATINGS

Dissertation Approved:

Dr. Warren T. Ford

Dissertation Adviser

Dr. Kenneth D. Berlin

Dr. Jeffery L. White

Dr. Kevin D. Ausman

Dr. James P. Wicksted

Dr. Sheryl A. Tucker

Dean of the Graduate College

PREFACE

In my Ph.D. research I have studied single-walled carbon nanotube (SWCNT) polymer composites that potentially have unique combination of excellent mechanical strength, electrical conductivity, and thermal conductivity and polymeric coatings to repel or destroy the toxic insecticide Paraoxon.

The surface of SWCNT was modified with polystyrene (PS) and poly(methyl methacrylate) (PMMA, the polymer of Plexiglas), and was mixed with chemically identical host polymers to prepare SWCNT-filled electrically conductive plastics. In principle, at the scale of a 1 nanometer (1 nm = 1 billionth of a meter) diameter of a single SWCNT or a few nm diameter of a small bundle of SWCNT, the interfacial area of contact between the SWCNT and the PS or PMMA is much greater than with the much larger conventional carbon fiber or glass fiber composites. The large interfacial area of SWNT-polymer composites should increase the electrical conductivity, thermal conductivity, and mechanical strength with a much smaller amount of the SWCNT filler. The prepared nanocomposite materials have potential applications as sensors, electrostatic dissipative materials, mechanical memory elements, and shields to prevent electromagnetic interference. In practice, my results were as follows: (a) The glass transition temperature and modulus (stiffness) of the neat PMMA increased with SWCNT loadings when chain lengths of the grafted PMMA were longer than free PMMA chains. (b) For the same set of samples, electrical conductivity of PMMA

increased to 10^6 times of unfilled PMMA at 0.25 wt% of SWCNT. (c) In case of PS nanocomposites, glass transition temperature increased up to 6 wt% of SWCNT and remained constant with further addition of SWCNT. (d) The electrical conductivity of PS nanocomposites did not increase with SWCNT additions due of the thick insulating PS layer on the tube surface. (e) All SWCNT were optically active after oxidative treatment and polymer functionalizations. This work has generated an understanding of how the length of the attached polymer to SWCNT impacts their miscibility in the host polymer. The results of this study will assist scientists and engineers to develop high-performance nanocomposites.

In my second project I prepared nanosized polymeric particles which can either repel or detoxify Paraoxon into non-toxic products. Previous research had shown that colloidal catalyst particles related to those in water-based paints can destroy Paraoxon in water. In my research I coated the surface of the particles with a fluoropolymer for the purpose of preventing Paraoxon from penetrating the particles and coated the particles on a glass surface. This work might lead to self-cleaning coatings for interior and exterior decorative purposes. Decontamination, aimed at eliminating the hazard of chemical warfare agents (CWA), is essential on the battlefield, in research laboratories, in chemical agent production and storage places, and in CWA destruction sites. Polymeric particles with highly fluorous surface had water and toxic chemical repellant properties which either repelled the Paraoxon or detoxified the Paraoxon into non-toxic products, but cannot do both. This work is geared towards the advancement of environmental friendly preparation of toxic chemical decontaminants.

TABLE OF CONTENTS

Chapter Page

CHAPTER II POLY(STYRENE) FUNCTIONALIZED SINGLE-WALLED-CARBON NANOTUBE POLYMER COMPOSITES

CHAPTER III POLY(METHYL METHACRYLATE) FUNCTIONALIZED SINGLE-WALLED CARBON NANOTUBE-POLYMER COMPOSITES

LIST OF TABLES

Table Page

CHAPTER I

CHAPTER II

CHAPTER III

CHAPTER IV

LIST OF FIGURES

Figure Page

CHAPTER I

CHAPTER II

CHAPTER III

LIST OF SCHEMES

Scheme Page

CHAPTER II

CHAPTER III

CHAPTER IV

CHAPTER I

SINGLE-WALLED CARBON NANOTUBES: FUNCTIONALIZATION, CHARACTERIZATION, AND COMPOSITE PROPERTIES

1.1 Motivation

Carbon occurs in all organic and in many inorganic compounds. The name 'carbon' was derived from the Latin word carbo means "charcoal". There are three naturally occurring allotropes of carbon known to exist on the earth: amorphous, graphite, and diamond. Since, 1980's some other forms of carbon have been discovered with unique properties, and have an exceptional potential for many industrial applications and advanced technologies. In 1985, a group of researchers led by Richard Smalley and Robert Curl of Rice University, Houston and Harry Kroto of the University of Sussex in England discovered a new geometrical form of carbon molecule (C_{60}) called "buckerminsterfullerene" or in short "buckyball".[1] After the discovery of C_{60} molecules, other similar allotropes of carbon molecules C_{36}, C_{70}, C_{76}, and C_{84} were observed and called fullerenes. C_{60} consists of six and five-membered rings and has the geometry of a soccer ball. Carbon fibers with stacks of carbon layers, parallel to the fiber axis, and arranged in concentric sheets of carbon layers were reported by Endo[2,3,4] *et al.* prior to

Iijima's report on the synthesis of multiple concentric tubes in 1991.[5] Iijima called those cylindrical tubes multi-walled carbon nanotubes (MWCNT). Two years later, Iijima and Bethune discovered single-walled carbon nanotubes (SWCNT).[6,7] An individual SWCNT can be considered as a graphene sheet rolled into a tube with two ends capped with hemispherical fullerenes. This rolling gives rise to a large number of potential diameters and chiralities of SWCNT. The atomic structures of fullerene, multi-walled carbon nanotube, and single-walled carbon nanotube are shown in Figure 1.

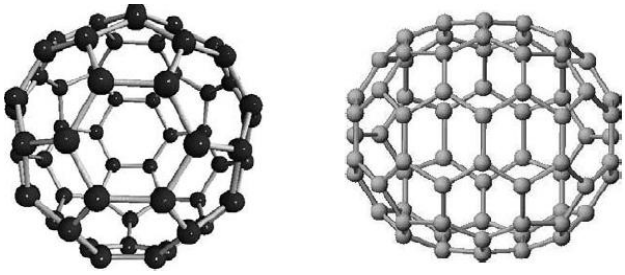

C_{60} C_{70}

(a) Models of the first fullerenes discovered, C_{60} and C_{70}

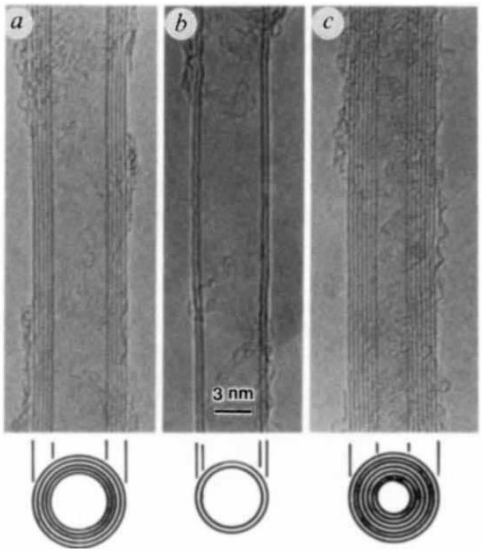

(b) Multi-walled carbon nanotube

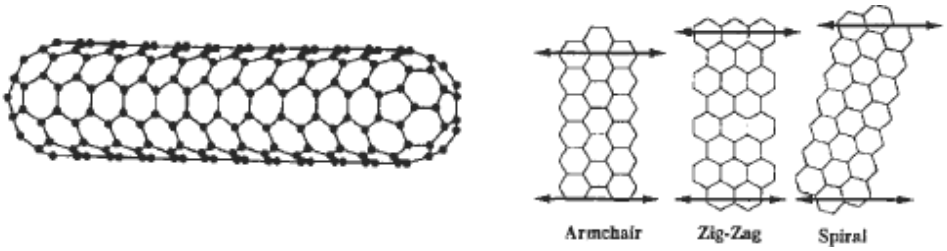

(c) Single-walled carbon nanotube

Figure 1. Structures of fullerenes and carbon nanotubes (single and multi walled). Figure (a) is copied from the reference 18, (b) is copied from the reference 5, and (c) is copied from Burchell, T. D., Ed. *Carbon Materials for Advanced Technologies*; Elsevier Science Ltd: Chicester, U.K., 1999.

SWCNT have exceptional electrical, mechanical, thermal, and optical properties which find applications in molecular electronics, optoelectronics, field emission devices, batteries, catalysis, gas storage, sensors, and polymer nanocomposites.[8] SWCNT possess extraordinary mechanical properties including high stiffness and high specific strength. The specific strength, also called strength-to-weight ratio, of SWCNT is 50 times higher than steel, which means that the materials made up of SWCNT are stronger and lighter in weight. The Young's modulus for an individual SWCNT is from 1.06 to 1.25 TPa[9,10,11] and for ropes 1 TPa,[12] which are 5 times higher than steel (200 GPa). The tensile strength of MWCNT ropes is between 11 to 63 GPa[13] whereas for an individual SWCNT the value is 22.2 ± 2.2 GPa and for SWCNT ropes tensile strength reaches 3.6 ± 0.4 GPa.[14] The aspect ratio of carbon nanotubes is usually more than 100 and even goes up to 1000. The length of a SWCNT is around 1 μm and the diameter ranges from 0.4 to >3 nm whereas the length of MWCNT varies from ~1.4 to at least 100 μm.[15]

Carbon nanotubes can be either metallic or semiconducting. Therefore, one can envision nanotube to act as a high local current carrying interconnects for various applications in electronic devices. SWCNT possess thermal stability up to 2800 ^{o}C in vacuum and < 500 ^{o}C in air. The theoretical electrical conductivity is 1000 times higher than copper,[16] and theoretical thermal conductivity is 16 times higher than the copper.[17] Thus, these exceptional physical, electrical, thermal and mechanical properties have made SWCNT a promising reinforcement filler to prepare next generation high performance nanocomposites and to explore these materials for other potential applications.

1.2 Structure of Carbon Nanotubes. Carbon nanotubes (CNT) are considered to be building blocks to nanotechnology. They are made up of pure carbon bonds. Graphite and diamond are examples of sp^2 and sp^3 hybridization.[18] The structures of graphite and diamond are shown in Figure 2.

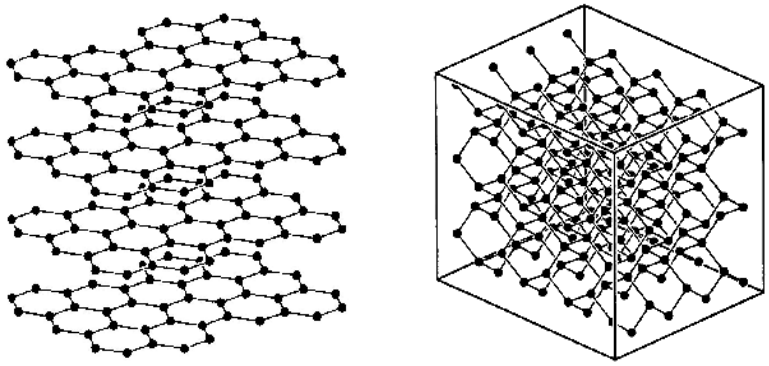

Figure 2. Structures of graphite and diamond.
(The figure is copied from Drexler, E.; Peterson, C.; Pergamit, G. Unbounding the future: the nanotechnology revolution: New York, 1991).

In sp^2 hybridization, one *s* orbital and two *p* orbitals are involved in the formation of a bond. The bond is strong in a plane but weak between planes. When such bonds come together, they form 6-fold honeycomb like structure in a single plane. Graphite is an example of an array of such single planes called graphene, which are placed layer-by-layer. In each layer, the carbon atoms are arranged in a hexagonal lattice, and the distance between planes is 0.36 nm. The graphite has a planar structure. On the other hand, when such planes are wrapped together, they form cylindrical shape tubes, called carbon nanotubes, which consist of 6-membered rings at the walls and 5-membered rings joined

together with 6-membered rings at the caps. Figure 3 shows the construction of a carbon nanotube.

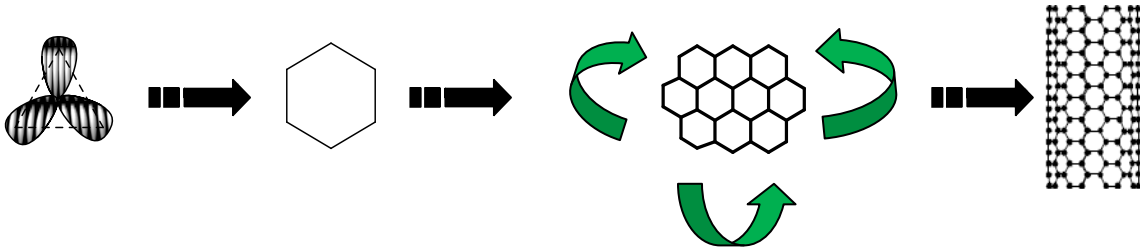

Figure 3. Schematic representation of carbon nanotube formation.

The fundamental structures of carbon nanotube can be illustrated in terms of chirality or helicity which are defined by chiral vector, C_h, and chiral angle θ shown in Figure 4. The chiral vector C_h defines the circumference on the nanotube connecting two equivalent carbon atoms, $C_h = n\hat{a}_1 + m\hat{a}_2$, where n and m are integers, called indexes whereas $\hat{a}_1$ and $\hat{a}_2$ are the two basis vectors of graphite. The chiral angle is $\theta = \tan^{-1}[\sqrt{3}(n/(2m+n)]$.

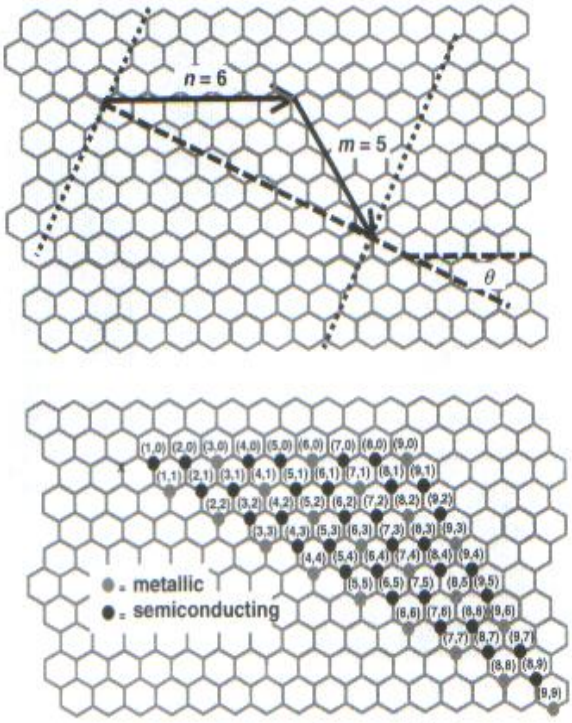

Figure 4. Graphene sheet labeled with the integers *n* and *m* to show a tube as either metallic or semiconducting. The figure is copied from the reference 74.

On the basis of electronic properties, carbon nanotube can be separated into three different classes: armchair ($n = m$, $\theta = 30^o$), zigzag ($m = 0$, $n > 0$, $\theta = 0^o$), and chiral ($0 < m < n$, $0 < \theta < 30^o$) shown in Figure 5. The diameter, chiral angle, and the type of nanotube are determined by the values of *n* and *m*.[19] Armchair carbon nanotubes are metallic in nature, a degenerate semimetallic with zero band gap. On the other hand, zigzag and chiral nanotubes are semimetallic with a finite band gap if $n - m/3 = i$, where *i* is an integer and $n \neq m$. Zigzag nanotubes are more conductive than chiral nanotubes.

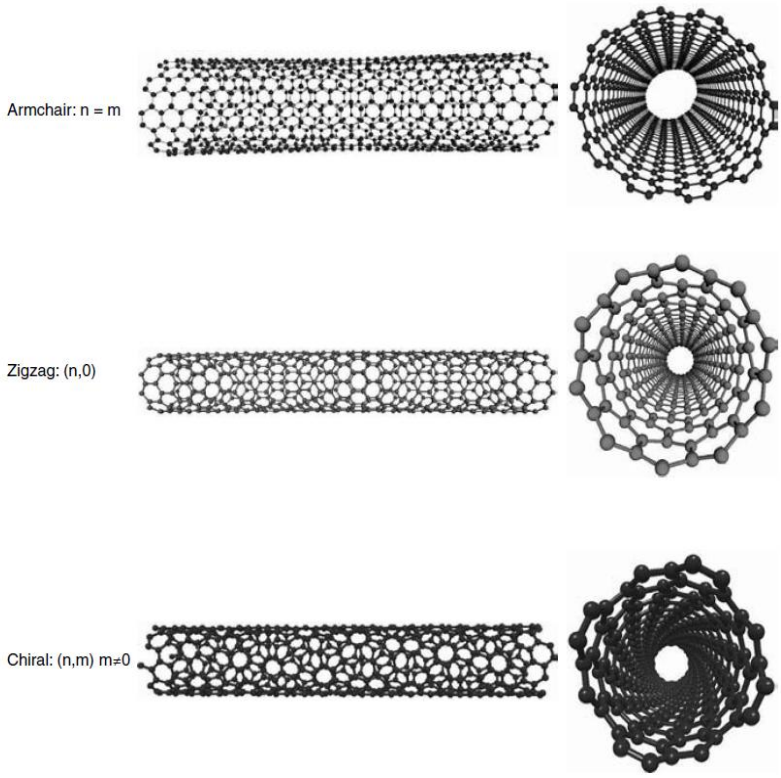

Figure 5. Three types of SWCNT on the basis of integers (*n*, *m*). The figure is copied from the reference 18.

1.3 Properties of Carbon Nanotubes. Carbon nanotube possesses exceptional properties due to its structure. However, due to the small size and different types of nanotubes available in a sample, it is difficult to estimate the properties of an individual nanotube. Hence, most of the initial work on the mechanical properties of nanotubes has come from the computational work. The Young's modulus, *E*, of CNT, computed by various researchers from molecular mechanics simulations and experimental data varied from 0.5 to 5 TPa.[20] For MWCNT, the interwall distance is close to the interlayer distance between the graphite layers was approximately 0.34 nm. Therefore, considering the wall thickness of 0.34 nm for SWCNT, values of Young's modulus, *E*, were estimated between 1 TPa[21]

and 1.3 TPa,[22] which correspond to the value of a flat graphene sheet within the same theoretical framework. Computational studies were based on the assumption that the nanotube samples are defect free, but in actual case nanotubes contain a significant numbers of defects. The values of Young's modulus, *E,* predicted by computational studies for individual nanotubes and nanotube bundles were validated by various experimental techniques summarized in Table 1. The Young's modulus for an individual nanotube of 1 TPa and density of 1.3-1.5 g cm^{-3} have made SWCNT a unique nanoscale filler for preparing strong and light weight nanocomposites. Young's modulus depends on many factors such as diameter of the nanotube, helicity, defects, and the method by which the nanotubes are prepared. As the diameter decreases, the modulus decreases due to the increase in the bond strain. Helicity affects the modulus as well. Due to bond strength, for example, a zigzag tube is stiffer than an armchair nanotube. Carbon nanotubes prepared by chemical vapor deposition have lower Young's modulus than arc discharge and/or laser ablated tubes because the former has a higher numbers of defects.

Table 1. Young's Modulus Calculated From Different Experimental Data

nanotube type	test method	Young's modulus (TPa)	deviation (TPa)	reference
MWCNT	Amplitude of intrinsic thermal vibration within STEM	1.80	1.4	23
MWCNT	Beam bending via AFM	1.28	0.6	24
SWCNT	Amplitude of intrinsic thermal vibration within STEM	1.25	0.5	9
SWCNT	Raman Spectroscopy	2.83-3.58	na[a]	25
MWCNT	Raman Spectroscopy	1.72-2.44	na	25
MWCNT	3 point bending with AFM	1.28	0.59	26
MWCNT Bundle	3 point bending with AFM	0.81	0.41	26
SWCNT	3 point bending with AFM	1.2	Na	10
SWCNT	Raman Spectroscopy	0.78-2.34	Na	27
MWCNT	Tension mode with AFM	0.27-0.95	Na	28
SWCNT Bundle/Ropes	Tension mode with AFM	0.32-1.47	Na	29

[a]Not available

Molecular mechanics and molecular dynamics studies reveal the fracture strain of CNT between 10 and 15% with corresponding fracture stresses from 65 to 93 GPa.[30] The tensile strength of the individual SWCNT is estimated to be 52 GPa whereas the maximum tensile strain of SWCNT bundles is approximately 5.3%.[29] For MWCNT, the outer tube breaks followed by removal of inner tubes by "sword-in-sheath" mechanism. The tensile strength of the outer shell of MWCNT is estimated to be 11 to 63 GPa with

Young's modulus ranging from ~270 to 970 GPa at the maximum strain at failure of 12%.[28] In MWCNT, the outer layer initially carries the load because of the way the ends of the MWCNT section are attached and the weak interlayer interactions. It is the outermost layer that breaks, followed by pullout. In some cases, the inner-layer pullout could extend all the way to the end of the MWCNT where the nested layers terminate at the cap. Table 2 compares physical and mechanical properties of various fillers used to prepare polymer composites.[31] The mechanical properties of CNT stand out quite impressive as a reinforcement material for polymer nanocomposites compared to other fillers. However, many issues need to be resolved and understood to utilize the full potential of these materials.

Table 2. Physical and Mechanical Properties of Various Reinforcement Fillers[31]

filler	diameter (μm)	density (g/cm^3)	tensile strength (GPa)	Young's modulus (GPa)
Carbon fiber	7	1.33-1.7	2.4-3.1	120-170
Glass (E and S-2)	14	2.5	3.4-4.6	90
Aramid (Kevlar)	12	1.44	3.4-4.1	83-186
Boron	100-140	2.5	3.5	400
Quartz	9	2.2	2.8	70
SiC	10-20	2.3	2.8	190
CNT	0.001-0.1	1.3-1.4	50-200	1000

CNT can be metallic or semiconducting depending on the chiral vector. This difference in conductivity of nanotubes is due to the molecular structure that results in different band structures and hence different band gaps. Quantum mechanical studies reveal that the conductance to resistance ratio does not depend on the nanotube length. Nevertheless, due to differences in chirality and the amount of defects, the electrical conductivities of SWCNT and MWCNT are quite diverse. An individual MWCNT comprised of metallic and semiconducting nanotubes has conductivities between 2×10^7 and 8×10^5 S/m with a maximum band gap of 0.3 eV.[32,33] Conductivity measurements on an individual metallic SWCNT gave a value approximately 5×10^7 S/m ($R \approx 32$ KΩ at 290 K),[34] whereas bundles of SWCNT were on the lower side of MWCNT conductivity values.[35]

The thermal conductivity of MWCNT at room temperature was measured to be 2000 W/mK[36] and 3000 W/mK[37] for tubes with diameters 9.8 nm and 14 nm. On the other hand, molecular dynamic simulations suggest that thermal conductivity of an isolated (*10,10*) SWCNT could reach as high as 37,500 W/mK at temperature T = 100 K and falls to 6600 W/mK at T = 300K.[38] This decrease in thermal conductivity is due to the phonon-phonon Umklapp scattering. In another experimental study, an individual suspended SWCNT has shown thermal conductivities of 3000 W/mK at T = 100 K and 1000 W/mK at 800 K.[39]

Theoretical studies reveal that optical properties of chiral nanotubes change as the size of nanotubes increases. The electronic transitions between different energy bands of metallic and semiconducting nanotubes are characterized by van Hove singularities, which show the quantized momentum constituents along the circumferential direction.[40]

These van Hove singularities result from the folding of 2-D energy bands of a graphene layer into 1-D energy bands of nanotube. Optical properties of CNT could play an important role in using these materials for manufacturing optical devices like sensors.

In terms of chemical reactivity, CNT are more reactive than the interior carbon atoms of a graphene sheet due to the ring strain. Thus, reactivity of nanotubes can be related to its *pi*-orbital mismatch due to its strained curvature. The end caps of nanotube are more reactive than its side walls due to the more strained structure. Covalent functionalization of sidewalls or end caps of nanotube with organic molecules improves their dispersion in different solvents and polymer matrices.

1.4 Synthesis of Carbon Nanotubes.[40] Carbon nanotubes are synthesized by three main methods: arc discharge, chemical vapor deposition (CVD), and visible light vaporization. Visible light method consists of three separate methods: laser ablation uses pulsed laser as a source of heat, laser vaporization employs continuous laser, and solar vaporization utilizes continuous multi-wavelength light from a solar furnace. In arc discharge and visible light vaporization methods, graphite sublimes into an inert gas at high pressure and then graphite vapors condense at high temperature. A catalyst may or may not be used in both methods. The purpose of the catalyst is to direct the growth of the nanotube toward a particular type. For the synthesis of SWCNT, a catalyst is required for all the three methods mentioned above, and the mechanism of SWCNT formation is identical for all methods. The key step in the synthesis of SWCNT is the formation of a cap on the surface of a catalytic species which could be in the form of single to few metal clusters. These clusters serve as a nucleating site for the formation of a nanotube. A catalyst is required for a SWCNT to keep the growth end of a tube open. A catalyst is not required

for the synthesis of MWCNT because the interactions between the open ends of the concentric tubes stabilize the tube and allow further growth of a tube. The nucleation step is the key step in the synthesis, which determines whether a SWCNT or other species will form. The size, type, and chemical compositions of the metal cluster are important to synthesize the tube with different diameters and chiralities. While an in-depth discussion on different methods is well beyond the scope of this dissertation, a brief summary on each method of nanotubes preparation will be discussed in this section.

1.4.1 Arc Discharge.[41] Figure 6 shows the general setup for the carbon arc discharge method initially used to synthesize C_{60} fullerenes. This is the easiest and perhaps most commonly used method worldwide for synthesizing mainly SWCNT with few structural defects. In this method, a vapor is produced by arc discharge between the two carbon electrodes in the presence or absence of a catalyst. Nanotubes self assemble on the surface of the catalyst from their vapors followed by the vertical growth on the catalyst surface. After the synthesis nanotubes need to be separated from the mixture of soot (amorphous carbon) and metal catalysts. Additionally, the yield of this method is not satisfactory to achieve the requirements of nanotubes for long-term goal of mass production.

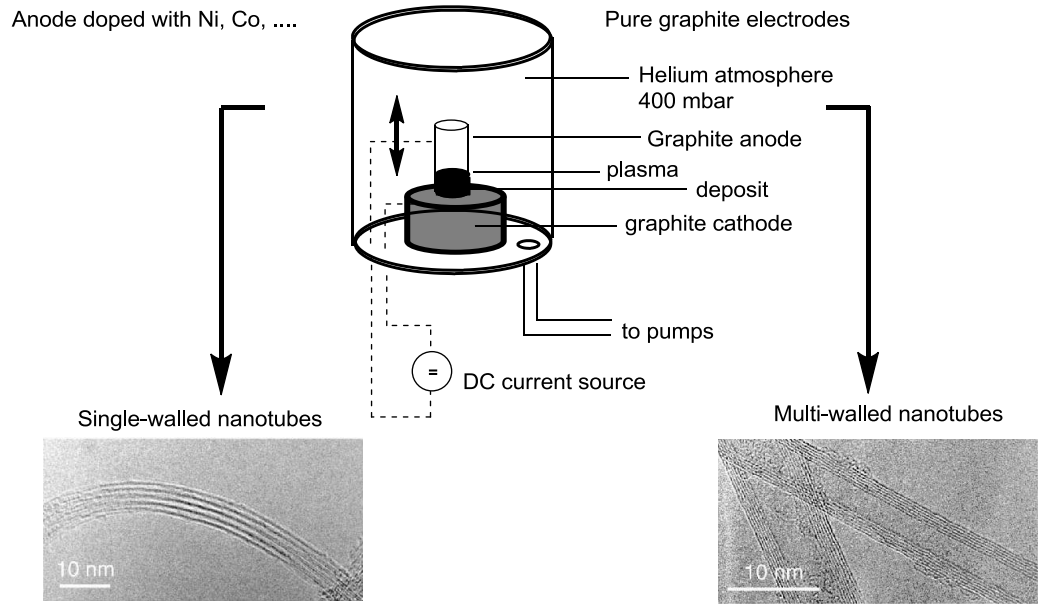

Figure 6. Diagram of set up for arc discharge method. The figure is re-drawn from the reference 41.

1.4.2 Chemical Vapor Deposition (CVD).[41] CVD shown in Figure 7 generally produces MWCNT at lower temperature (700-800 ^{o}C) and SWCNT at higher temperature (850-950 ^{o}C). CVD carbon nanotube synthesis is essentially a two-step process consisting of a catalyst preparation step followed by the synthesis of the nanotube. Excellent alignment and positional control of nanotube on nanometer scale can be achieved by this method. The growth rate of nanotubes and their diameters can be controlled. This method is easy to scale up for mass production and commercialization. In this method, catalysts such as Fe, Ni, and Co are deposited on the surface of Si, SiO_2 by thermal CVD and sputtering. The reaction gases CH_4, C_2H_2, C_2H_4, C_2H_6, and CO are injected into the reaction chamber during the discharge. Carbon nanotubes grow on the surface of the

nanoscopic fine catalyst particles by glow discharge generated by high power electricity. The yield of this method is around 50% and the diameter of MWCNT obtained is 15 nm.

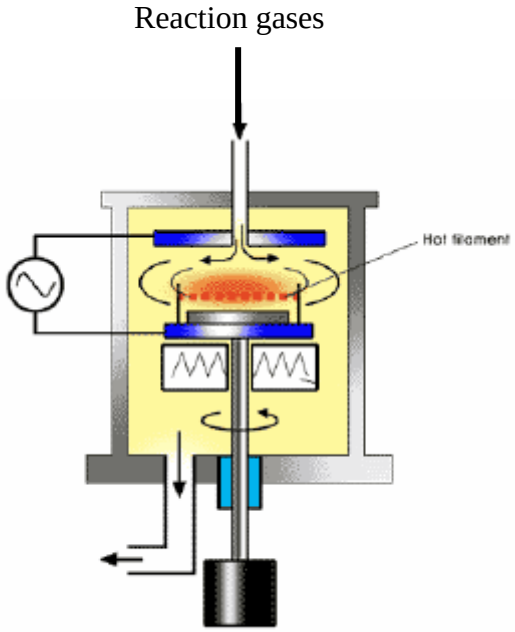

Figure 7. Diagram of set up for chemical vapor deposition method. The figure is copied from the reference 41.

CVD in its various forms produces SWCNT of high quality and higher percent yield of tubes than all other current methods of nanotube production.

1.4.2.1 Synthesis of HiPco Single-Walled Carbon Nanotubes by CVD Method.[42] HiPco, which stands for high-pressure catalytic decomposition of carbon monoxide, is a method where the metal catalyst is formed *in situ* when $Fe(CO)_5$ or $Ni(CO)_4$ is injected into the reactor along with a stream of carbon monoxide (CO) at the temperature 900-1100 ^{o}C and pressure 30-50 atm. The reaction responsible to produce SWCNT is the disproportionation of carbon monoxide to C (nanotube) and CO_2 by nanometer-size metal particles. This method produces SWCNT with high quality, purity, narrow diameter

distribution, and diameters ranging from 0.7 to 1.4 nm. In this method, SWCNT can be prepared with variety of diameters by changing the pressure of the reactor and the catalyst compositions.

1.4.2.2 Synthesis of CoMoCat Single-Walled Carbon Nanotube by CVD Method.[43] This method uses Co-Mo bimetallic catalysts supported on silica and a fluidized bed reactor that yields high selectivity towards the synthesis of SWCNT. In this method, calcinated Co-Mo catalysts at the molar ratio 2:1 are placed in a horizontal quartz tubular reactor, heated in H_2 up to 500 ^oC, and then in He to 700 ^oC. Subsequently, CO is introduced at a certain flow rate to synthesize SWCNT with diameters ranging from ~0.8 to 1.4 nm and small helical-angle distribution. Just two species (*6,5*) and (*7,5*) comprise approximately 58% by weight of the SWCNT.

1.4.3. Laser Ablation.[41] In laser ablation method shown in Figure 8, a high energy pulsed or continuous laser beam is used to vaporize a graphite target in an oven at the temperature of 1200 ^oC. The carbon containing feedstock gas is either CO or methane. The oven is filled with helium or argon gas in order to maintain the pressure at 500 Torr. As the vaporized carbon sources cool, small carbon molecules and atoms condense to form large clusters, possibly including fullerenes. The catalysts also begin to condense at the beginning, then attach to the carbon clusters and prevent them closing into closed structures. From those carbon clusters, tubular molecules grow into single-walled carbon nanotubes until the catalyst particles become too large, or conditions have cooled sufficiently that the vapors no longer diffuse through or over the catalyst particles. Sometimes the catalyst surface is coated with a thick carbon layer that cannot absorb any more carbon materials, which arrests the nanotube growth. SWCNT are bundled and have

smaller amounts of impurities in contrast to arc discharge method. The catalyst can be patterned, and a forest of SWCNT can be grown.

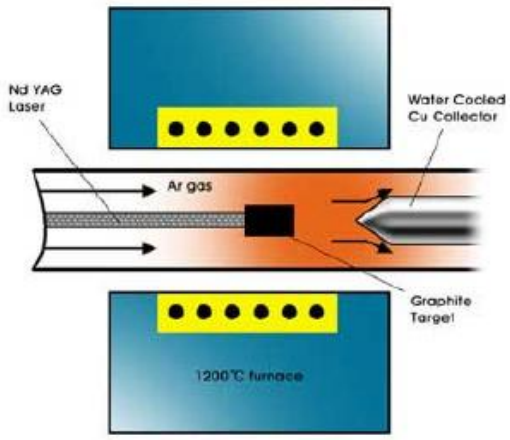

Figure 8. Diagram of set up for laser ablation method. The figure is copied from the reference 41.

1.5 Mechanism of Carbon Nanotube Growth on the Catalyst Particles.[41] Growth mechanism of carbon nanotube formation is not exactly known and numerous theories have been postulated on this topic. One of the plausible mechanisms comprises of formation of nanotubes or fullerenes precursor, C_2, on the surface of the catalyst particles. Figure 9 shows one of the plausible mechanisms of carbon nanotube formation. From the surface of the metastable carbide, rod like carbon nanotube starts to grow rapidly, move upward with the growing tube and remains connected to the metal particles. This type of mechanism is often called "tip-growth" mechanism. The size of the metal particle governs the formation of an individual SWCNT or nanotube bundles. The diameter of metal particles and clusters play a crucial role in the diameter and characteristics of the

SWCNT. For instance, sometimes the cluster is small enough that the diameter of the nanotube is nearly the same size as the diameter of the cluster. This results in the formation of single nanotube that has an encapsulated metal cluster at one end of the tube. In another case, if the diameter of the cluster is bigger and hence the nanotube grows perpendicular from the metal surface and result in the formation of nanotube bundles. In case of arc discharge method where no metal catalysts are used, nanotubes grow directly from the surface of the precursor carbide formed in the first step. During the upward growth of nanotube, the side wall grows by slow graphitization, which has been monitored by *in situ* HRTEM.[44,45] HRTEM study also suggests that graphenes exist at the early stage of the synthesis develop into well ordered graphene layers through fusions and rearrangements followed by evaporation of micro-graphene layers. Table 3 summarizes history of different synthetic methods used for the synthesis of carbon nanotubes.

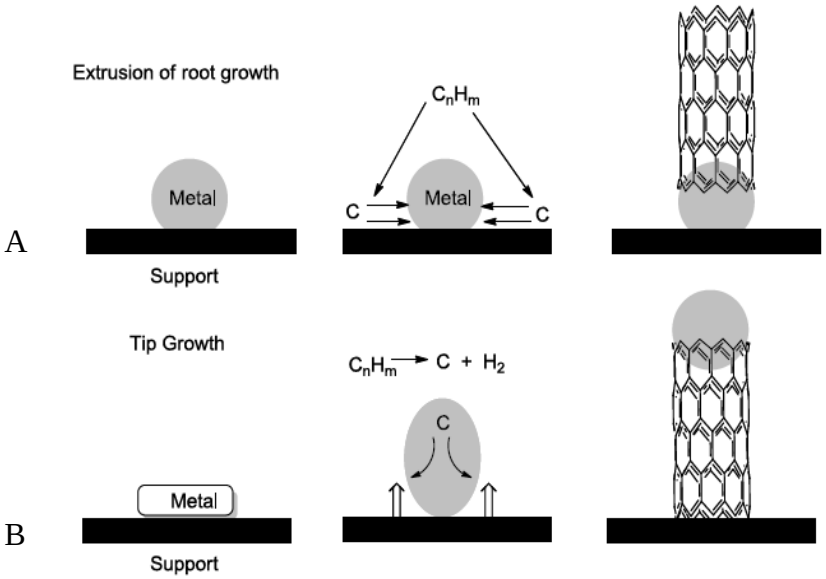

Figure 9. Plausible mechanism of carbon nanotube formation.

Table 3. History of Synthetic Methods for Carbon Nanotubes

method	arc discharge	chemical vapor deposition	laser ablation (vaporization)
Inventors	Ebbesen and Ajayan, NEC, Japan 1992[46]	Endo and co-workers, Shinshu University Nagano, Japan[47]	Smalley and co-workers, Rice University, 1995[48]
Technical	Two graphite rods few millimeters apart, connected to the electrical supply. At 100 amps, carbon vaporizes and forms a hot plasma, eventually CNT.	Place catalyst particles inside the oven, heated to 600 ^{o}C. Reaction gas (e.g. methane) purged into the chamber. Reaction gas decomposes releasing carbon atoms, which recombine to form CNT.	Graphite blasts with high intense laser producing carbon gases which recombine to form SWCNT, capable of forming high amount of SWCNT
Yield	30-90%	20-100%	Up to 70%
SWCNT	Short tubes, diameter = 0.6 to 1.4 nm	Long tubes, diameter = 0.6 to 4 nm	5-20 μm long bundles with diameter 1 to 2 nm
MWCNT	Short tubes, inner diameter 1-3 nm whereas outer diameter ~10 nm	Long tubes diameter ranging from 10 to 240 nm	MWCNT synthesis achievable, method is expensive
Pros	Prepares both SWCNT and MWCNT. SWCNT have few structural defects, MWCNT can be synthesized without any catalyst, inexpensive, synthesis possible at >2500 ^{o}C	Long SWCNT, diameter controllable, easy method, scalable to commercial production, substantially pure. Reaction temp. ranges from 700-1400 ^{o}C	Mainly synthesizes SWCNT, diameter controllable and few defects, end product is substantially pure. Reaction temp. is >2500 ^{o}C
Cons	Tubes are shorter with random sizes and directions; needs multiple purification steps	MWCNT with significant amount of defects	It needs expensive laser and high power

1.6 Polymer Functionalization of Carbon Nanotubes. The full potential use of CNT as a reinforcement filler has been limited because they tend to aggregate due to strong van der Waals attractions. Aggregates produce lower electrical conductivity and less increase in tensile modulus per weight than individual tubes. Moreover, low binding energy to the matrix polymer results in poor load transfer between the polymer and the nanotube. To overcome this problem surface modifications of nanotubes by covalent and noncovalent (physical) techniques have become a vital step towards the development of high strength nanocomposites. Covalent functionalization involves the conversion of some of the sp^2 side-wall C-atoms to sp^3 by small organic molecules or polymers, which improves the solubility and dispersion of CNT in different solvents and polymers. Additionally, covalent functionalization reactions such as diazonium chemistry,[49] dichlorocarbene reactions,[50] and osmylation reaction[51] can be performed selectively on the metallic tubes, which react faster than the semi-conducting tubes. Thus, higher reactivity of metallic tubes allows the separation of metallic tubes from the semi-conducting type from the mixture.[18]

Non-covalent functionalization comprises the adsorption of surfactants or polymers on the surface of nanotubes. In this section only covalent functionalization of CNT with polymers will be discussed due to the nature and scope of this work. Covalent side-wall functionalization of CNT increases the solubility and dispersion of nanotubes in various solvents and polymer matrices. There are two ways by which polymers are grafted onto the nanotube surface: "*grafting to*" and "*grafting from*" techniques.[52-54]

1.6.1 Grafting to Approach. "*Grafting to*" involves the addition of polymers to the nanotube surface or to functional groups on the nanotube surface. In this case the

molecular weight and polydispersity of the grafted polymers are known in advance. "*Grafting to*" of polymers has been accomplished by addition of polymer radicals,[55-57] anions,[58] nitrenes,[59] dipolarophiles,[60] and reactive dienes to the C-C double bonds of the sidewalls and by reacting functional groups present on the polymer with functional groups on the nanotube surface. Grafting polymers to the nanotubes by *in situ* free radical polymerization is a relatively simple and scalable approach involves the polymerization of monomers in the presence of initiators and nanotubes. Figure 10 shows different mechanisms of "*grafting to*" approach.

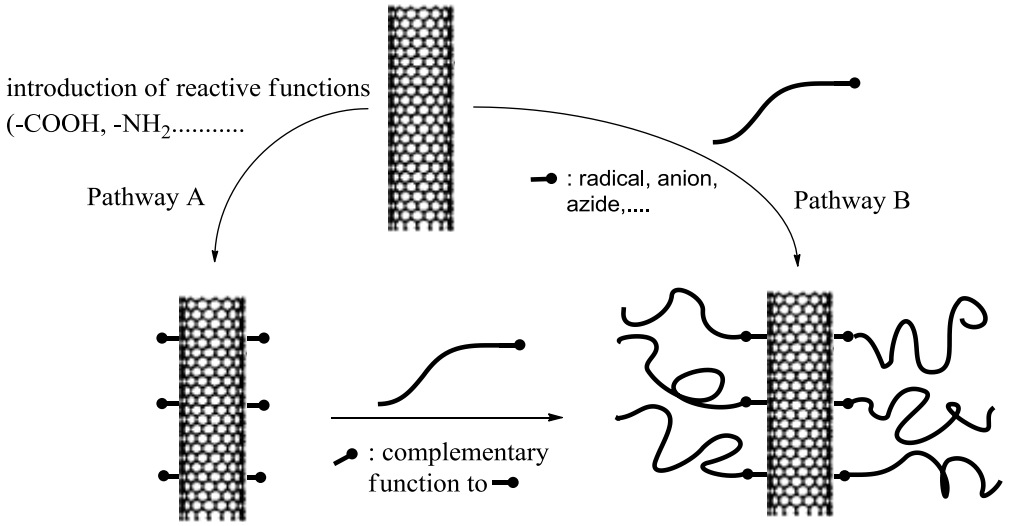

Figure 10. Two-step (pathway A) and one-step (pathway B) "*grafting to*" approach.

1.6.2 Grafting from Approach. "*Grafting from*" involves the immobilization of polymer precursor or initiator on the nanotube surface followed by subsequent polymerization from the nanotube surface. Initiators are covalently attached to the nanotubes via acid groups generated at the defect sites by treating the tubes with nitric acid or by side wall functionalization of nanotube. The advantage of "*grafting*" from

method is one can achieve high graft density because of less steric hindrance from the growing polymer chains. This method allows controlling the molecular weight of the grafted polymers and enables grafting polymers with high molecular weight.

Recently reversible deactivation radical polymerization has been advantageously implemented to graft polymers with well defined architecture on the surface of the nanotubes aiming tuning surface properties of nanotubes. Reversible deactivation radical polymerization offers many advantages over other methods of polymerization in producing variety of well controlled polymeric architectures (block, star, graft) with narrow molecular weight distribution, variety of functionality, and compositions. Their large functional groups tolerance and versatility made this technique popular to prepare wide variety of polymers. The reversible deactivation radical polymerization techniques used to functionalize CNT include atom transfer radical polymerization (ATRP),[61,62] nitroxide-mediated polymerization (NMP),[63] and reversible addition-fragmentation chain transfer polymerization (RAFT).[64] Figure 11 shows the general mechanism for "*grafting from*" approach.

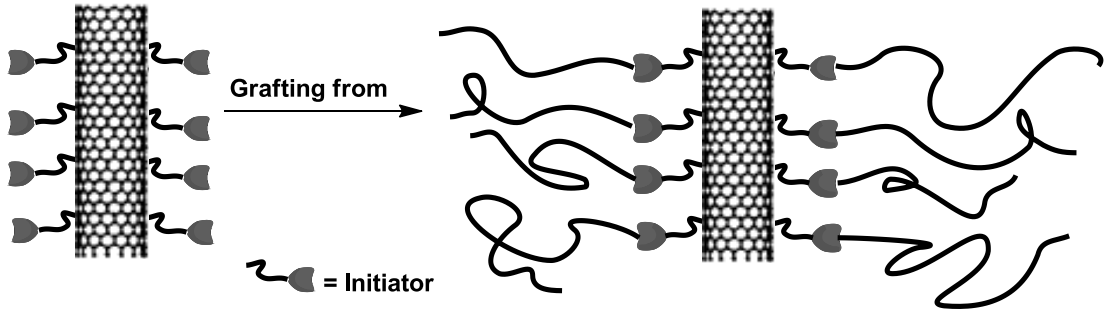

Figure 11. Functionalization of carbon nanotube by polymers via "*grafting from*" approach.

1.7 Carbon Nanotube Reinforced Polymer Composites. As mentioned previously, SWCNT exhibit extraordinary mechanical properties such as high tensile strengths (50 to 200 GPa), Young's moduli (1 to 5 TPa), and high strains at break up to ~6%. Thus, due to their excellent mechanical properties and high aspect ratio as much as 1000, SWCNT are considered to be excellent reinforcement filler for polymer nanocomposites. Therefore, recent studies focus on polymer-CNT composites because of their potentially superior mechanical properties compared to composites made with other conventional fillers like silica, polyhedral oligomeric silsesquioxane (POSS), carbon black, and carbon fiber. The goal is to develop polymer-CNT composites by taking an advantage of high electrical, thermal, and mechanical properties of carbon nanotubes. [65-68]

1.7.1 Dispersion of Carbon Nanotubes into Polymers.[40] There are several different methods used to disperse carbon nanotubes into the polymer matrices, and the determination of the ideal method is a challenging task. These methods utilize polymers, surfactants, acids, or a combination of several different materials to disperse carbon nanotubes into the polymer matrices. Most of the methods utilize some degree of sonication in the presence or absence of surfactants, from a few minutes to several hours to disperse the carbon nanotubes. This method of mechanical dispersion overcomes the van der Waals forces, where the surface active agent can de-bundle the carbon nanotubes to prevent re-aggregation. However, sonication can lead to significant amounts of damage to the carbon nanotubes, and the longer the carbon nanotubes are sonicated, the greater is the probability of damage. Therefore, in order to determine the most reliable method of dispersion without destroying the nanotube structure, research must be conducted to determine ideal dispersing agents, sonication time period, and other

processing parameters. The ability to determine an ideal dispersing agent for carbon nanotubes has been the subject of many studies. Most notable approaches consist of either the use of surfactants or polymers.

Methods used to disperse carbon nanotubes can be classified into four major categories: solution method, melt mixing, no fluid mixing, and impregnation/infusion. In this section, each method is discussed briefly to give readers an insight about the engineering involved.

1.7.1.1 Solution Method. In this method nanotubes are dispersed in a low-viscosity monomer followed by polymerization. In this method, dispersions of nanotubes and polymers are mixed together in a ratio to yield desired weight fraction of the CNT in the final composite followed by either removal of solvent by evaporation or precipitating the mixture into a large excess of non-solvent.

1.7.1.2 Melt Mixing. This method involves mixing of melted polymer with carbon nanotubes under high shear at a temperature usually slightly above the melting point of polymer. High shear forces are responsible for producing well-dispersed nanotubes at nano and micro scales. The amount of nanoscale dispersion achieved in this method is inferior to the solution method because the small molecules responsible for the exfoliation of tubes via diffusion are not available. Moreover, the forces involved in this method are much smaller in magnitude compared to the sonication. Therefore, this method may damage tubes less than sonication.

1.7.1.3 No Fluid Mixing. This method comprises mixing dry nanotubes or master batches of nanotubes in polymers with polymer powders under low shear rate. Nanoscale dispersion is not achieved by this method.

1.7.1.4 Impregnation/Infusion. In this method, nanotubes are grown on the substrate into their final shape and then the low viscosity monomer is added to the nanotubes followed by the polymerization. Generally, neat polymer melts are not added to the nanotubes because flow will not be adequate to prevent significant voids in the final products.

1.7.2 Mechanical Properties of Nanocomposites. This section will discuss different factors that can affect tensile properties of carbon nanotube-polymer composites. The tensile strength and modulus often increase at low filler loading, typically less than 1 wt%. Sometimes, both tensile strength and modulus decrease at higher filler loadings due to poor dispersion of nanotubes.[69-72] Improvement in the dispersion of nanotubes in polymer matrix improves the reinforcement and consequently mechanical properties of nanocomposites. The influence of different types and diameters of nanotubes on the tensile properties of composites has been explored in detail for poly(vinyl alcohol) and carbon nanotubes. Composites of poly(vinyl alcohol) mixed with SWCNT (bundles) (D = 9 nm), double-walled carbon nanotubes (DWCNT) (D = 2.5 nm), and MWCNT (D = 14-24 nm) were prepared and tensile properties were evaluated.[73] For SWCNT, reinforcement was inferior due to poor dispersion of nanotube bundles. The same is true for DWCNT as the volume fraction is increased beyond 0.1%. Young's modulus scales up linearly with total surface area per unit weight of nanotubes indicating that low diameter multiwall nanotubes are best suited for reinforcement of polymer nanocomposites. In another study on polyurethane-nanotube composites, MWCNT (D = 8-15 nm) and SWCNT (D = 1-2 nm) have different effects on the mechanical properties of polyurethane. MWCNT were useful in increasing the modulus whereas SWCNT

increase the elongation and tensile properties.[74] The difference in reinforcement of both MWCNT and SWCNT could be related to the rheological behavior of MWCNT and SWCNT in polyols. The shape factor '*f*' (shown in equation below) of MWCNT in polyols matrices is bigger and shear thinning behavior of MWCNT is higher than the SWCNT. The viscosity (η) of CNT-polymer composite can be written as:

$$\eta = \eta_0 (1 + 0.67 f C + 1.62 f^2 C^2) \qquad (1)$$

where, f is the shape factor, or the aspect ratio, i.e., the ratio of the longest to shortest diameter of particles, η_0 is the viscosity when CNT concentration is zero, and C is the concentration of CNT. The f value is dependent on the CNT morphology in polyols. A better dispersion of MWCNT leads to a high aspect ratio and thus a bigger f value. No good correlation was found between the diameters of nanotubes and their reinforcement potential in polymer composites. The stress transfer efficiency of polymer-nanotube composites depends on the aspect ratio of CNT. For example the elastic modulus of poly(vinyl alcohol) and MWCNT fibers was increased when the aspect ratio of MWCNT was increased from 24 to 43.[75]

Surface modification of CNT by small organic molecules and polymers is another way of improving the mechanical properties of carbon nanocomposites. It involves covalent[76,77] (with small organic molecules or polymers) and noncovalent[78] (with surfactants or polymers) modifications of CNT side walls. Surface modification increases the attractive interaction of CNT with the polymer matrix and consequently improves the mechanical properties. Nanotubes alignment (orientation) affects the tensile strength and modulus of nanocomposites. MWCNT filled PMMA nanocomposites have shown increase in tensile toughness with oriented nanotubes compared to unoriented

nanotubes.[79] Although numerous studies have been accomplished on the mechanical properties of carbon nanotube polymer composites, several other aspects such as interactions in CNT-polymer interphase regions and stress transfer from polymers to nanotubes need to be understood well to design high performance and durable nanocomposites.

1.7.3 Electrical Properties of Nanocomposites. The inherent conductivity of carbon nanotubes is determined by (*n,m*) integers, type of nanotube, and defects on the nanotubes. However, the electrical conductivity of carbon nanotube-polymer composite depends on the dispersion of CNT in the insulated polymer matrix and tube-tube connections. Electrical conductivity of composites is due to the transfer of charge from one tube to the other. A nanotube network is necessary to get high electrical conductivity of nanotube composites. When electrically conducting nanoparticles are dispersed within an insulating material such as carbon nanotube-polymer composite, the material is non-conducting until the volume fraction of conducting filler reaches certain region called *percolation threshold* as shown in Figure 12 below. The percolation theory suggests that the electrical conductivity (σ) of carbon nanotube composite depends on the volume fraction (V_f) of a filler 'c' through the following equation:[80]

$$\sigma = A(V_c - V_{fc})^{\beta} \quad (1)$$

where, A is the prefactor required for the fit, V_c is the filler volume fraction, V_{fc} is the percolation threshold, and the term β is critical exponent which reflects percolation mechanism. The value of β to a first approximation is independent of the volume or weight fractions used at the low level of carbon nanotube loadings for polymer composites. Typical theoretical values of β for the three-dimensional isotropic binary

systems lie between 1.6-2.0.[80]

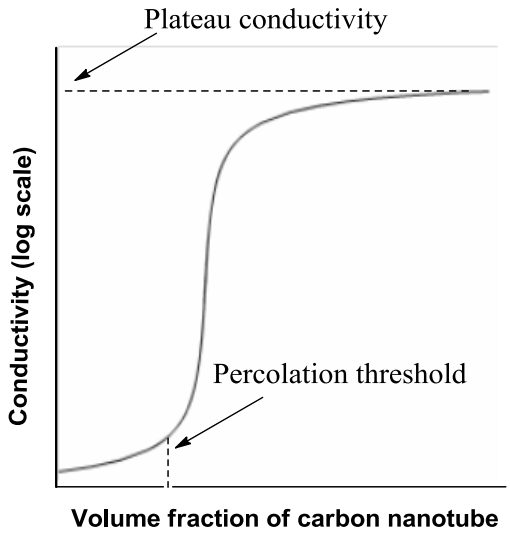

Figure 12. Electrical conductivity versus weight fraction for an insulating polymer filled with conductive carbon nanotubes. The increase in the percolation region is typically on the order of 10^{10}-10^{15} S/m. The figure is redrawn from the reference 40.

In Figure 12 the conductivity of first part of the plot is nearly constant on logarithmic scale and slightly increases linearly with the volume fraction of the filler. Then there is a sharp increase in the conductivity between the percolation threshold and the plateau region with CNT contents, where the conductivity increases only a small amount with further additions of conductive carbon nanotubes. Thus, to achieve high electrical conductivity for carbon nanotube based polymer composites at low SWCNT loadings, uniformly dispersed small bundle sized carbon nanotubes in the insulating polymer are important.

In general, SWCNT composites have lower electrical conductivities than the MWCNT composites. This could be due to poor dispersion of SWCNT in the polymer

matrix or higher contact resistance of smaller diameters SWCNT.[40] Tchoul *et al.* have reported the percolation threshold of conductivity of SWCNT/polystyrene composites from 0.17-0.3 wt% SWCNT for the poly[(*m*-phenylenevinylene)-*co*-(2,5-dioctoxy-*p*-phenylenevinylene)] (PmPV) coated SWCNT (HiPco, CoMoCat, and pulsed vapor vaporization (PLV)) and 0.4-0.5 wt% for those materials made by a coagulation method.[81] High aspect ratio and large surface area of MWCNT have significant effect on the conductivity of epoxy composites. The conductivity of epoxy composites was increased by a factor of 68 by increasing the nanotube length from 250 to 2500 nm.[82] The conductivity of MWCNT is independent of chemical functionalization because only the outer shell is affected by the functionalization and inner tubes can still conduct the electricity. However, three dimensional network formation through nanotube-nanotube and nanotube-matrix interactions is essential for the percolation threshold of electrical conductivity. Functionalization of MWCNT with acids, amines, and heat treatment at 500 ^{o}C for 1 h in air increased the dispersion of nanotubes in polymer matrix and thus improved the overall conductivity of nanocomposites.[83,84] On the other hand, the conductivity of SWCNT varied greatly with functionalization and doping of nanotubes with small atoms such as iodine increased the conductivity. However, covalent attachments of organic molecules can adversely affect the electrical conductivity of SWCNT. The processing conditions and shear forces largely influence the percolation threshold of composites. The high shear forces can disperse MWCNT uniformly in the epoxy matrix. In case of MWCNT-epoxy composites prepared by shear-intensive mechanical stirring at 2000 rpm, percolation threshold has been found to be ranged between 0.0020-0.0025 wt%, the lowest ever measured.[85-87] On the other hand, when

SWCNT were dispersed in the same epoxy system using similar high-shear mixing procedure, the percolation threshold was higher (0.05–0.23 wt%) than the MWCNT due to the poor dispersion of SWCNT in the epoxy matrix. Carbon nanotube based composites find commercial applications in electronic devices and sensors; however its full potential is limited until higher conductivities are achieved.[88] For instance to get protection against electrostatic discharge, a low level of conductivity or high level of resistivity ranging from 10^4 to 10^8 ohm/cm is enough, whereas to protect against electromagnetic interference as well as to prevent the emission of interfering radiation, resistivity of $\leq 10^4$ ohm/cm is needed. To date, a maximum conductivity of only 0.2 S/cm has been achieved, which is well below the required conductivity for use as an electrical conductor.[88] Therefore, increasing the number of tube-tube connections by increasing the tube length and/or orienting the nanotubes in the polymer composite is the biggest challenge to overcome to prepare highly electrically conductive carbon nanotube nanocomposites.

1.7.4 Thermal Properties of Nanocomposites. High thermal conductivity 'κ' (theoretical value ≈ 6600 W/m K) is one of the important physical properties of carbon nanotubes.[38] However, due to small interfacial thermal conductance between the nanotube and its surrounding polymers, there is only a modest improvement in the conductivity of carbon nanotube nanocomposites.[89] This interfacial thermal resistance is due to the failure to transfer high frequency phonon energy of nanotubes to the surroundings by phonon-phonon coupling. Thermal conductivity of CNT-polymer composites depends on many factors such as dispersion of nanotubes in the matrix polymer, nanotube loadings, aspect ratio, alignment, and impurities present in nanotubes.

Molecular dynamic simulations have shown the enhancement of thermal conductivity of nanotube filled nanocomposites when the SWCNT were functionalized.[90] SWCNT were purified by nitric acid treatment which generated carboxylic acid groups on the nanotube surface and removed metal impurities along with non-SWCNT materials (carbonaceous) from the mixture. The functionalized SWCNT filled epoxy composites have shown higher thermal conductivity compared to composites made with impure SWCNT.[91] The improvement in the thermal conductivity is due to the improvement in nanotube dispersion and the presence of more pure SWCNT tubes. SWCNT were used to augment the thermal properties of epoxy composites. Samples with 1 wt% filler loading showed increase in thermal conductivity of 70% and 125% at 40K and room temperature relative to the unfilled epoxy resin.[92] In another study, on SWCNT-epoxy composites prepared by an infiltration method on freestanding nanotube frameworks generated micron-scale bi-continuous phase and increased thermal conductivity by 220% relative to neat epoxy at 2.3 wt% nanotube loadings.[93] This approach reduced the interfacial thermal resistance at the nanotube/nanotube junctions. These findings suggest that one can achieve better electrical and thermal conductivities by heterogeneous distribution of SWCNT in different polymer matrices. The thermal conductivities of different types of CNT (SWCNT, DWCNT, MWCNT) in epoxy composites were studied in detail with respect to filler loadings, interfacial area, influence of surface functionalization, and aspect ratio. This study suggests that MWCNT have highest potential to improve the thermal conductivity because of relatively low interfacial area which confers less interfacial thermal resistance.[94] Both theoretical and experimental analyses of CNT length on the thermal conductivity of composites reveal that an appropriate length distribution of CNT

could improve the thermal conductivity of composites.[95] Alignment of nanotubes in nanocomposites enhances the overall thermal conductivity. In SWCNT-epoxy composites, thermal conductivity increases 300% at 3 wt% nanotube loading relative to the conductivity of neat epoxy resins. An additional 10% increase was observed in case of magnetically aligned SWCNT.[96] In another study, silicone elastomers were injected into the thick and aligned MWCNT forest grown on the silicone substrate.[97] This study reveals that at very low fraction (0.4 vol% or 0.3 wt%) of aligned MWCNT, thermal conductivity was increased from 115 to 280%, more than the neat epoxy resins or MWCNT dispersed in matrix polymer.

1.8 Technical Challenges. Since the discovery of CNT, adequate research has been done to understand the properties of CNT needed to use their full potential. However, there are many technical challenges involved with carbon nanotubes.

1.8.1 Carbon Nanotube Synthesis. CNT are synthesized by a number of ways but none of the methods has good control of diameters, length, and chirality. In spite of using identical methods and standard synthetic conditions there exists a large variation in morphology and properties of carbon nanotubes. Therefore, work needs to be done which can correlate these variables and properties between batches of carbon nanotubes towards the development of standard method for the synthesis of CNT with unique properties which won't vary from one batch to the other.

1.8.2 Carbon Nanotube Polymer Composites. Another issue associated with SWCNT is the aggregation due to strong van der Waals forces which could lead to poor dispersion of nanotubes in the matrix polymer especially at high filler loading (>6 wt%) in nanocomposites. Furthermore, we need to pay attention to other issues such as

inadequate nanotube loading and lack of alignment of nanotubes in the matrix polymer. SWCNT can be considered as hollow cylinders formed of graphite layers with both ends of the cylinder normally capped by fullerene-like structures which are more reactive compared to their side-walls. However, end caps do not affect the reactivity of nanotubes to a large extent. Thus, due to these less reactive side-walls there is no good interfacial bonding between the CNT and the matrix polymer resulting in a poor load transfer from nanotubes to the matrix polymer. Therefore, surface modification of SWCNT either by covalent or non-covalent approach has become an inevitable step to improve the dispersion of CNT in various solvents and polymer nanocomposites. In order to realize full potential of CNT, a standard method should be developed for the mass production of CNT balancing their outstanding inherent properties with reasonable cost. Existing methodologies of composite preparation must be amended and new technologies must be developed to improve dispersion and orientation of CNT in the polymer matrix. Surface modifications of CNT using both covalent and non-covalent techniques are necessary to increase the nanotube dispersion, solubility, and load transfer from the matrix polymer to the nanotube. A recent trend indicates that researchers are involved in manufacturing functionalized nanostructured materials with additional functions such as self assembly and self-healing. Even though properties of CNT look promising, major technical challenges pertaining to manufacturing and dispersion need to be solved before utilizing them for various potential applications.

In conclusion, **s**ince their discovery in 1991, carbon nanotubes have attracted many researchers world-wide. The small dimension, superior mechanical properties, and remarkable physical properties have made them a unique material for variety of

promising applications ranging from tiny electronic devices, to biomedical uses, packaging films, superabsorbents, components of armor, and parts of automobiles. The excitement about carbon nanotubes stems from their unique properties. For instance, an elastic modulus of 1 TPa and tensile strength of 100 GPa have made SWCNT the most promising reinforcement filler to prepare nanocomposites with high specific strength. Other properties of CNT such as excellent electrical, thermal, optical, and magnetic properties have enabled the development of carbon nanotube based multifunctional and structural nanomaterials.

1.9 Graphene. For the past decade, carbon nanotubes (CNT) have been the center of attraction for many researchers for the development of many potential applications such as molecular electronics, optoelectronics, field emission devices, batteries, catalysis, gas storage, sensors, and polymer nanocomposites.[8] Recently, researchers have begun to shift their interest on another carbon-based nanomaterial called "*graphene*".[98,99] Graphene is the name given to a monolayer or a few layers of carbon atoms tightly packed into a two-dimensional (2D) honeycomb lattice, and is a basic building block for graphitic materials of all other dimensionalities (Figure 13). It can be wrapped up into 0D fullerenes, rolled into 1D nanotubes or stacked into 3D graphite.

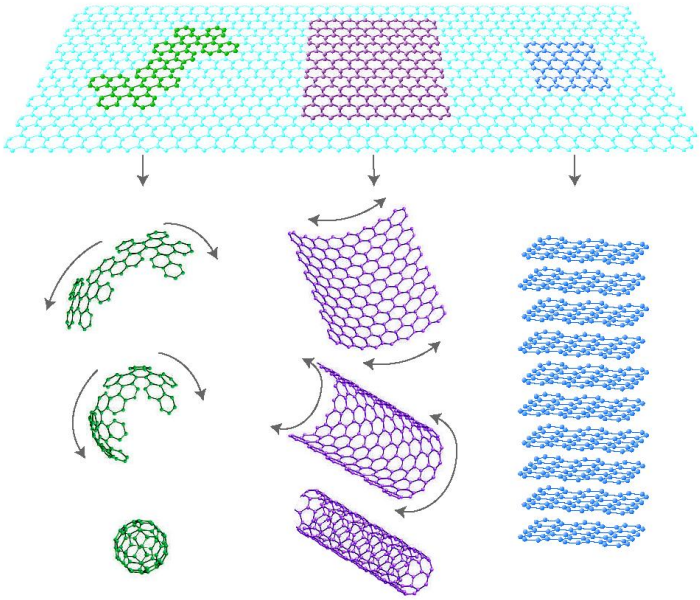

Figure 13. Mother of all graphitic forms. Graphene is a 2D building material for carbon materials of all other dimensionalities. This figure was copied from the reference 98.

Recently, mechanical and thermal properties of graphene have been studied in detail. It exhibits a breaking strength of ~40 N/m, reaching the theoretical limit of 42 N/m for monolayer graphene, record values for room temperature thermal conductivity of ~5000W/m^{-1} K^{-1}, and Young's modulus of ~1.0 TPa with a maximum strain at break of ~20% of its original length.[99] Graphene sheets have higher surface-to-volume ratios than CNT owing to the inaccessibility of the inside surface of the nanotubes.[100] This makes graphene sheets potentially more favorable for improving the properties of matrix polymers such as the mechanical, rheological and permeability properties, and thermal stability. Further, graphene is obtained from naturally occurring graphite implying that lighter nanocomposites can be produced at lower costs. Tailor-made graphene based polymer nanocomposites which exploit the superlative properties of both graphene filler

and polymer host can show enhanced performance in a large number of applications ranging from flexible packaging, semi-conductive sheets in transistors, memory devices, hydrogen storage, and printable electronics.[90] Despite excellent electrical properties, graphenium microprocessors are unlikely to come for the next 20 years.[98] It is expected that after the complete development of graphene films on a large scale with desired electrical properties, graphene may be used as a replacement for silicon based electronics and thus provide future electronic devices which are cost-effective and eco-friendly, and have better functionality and higher stability. In conclusion, due to graphene's large surface-to-volume ratio and high conductivity, the immediate applications of graphene are in polymer nanocomposites, electric batteries, hydrogen storage materials, field emitters (plasma displays), and supercapacitors.

1.10 Research Objectives. To utilize full potential of CNT, surface modification has become absolutely necessary, practical, and effective way to improve the dispersion of nanotubes in polymer nanocomposites. Over the past few years, much attention has been paid to the covalent functionalization of carbon nanotubes. The covalent functionalization allows carrying out a wide range of chemistry on the nanotube surface and fine tuning their properties for various potential applications. In general, covalent functionalization targets the end caps, defects, and side walls of CNT. The presence of defects makes the covalent functionalization possible by small to big organic molecules (e.g. polymers) onto the nanotube surface which in turn increases the interfacial interaction between the filler and the matrix polymer and hence the reinforcement effects of CNT.

Our research emphasizes the understanding of the fundamental properties of single-walled carbon nanotubes and its composites made with different polymer matrices. We have two types of objectives for carbon nanotube work.

(1) Materials objective: This objective aspires to covalently functionalize SWCNT with polymers such as polystyrene and poly(methyl methacrylate), disperse them in chemically similar polymer matrix to develop nanocomposites with improved electrical conductivity, thermal conductivity, and high mechanical strength with low nanotube loadings.

(2) Processing objective: This objective aims at devising simple methods for covalently grafting polymers to the SWCNT surface using commercially available nanotubes without extensive purification and incorporates them into a variety of polymer matrices to prepare carbon nanotube based nanocomposites.

References

1. Kroto, H. W.; Heath, J. R.; O'Brien, S. C.; Curl, R. F.; Smalley, R. E., *Nature* **1985,** *318*, 162-163.
2. Endo, M.; Koyama, T.; Hishiyama, Y., *Jpn. J. Appl. Phys.* **1976,** *15*, 2073-2076.
3. Oberlin, A.; Endo, M.; Koyama, T., *Carbon* **1976,** *14*, 133-135.
4. Oberlin, A.; Endo, M.; Koyama, T., *J. Cryst. Growth* **1976,** *32*, 335—349.
5. Iijima, S., *Nature* **1991,** *354*, 56-58.
6. Bethune, D. S.; Kiang, C. H.; De Vries, M. S.; Gorman, G.; Savoy, R.; Vazquez, J.; Beyers, R., *Nature* **1993,** *363*, 605-607.
7. Iijima, S.; Ichihashi, T., *Nature* **1993,** *363*, 603-605.
8. Schnorr, J. M.; Swager, T. M., *Chem. Mater.* **2011,** *23*, 646-657.
9. Krishnan, A.; Dujardin, E.; Ebbesen, T. W.; Yianilos, P. N.; Treacy, M. M. J., *Phys. Rev. B* **1998,** *58*, 14013–14019.
10. Tombler, T. W.; Zhou, C.; Alexseyev, L.; Kong, J.; Dai, H.; Liu, L.; Jayanthi, C. S.; Tang, M.; Wu, S. -Y., *Nature* ***2000,*** *405*, 769-772.
11. Cai, J.; Wang, C. Y.; Yu, T.; Yu, S., *Phys. Scr.* **2009,** *79*, 025702.
12. Salvetat, J. -P.; Briggs, G. A. D.; Bonard, J. -M.; Bacsa, R. R.; Kulik, A. J.; Stöckli, T.; Burnham, N. A.; Forró, L., *Phys. Rev. Lett* **1999,** *82*, 944-947.
13. Guo, Y.; Guo, W., *J. Phys. D: Appl. Phys.* **2003,** *36*, 805–811.
14. Li, F.; Cheng, H. M.; Bai, S.; Su, G., *Appl. Phys. Lett.* **2000,** *77*, 3161-3163.
15. Baughman, R. H.; Zakhidov, A. A.; De Heer, W. A., *Science* **2002,** *297*, 787-792.
16. Hong, S.; Myung, S., *Nat. Nanotechnol.* **2007,** *2*, 207- 208.
17. Hone, J.; Whiteney, M.; Zettl, A., *Synth.Met.* **1999,** *103*, 2498-2499.

18. Hennrich, F.; Chan, C.; Moore, V.; Rolandi, M.; O'Connell, M., The element carbon. In *Carbon Nanotubes Properties and Applications*, O'Connell, M. J., Ed. CRC Press: Boca Raton FL, 2006.

19. Mintmire, W. J.; White, C. T., *Carbon* **1995,** *33*, 893-902.

20. Sears, A.; Batra, R. C., *Phys. Rev. B* **2004,** *69*, 235406.

21. Lu, J. P., *Phys. Rev. B* **1997,** *79*, 1297-1300.

22. Hernandez, E.; Goze, C.; Bernier, P.; Rubio, A., *Appl. Phys. A.* **1999,** *68*, 287–292.

23. Wong, E. W.; Sheehan, P. E.; Lieber, C. M., *Science* **1997,** *277*, 1971-1975.

24. Treacy, M. M. J.; Ebbesen, T. W.; Gibson, J. M., *Nature* **1996,** *381*, 678-680.

25. Lourie, O.; Wagner, H. D., *J. Mater. Res.* **1998,** *13*, 2418-2422.

26. Salvetat, J.-P.; Bonard, J.-M.; Thomson, N. H.; Kulik, A. J.; Forro, L.; Benoit, W.; Zuppiroli, L., *Appl. Phys. A.* **1999,** *69*, 255-260.

27. Cooper, C. A.; Young, R. J.; Halsall, M., *Composites: Part A* **2001,** *32*, 401-411.

28. Yu, M.-F.; Lourie, O.; Dyer, M. J.; Moloni, K.; Kelly, T. F.; Ruoff, R. S., *Science* **2000,** *287*, 637-640.

29. Yu, M.-F.; Files, B. S.; Arepalli, S.; Ruoff, R. S., *Phys. Rev. Lett.* **2000,** *84*, 5552-5555.

30. Belytschko, T.; Xiao, S. P.; Schatz, G. C.; Ruoff, R. S., *Phys. Rev. B.* **2002,** *65*, 235430.

31. Wang, S. Functionalization of Carbon Nanotubes: Characterization, Modeling and Composite Applications. Ph.D. Dissertation, Florida State University, Tallahassee, FL, 2006.

32. Dai, H.; Wong, E. W.; Lieber, C. M., *Science* **1996,** *272*, 523-526.

33. Ebbesen, T. W.; Lezec, H. J.; Hiura, H.; Bennett, J. W.; Ghaemi, H. F.; Thio, T., *Nature* **1996,** *382*, 54-56.

34. Mann, D.; Javey, A.; Kong, J.; Wang, Q.; Dai, H., *Nano Lett.* **2003,** *3*, 1541–1544.

35. Thess, A.; Lee, R.; Nikolaev, P.; Dai, H.; Petit, P.; Robert, J.; Xu, C.; Lee, Y. H.; Kim, S. G.; Rinzler, A. G.; Colbert, D. T.; Scuseria, G. E.; Tománek, D.; Fischer, J. E.; Smalley, R. E., *Science* **1996,** *273*, 483-487.

36. Fujii, M.; Zhang, X.; Xie, H.; Ago, H.; Takahashi, K.; Ikuta, T.; Abe, H.; Shimizu, T., *Phys. Rev. Lett.* **2005,** *95*, 065502.

37. Kim, P.; Shi, L.; Majumdar, A.; McEuen, P. L., *Phys. Rev. Lett.* **2001,** *87*, 215502.

38. Berber, S.; Kwon, Y.-K.; Tománek, D., *Phys. Rev. Lett.* **2000,** *84*, 4613-4616.

39. Pop, E.; Mann, D.; Wang, Q.; Goodson, K.; Dai, H., *Nano Lett.* **2006,** *6*, 96–100.

40. Grady, B. P., In *Carbon Nanotube-Polymer Composites: Manufacture, Properties, and Applications*. John Wiley & Sons: New York, 2011.

41. Daenen, M.; de Fouw, R. D.; Hamers, B.; Janssn, P. G. A.; Schouteden, K.; Veld, M. A. J. *The Wondrous World of Carbon Nanotubes*; Technical Report for Phillips NAT-lab: February 2003.

42. Nikolaev, P.; Bronikowski, M. J.; Bradley, R. K.; Rohmund, F.; Colbebrt, D. T.; Smith, K. A.; Smalley, R. E., *Chem. Phys. Lett.* **1999,** *313*, 91-97.

43. Kitiyanan, B.; Alvarez, W. E.; Harwell, J. H.; Resasco, D. E., *Chem. Phys. Lett.* **2000,** *317*, 497-503.

44. Yasuda, A.; Kawase, N.; Banhart, F.; Mizutani, W.; Shimizu, T.; Tokumoto, H., *J. Phys. Chem. B* **2002,** *106*, 1849-1852.

45. Yasuda, A.; Kawase, N.; Mizutani, W., *J. Phys. Chem. B* **2002,** *106*, 13294-13298.

46. Ebbesen, T. W.; Ajayan, P. M., *Nature* **1992,** *358*, 220-222.

47. Endo, M.; Takeuchi, K.; Igarashi, S.; Kobori, K.; Shiraishi, M.; Kroto, H. W., *J. Phys. Chem. Solids* **1993,** *54*, 1841-1848.

48. Guo, T.; Nikolaev, P.; Rinzler, A. G.; Tomanek, D.; Colbert, D. T.; Smalley, R. E., *J. Phys. Chem.* **1995,** *99*, 10694-10697.

49. Strano, M. S.; Dyer, C. A.; Usrey, M. L.; Barone, P. W.; Allen, M. J.; Shan, H.; Kittrell, C.; Hauge, R. H.; Tour, J. M.; Smalley, R. E., *Science* **2003,** *301*, 1519-1522.

50. Kamaras, K.; Itkis, M. E.; Hu, H.; Zhao, B.; Haddon, R. C., *Science* **2003,** *301*, 1501.

51. Banerjee, S.; Wong, S. S., *J. Am. Chem. Soc.* **2004,** *126*, 2073-2081.

52. Tasis, D.; Tagmatarchis, N.; Bianco, A.; Prato, M., *Chem. Rev.* **2006,** *106*, 1105-1136.

53. Homenick, C. M.; Lawson, G.; Adronov, A., *Polym. Rev.* **2007,** *47*, 265–290.

54. Bahun, G. J.; Cheng, F.; Homenick, C. M.; Lawson, G.; Zhu, J.; Adronov, A., In *Chemistry of Carbon Nanotubes*, Basiuk, V. A.; Basiuk, E. V., Eds. American Scientific Publishers: Stevenson Ranch, CA USA, 2008; Vol. 2, pp 191-246.

55. Lou, X.; Detrembleur, C.; Sciannamea, V.; Pagnoulle, C.; Jerome, R., *Polymer* **2004,** *45*, 6097–6102.

56. Liu, Y.; Yao, Z.; A., A., *Macromolecules* **2005,** *38*, 1172-1179.

57. Qin, S.; Qin, D.; Ford, W. T.; Resasco, D. E.; Herrera, J. E., *Macrmolecules* **2004,** *37*, 752-757.

58. Viswanathan, G.; Chakrapani, N.; Yang, H.; Wei, B.; Chung, H.; Cho, K.; Ryu, C. Y.; Ajayan, P. M., *J. Am. Chem. Soc.* **2003,** *125*, 9258-9259

59. Holzinger, M.; Vostrowsky, O.; Hirsch, A.; Hennrich, F.; Kappes, M.; Weiss, R.; Jellen, F., *Angew. Chem. Int. Ed.* **2001,** *40*, 4002-4005.

60. Georgakilas, V.; Kordatos, K.; Prato, M.; Guldi, D. M.; Holzinger, M.; Hirsch, A., *J. Am. Chem. Soc.* **2002,** *124*, 760-761.

61. Qin, S.; Qin, D.; Ford, W. T.; Resasco, D. E.; Herrera, J. E., *J. Am. Chem. Soc.* **2004,** *126*, 170-176.

62. Yao, Z.; Braidy, N.; Botton, G. A.; Adronov, A., *J. Am. Chem. Soc.* **2003,** *125*, 16015-16024.

63. Dehonor, M.; Masenelli-Varlot, K.; González-Montiel, A.; Gauthier, C.; Cavaillé, J. Y.; Terrones, H.; Terrones, M., *Chem. Commun.* **2005,** (42), 5349–5351.

64. Cui, J.; Wang, W.; You, Y.; Liu, C.; Wang, P., *Polymer* **2004,** *45*, 8717–8721.

65. Krishnamoorti, R.; Vaia, R. A., *J. Polym. Sci., Part B: Polym. Phys.* **2007,** *45*, 3252-3256.

66. Winey, K. I.; Vaia, R. A., *MRS Bull.* **2007,** *32*, 314-322.

67. Krishnamoorti, R., *MRS Bull.* **2007,** *32*, 341-347.

68. Moniruzzaman, M.; Winey, K. I., *Macrmolecules* **2006,** *39*, 5194-5205.

69. Ha, M. L. P.; Grady, B. P.; Lolli, G.; Resasco, D. E.; Ford, W. T., *Macromol. Chem. Phys.* **2007,** *208*, 446–456

70. Wong, M.; Paramsothy, M.; Xu, X. J.; Ren, Y.; Li, S.; Liao, K., *Polymer* **2003,** *44*, 7757–7764.

71. Zhao, C., -X.; Zhang, W.-D.; Sun, D.-C., *Polym. Compos.* **2009,** *30*, 649-654.

72. Blond, D.; Barron, V.; Ruether, M.; Ryan, K. P.; Nicolosi, V.; Blau, W. J.; Coleman, J. N., *Adv. Funct. Mater.* **2006,** *16*, 1608-1614.

73. Cadek, M.; Coleman, J. N.; Ryan, K. P.; Nicolosi, V.; Bister, G.; Fonseca, A.; Nagy, J. B.; Szostak, K.; Be´guin, F.; Blau, W. J., *Nano Lett.* **2004,** *4*, 353-356.

74. Xia, H.; Song, M., *Soft Matter* **2005,** *1*, 386–394.

75. Wong, K. K. H.; Zinke-Allmang, M.; Hutter, J. L.; Hrapovic, S.; Luong, J. H. T.; Wan, W., *Carbon* **2009,** *47*, 2571-2578.

76. Sun, L.; Warren, G. L.; O'Reilly, J. Y.; Everett, W. N.; Lee, S. M.; Davis, D.; Lagoudas, D.; Sue, H.-J., *Carbon* **2008,** *46*, 320-328.

77. Velasco-Santos, C.; Martı´nez-Herna´ndez, A. L.; Fisher, F. T.; Ruoff, R.; Castan˜o, V. M., *Chem. Mater.* **2003,** *15*, 4470-4475.

78. Wang, T.; Dalton, A. B.; Keddie, J. L., *Macrmolecules* **2008,** *41*, 7656-7661.

79. Gorga, R. E.; Cohen, R. E., *J. Polym. Sci., Part B: Polym. Phys.* **2004,** *42*, 2690–2702.

80. Weber, M.; Kamal, M. R., *Polym. Compos.* **1997,** *18*, 711-725.

81. Tchoul, M. N.; Ford, W. T.; P., H. M. L.; Sumarriva, I. C.; Grady, B. P.; Lolli, G.; Resasco, D. E.; Arepalli, S., *Chem. Mater.* **2008,** *20*, 3120-3126.

82. Li, J.; Lumpp, J. K.; Andrews, R.; Jacques, D., *J. Adhes. Sci. Technol.* **2008,** *22*, 1659-1671.

83. Li, Q.; Xue, Q.; Hao, L.; Gao, X.; Zheng, Q., *Compos. Sci. Technol.* **2008,** *68*,

2290–2296.

84. Lee, S. H.; Cho, E.; Jeon, S. H.; Youn, J. R., *Carbon* **2007,** *45*, 2810-2822.

85. Sandler, J. K. W.; Kirk, J. E.; I.A. Kinloch; Shaffer, M. S. P.; Windle, A. H., *Polymer* **2003,** *44*, 5893–5899.

86. Moisala, A.; Li, Q.; Kinloch, I. A.; Windle, A. H., *Compos. Sci. Technol.* **2006,** *66*, 1285–1288.

87. Martin, C. A.; Sandler, J. K. W.; Shaffer, M. S. P.; Schwarz, M.-K.; Bauhofer, W.; Schulte, K.; Windle, A. H., *Compos. Sci. Technol.* **2004,** *64*, 2309–2316.

88. Mylvaganam, K.; Zhang, L. C., *Recent Pat. Nanotechnol.* **2007,** *1*, 59-65.

89. Huxtable, S. T.; Cahill, D. G.; Shenogin, S.; Xue, L.; Ozisik, R.; Barone, P.; Usrey, M.; Strano, M. S.; Siddons, G.; Shim, M.; Keblinski, P., *Nat. Mater.* **2003,** *2*, 731-734.

90. Shenogin, S.; Bodapati, A.; Xue, L.; Ozisik, R.; Keblinski, P., *Appl. Phys. Lett.* **2004,** *85*, 2229-2231.

91. Yu, A.; Itkis, M. E.; Bekyarova, E.; Haddon, R. C., *Appl. Phys. Lett.* **2006,** *89*, 133102.

92. Biercuk, M. J.; Llaguno, M. C.; Radosavljevic, M.; Hyun, J. K.; Johnson, A. T., *Appl. Phys. Lett.* **2002,** *80*, 2767.

93. Du, F.; Guthy, C.; Kashiwagi, T.; Fischer, J. E.; Winey, K. I., *J. Polym. Sci., Part B: Polym. Phys.* **2006,** *44*, 1513-1519.

94. Gojny, F. H.; Wichmann, M. H. G.; Fiedler, B.; Kinloch, I. A.; Bauhofer, W.; Windle, A. H.; Schulte, K., *Polymer* **2006,** *47*, 2036-2045.

95. Song, P. C.; Liu, C. H.; Fan, S. S., *Appl. Phys. Lett.* **2006,** *88*, 153111.

96. Choi, E. S.; Brooks, J. S.; Eaton, D. L.; Al-Haik, M. S.; Hussaini, M. Y., *J. Appl. Phys.* **2003,** *94*, 6034-6039.

97. Huang, H.; Liu, C.; Wu, Y.; Fan, S., *Adv. Mater.* **2005,** *17*, 1652-1656.

98. Geim, A. K.; Novoselov, K. S., *Nature Materials* **2007,** *6*, 183-191.

99. Geim, A. K., *Science* **2009,** *324*, 1530-1534.

100. Salavagione, H. J.; Martínez, G.; Ellis, G., In *Physics and Applications of Graphene - Experiments*, Mikhailov, S., Ed. InTech, Croatia, 2011.

CHAPTER II

POLY(STYRENE) FUNCTIONALIZED SINGLE-WALLED CARBON NANOTUBE-POLYMER COMPOSITES

ABSTRACT: Single-walled carbon nanotubes (SWCNT) were functionalized with polystyrene (PS) with number average molecular weights (2270, 2850, 15000, and 49500 g/mol) and polydispersities (PDI) (1.13-1.36) through radical coupling reaction involving polystyryl radical generated at 130 ^{o}C and mildly acid functionalized SWNT dispersed in 1-methyl-2-pyrrolidinone. The amount of grafted polystyrene was found to be in the range of 20-25 weight %, independent of polystyrene molecular weights. In Raman spectra, the intensity ratios of D to G bands were alike for all polystyrene grafted samples (SWCNT-*g*-PS) and the starting SWCNT. Numerous near-infrared peaks of polystyrene functionalized SWCNT indicate the retention of inherent electronic properties. Composites of SWCNT-*g*-PS in a commercial grade PS, of number average molecular weight = 70,000 g/mol and PDI = 3.0, were prepared by a coagulation method. All of the SWCNT-*g*-PS had low electrical conductivity and showed no percolation threshold of electrical conductivity due to thick polymer coatings on the nanotube surface. On the

other hand, composites of nitric acid treated SWCNT had a plateau conductivity of ~10^{-4} S/cm at 3.0 wt% SWCNT and a percolation threshold of electrical conductivity <1.0 wt % SWCNT. TEM images showed bundles of SWCNT-*g*-PS of different sizes and uneven PS coatings on the nanotube surfaces. For SWCNT-*g*-PS2850 composites, the glass transition temperature (T_g) increased to 106-108 ^oC at 6 wt% SWCNT, and formed a plateau of 107-110 ^oC at 10-20 wt% SWCNT. For SWCNT composites grafted with two higher molecular weights of PS, T_g increased to 104-109 ^oC at 6 wt% SWCNT, and formed a plateau from 10-20 wt% SWCNT with little change in the T_g value. The change of heat capacity (ΔC_p) at T_g continued to decrease with increasing the amounts of nanotubes for SWCNT-*g*-PS2270, whereas there was a little or no change in ΔC_p for SWCNT-*g*-PS15000 and SWCNT-*g*-PS49500 composites.

2.1 Introduction

Single-walled carbon nanotubes (SWCNT) and multi-walled carbon nanotubes (MWCNT) have attracted many researchers worldwide due to their extraordinary electrical, thermal, and mechanical (tensile and storage modulus) properties for many potential applications in electrodes, supercapicitaors, electronics, field emission displays, catalysts, membranes, sensors, electronic devices, biomedical devices, and high strength fibers.[1,2]

However, carbon nanotubes possess poor solubility in many organic and aqueous solvents, making their processing and solution-phase manipulation of SWCNT difficult, limiting the use of their full potential. Carbon nanotubes appear in bundles due to strong forces of attraction, and their side-walls are not attracted to polymers resulting in

aggregations of nanotubes in the host polymer. One way to mitigate the solubility and dispersion problems is the chemical functionalization of side walls of CNT with small molecules using highly reactive reagents, such as carbenes[3,4,5] nitrenes,[6,7] azomethine ylides,[8,9] radicals,[10,11,12,13] and plasmas.[14,15] The pioneering work of oxidative treatment of CNT with the formation of carboxylic acids groups was an important step toward the surface functionalization.[16,17] Since, the attachment of small organic molecules was advantageous in tuning the properties of CNT, much attention has been paid to covalent functionalization of CNT with polymers.[18] Polymers exhibit a wide range of reactivity and structure, and their post-functionalization contributes an additional advantage in tuning properties of CNT. Covalent modification with polymers involves "*grafting to*" and "*grafting from*" methods.[18,19,20] "*Grafting to*" allows the characterization of polymers prior to grafting, but only few chains can be grafted by this method due to steric repulsion between the grafted chains and the reacting chain. On the other hand, "*grafting from*" involves multiple steps and polymers are grafted from the initiators immobilized on the nanotube surface. By this approach, a higher graft density can be obtained, but the polymer needs to be cleaved from the nanotube surface for characterization.

Outstanding progress has been made towards the use of "reversible-deactivation radical polymerization" methods due to their versatility towards different types of monomers and fine control on the molecular weight, functionality, architecture, and composition of polymers.[21] Over the past decade, reversible-deactivation radical polymerization viz. atom transfer radical polymerization (ATRP), reversible addition fragmentation chain-transfer polymerization (RAFT), and nitroxide-mediated living radical polymerization (NMRP) have been employed to graft tailored polymers onto the surface of CNT to

improve their solubility and dispersion in matrix polymer. Over the past twenty years, nitroxide-mediated living radical polymerization (NMRP) has witnessed large progress in terms of synthesis of polymers with well-defined architecture, molecular weight, and narrow polydispersity index (PDI).[22] The synthesized polymers are end capped with thermally labile nitroxide functionalities, capable of forming polymer centered radicals that could be used to add to C=C bond present on the side wall of nanotubes, similar to what has been used to functionalize the C_{60} molecule.[23,24,25]

Herein, we report the use of NMRP to synthesize well defined, narrow polydispersity polystyrenes of four number average molecular weights, their addition to the SWCNT surface, and the characterization of SWCNT-*g*-PS/PS nanocomposites by electrical conductivity and differential scanning calorimetry measurements. The goal of the study is to understand how different chain lengths of grafted polystyrene affect the dispersion of SWCNT in the host polymer.

2.2 Experimental Section

2.2.1 Materials. Styrene was purchased from Acros and purified by passing through basic alumina (Al_2O_3, activated, ~ 150 mesh, 58 Å, Aldrich). Benzoyl peroxide, 1-methyl-2-pyrrolidinone (NMP, anhydrous, 99.5%) and 2,2,6,6-tetramethyl-1-piperidinyloxy (TEMPO, 98%) were purchased from Sigma-Aldrich and used as received. HiPco SWCNT (Lot # P0340) were purchased from Carbon Nanotechnologies, Inc, Houston, Texas and treated with 8 M nitric acid to improve their dispersability.[26] The composite matrix was industrial grade PS having M_n = 70,000 and M_w/M_n = 3.2. Fluoropore 0.2 μm PTFE filters were purchased from Millipore.

2.2.2 Instruments and Measurements. The molecular weight and polydispersity index (PDI) of PS samples were measured by SEC on an Agilent series 1100 chromatograph using THF as eluent (1 mL min^{-1}) at 40 °C with differential refractive index detection and two Polymer Laboratories columns (PL gel 10 μm mixed B, 300 mm length x 7.5 mm internal diameter). Polystyrene standards in the range of 600,000-800 g/mol were used for calibration. A 35 μL sample solution (5 mg mL^{-1} in THF) was injected. Thermogravimetric analyses were carried out in a nitrogen atmosphere with a Shimadzu TGA50/50H instrument. The wt% of PS grafted onto the nanotube surface was calculated from the TGA plots as 100 * [wt% HNO_3 treated SWCNT (from plot B) – wt% SWCNT-*g*-PS (from plot C, D or E)]/(wt% HNO_3 treated SWCNT) at 600 °C.

SWCNT samples were dispersed in solvents using a Fisher FS-30 160W 3QT ultrasonic cleaner or a Microson XL-2000 22 KHz ultrasonic cell disruptor. The dispersions were filtered using a vacuum glass filtration cell and 0.2 μm PTFE filters. SWCNT-*g*-PS were precipitated using a DAMON IEC EXD centrifuge. Raman spectroscopy was carried out using a Coherent He-Ne laser at 633 nm at 20 mW using a dry powder samples. The scan time was 10 s. Atomic force micrographs were obtained using a Multimode Nanoscope IIIa SPM (Digital Instruments, Santa Barbara, CA) in tapping mode. The samples were prepared by applying a drop of dispersion to a mica chip for 5 min, removing the extra liquid with filter paper, and drying the substrate under nitrogen. STEM images were obtained with a JEOL JEM-2100 Scanning Transmission Electron Microscope at 200 kV accelerating voltage. The samples were prepared by diluting 1 mL (1 mg of SWCNT) of a SWCNT-*g*-PS dispersion in NMP with 20 mL of THF, collecting the solid on a PTFE filter, washing the solid with 100 mL of THF,

dispersing the solid into 20 mL of THF, bath sonicating for 5 min, and depositing 3-4 drops of the THF dispersion onto ultrathin carbon film/holey carbon 400 mesh copper grids (Ted Pella, Inc.). UV/vis/NIR spectra were obtained using a Varian 5000 spectrophotometer. Stock dispersions of 0.015 g SWCNT L^{-1} in NMP were centrifuged for 30 min at 540 x *g* and allowed to stand for 3 h. Light grey colored supernatant solution was used to obtain the spectra. DSC data were recorded at the scan rate of 10 °C min^{-1} after holding at elevated temperature followed by quick cool. Further details are given in our previous publication.[27]

2.2.3 Synthesis of TEMPO ended Polystyrene. PS-TEMPO samples were synthesized by similar methods described elsewhere.[28,29] A 150 mL dried three necked round bottomed flask was charged with benzoyl peroxide (400 mg, 1.6 mmol), TEMPO (480 mg, 3 mmol), styrene (40 g, 385 mmol), and a magnetic stirrer. The nitrogen gas was bubbled through the reaction mixture for 30 min, and then the flask was immersed into the oil-bath at 130 ^{o}C for 24 h. The solid PS samples were isolated by dissolving the mixture in CH_2Cl_2 (DCM) and precipitating into large excess of methanol. Re-dissolving in DCM and precipitation in methanol continued until sample contains no styrene monomer. The complete removal of styrene monomer was confirmed by ^{1}H-NMR spectroscopy. The samples were vacuum-dried at room temperature for 12 h.

2.2.4 Livingness of TEMPO Ended Polystyrene. Livingness of TEMPO ended polystyrenes were tested on all PS-TEMPO samples following the procedure described elsewhere.[30] A 25 mL three-necked round bottomed flask was charged with macroinitator PS2270-TEMPO (49 mg, 21.5 μmol) and inhibitor free styrene (20 mL, 175 mmol, 8750 eq.). The nitrogen gas was bubbled through the mixture for 30 min, and the flask was

immersed into the oil-bath at 130 ^{o}C for 4 h under constant stirring. The flask was cooled to room temperature and the contents were diluted with dichloromethane. The mixture was precipitated in large excess of methanol, and dried overnight at 70 ^{o}C under vacuum. The solid obtained was characterized by GPC analysis to estimate molecular weight and molecular weight distribution. A control experiment was carried out by heating the styrene monomer in absence of any macroinitiator under the same reaction conditions resulting in the synthesis of polystyrene of lower molecular weight and broader polydispersity index to other synthesized PS using PS-TEMPO as a macro initiator.

2.2.5 Synthesis of Polystyrene-Functionalized SWCNT. Prior to the functionalization, SWCNT were treated with 8 M nitric acid under bath sonication for 2 h at 40 ^{o}C.[26] The carboxylic acid functionalized nanotubes were dispersed in 1-methyl-2-pyrrolidinone (NMP), bath sonicated for 1 h at room temperature followed by 24 h magnetic stirring. The SWCNT dispersed in NMP were functionalized with TEMPO ended PS, a method similar to Lou.[31] A 150 mL round-bottomed flask was charged with 50 mL of SWCNT/NMP (0.5 g L^{-1}) dispersion. Nitrogen gas was bubbled through the solution for 30 min, followed by bath sonication at room temperature for 1 h, continuously purging with nitrogen. The PS solution prepared by dissolving 1.25 g of PS-TEMPO in 5 mL of NMP with stirring at room temperature for 4 h was added to the SWCNT dispersion. The nitrogen gas was bubbled through the mixture for 30 min. The flask was sealed and immersed in an oil bath at 130 °C for 24 h. The resulting mixture of SWCNT-*g*-PS and free PS was diluted with 20-fold of THF and centrifuged for 30 min at 540 x *g*. The supernatant liquid was removed, and the sample was redispersed in THF and re-centrifuged. The cycle of centrifugation and redispersion in THF was repeated

three times to obtain polystyrene-grafted SWCNT perfectly free of the unbound (free) polystyrene. Then the mixture was filtered through a 0.2 μm PTFE membrane using a vacuum glass filtration cell and washed on the filter with THF until a few drops of filtrate showed no precipitate in excess methanol. The SWCNT-*g*-PS free from PS was dispersed in NMP solvent at the concentration of 0.5 g L^{-1}, bath sonicated for 15 min at 23 °C and stirred magnetically for 24 h. The SWCNT remained dispersed in NMP for at least 3 months, but were used for composite preparation immediately after dispersing PS free SWCNT-*g*-PS in NMP solvent.

2.2.6 Composite Preparation. The concentration of SWCNT in NMP (g L^{-1}) was measured by filtering 10 mL of SWCNT-*g*-PS/NMP dispersion on a pre-weighted PTFE filter. The solid on the filter was washed with THF and vacuum dried at 70 ^{o}C for 24 h. The amount of SWCNT-*g*-PS deposited on the PTFE filter was estimated from the weight difference of PTFE filter before and after the deposition. The weight of deposited solids and wt% of grafted PS on the SWCNT obtained from TGA analysis were used to estimate the amount of SWCNT dispersed in NMP solvent. The SWCNT-*g*-PS/NMP dispersions were diluted to 0.045 g L^{-1} by adding required volume of NMP and stirred for 1 h. Dispersions of SWCNT-*g*-PS and matrix PS in NMP (10 g L^{-1}) were mixed to yield the desired weight fraction of SWCNT-*g*-PS in the final composite. The mixture was stirred for 1 h at room temperature and coagulated by dropwise addition to an excess of distilled water (V_{NMP}/V_{WATER} = 1:10) under vigorous mechanical stirring. The composite was filtered, washed with water and methanol, and dried under vacuum at 70 ^{o}C for 24 h.

2.3 Results and Discussion

2.3.1 Synthesis of TEMPO-ended Polystyrene. Nitroxide-terminated polystyrene (PS) samples were prepared by "living" free radical polymerization utilizing 2,2,6,6-tetramethyl-1-piperidinyloxy (Schemes 1 & 2). Table 1 summarizes the experimental conditions, number average molecular weights, and polydispersities of four TEMPO ended PS. The samples were analyzed by size exclusion chromatography, measured against commercial polystyrene standards.

Scheme 1. Synthesis of TEMPO ended Polystyrene

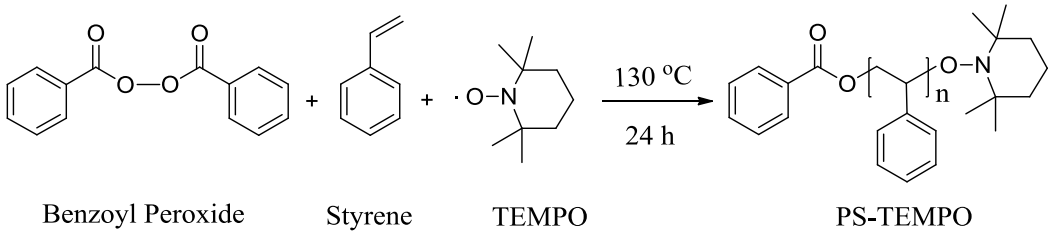

Benzoyl Peroxide Styrene TEMPO PS-TEMPO

Scheme 2. Mechanism of Synthesis of TEMPO ended Polystyrene

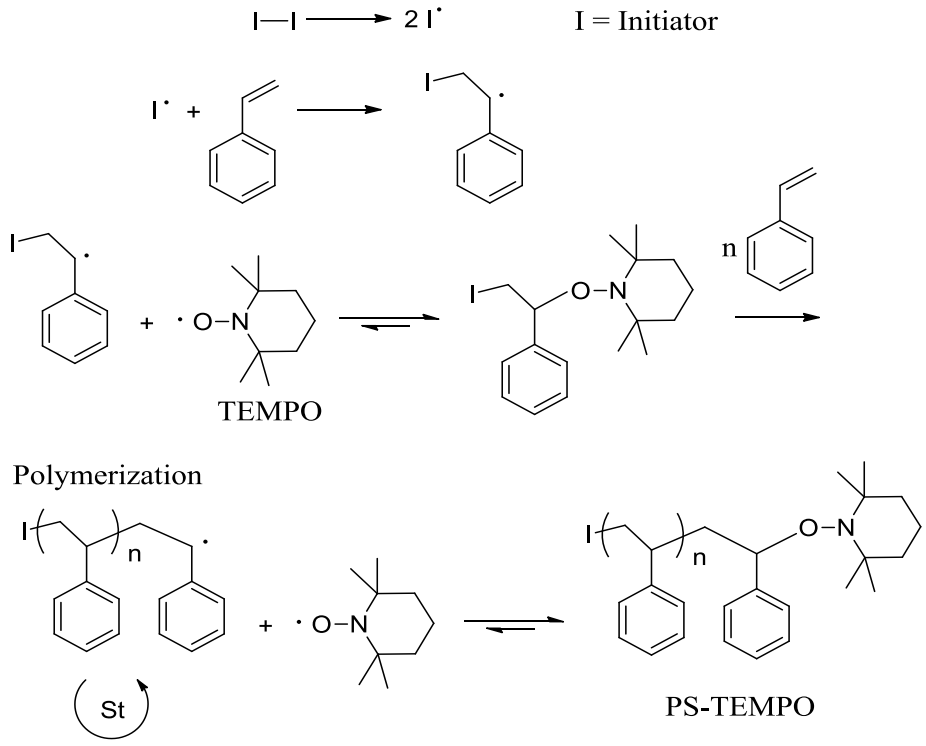

Table 1. Reaction Conditions and Properties of PS-TEMPO

sample	time (h) at 130 °C[a]	% yield	M_n (g mol^{-1})	M_w/M_n	chain extension	M_n (g mol^{-1})	M_w/M_n
					storage time (months)[b]		
PS2270	5	14	2,270	1.13	14	212,000	1.70
PS2850	5	14	2,850	1.11	0	141,000	1.64
PS15000	30	65	15,000	1.17	27	160,000	1.56
PS49500	72	81	49,500	1.36	24	191,000	1.91

[a]The first three samples were prepared with 1.0 wt % BPO vs. styrene and a TEMPO/BPO mol ratio of 1.9. PS49500 was prepared with 0.3 wt % BPO and TEMPO/BPO = 1.2. [b]Storage time of PS-TEMPO before chain extension.

2.3.2 Livingness of PS-TEMPO. Some PS-TEMPO samples were stored for more than a year. Therefore, chain extension reactions were carried out with a tiny amount of PS-TEMPO macroinitiator and large excess of styrene monomer (Scheme 3) to determine if the TEMPO ends were still active. The resulting polystyrenes had much higher molecular weight and broader PDI than the starting material as shown in Table 1, as expected for chain growth. A control experiment was done in the absence of PS-TEMPO under the same experimental conditions producing PS of M_n = 27,000 g/mol and PDI = 4.4, from self-initiation of styrene polymerization which proves that the products produced from chain extension reactions didn't form due to self initiation of styrene monomer.

Scheme 3. Chain Extension of PS-TEMPO in Presence of Excess Styrene Monomer

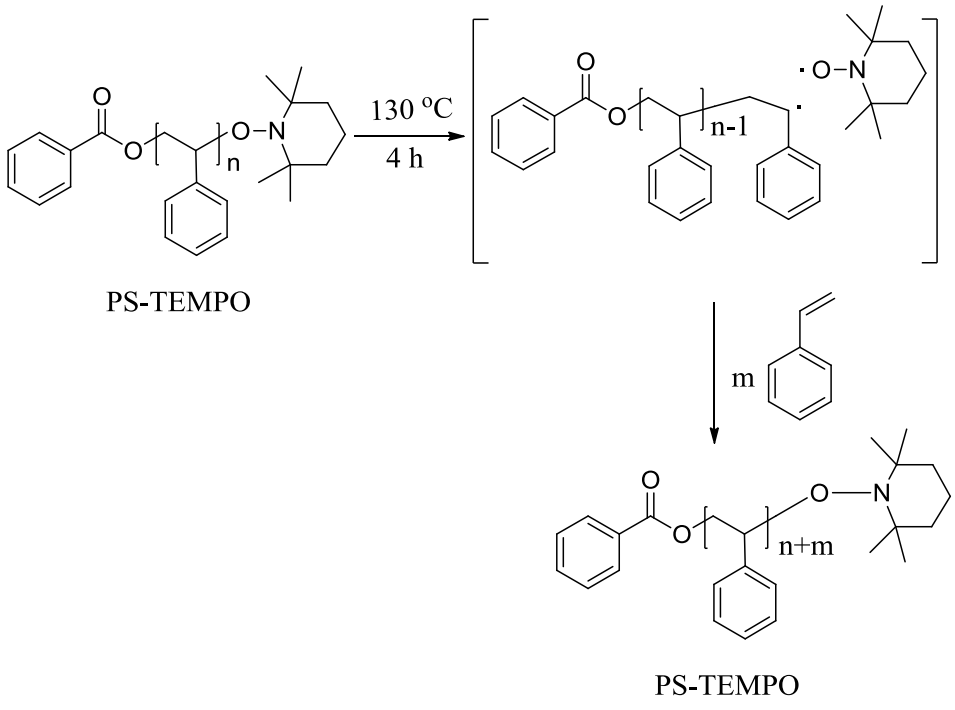

2.3.3 Functionalization of SWCNT with TEMPO Ended Polystyrene. Scheme 4 illustrates the grafting of polystyryl radicals from TEMPO-ended polystyrene (PS-TEMPO) to SWCNT by reversible deactivation. 1-Methyl-2-pyrrolidinone was chosen as the solvent for the grafting reactions because it enables the most concentrated dispersions of SWCNT of any common solvent,[32-35] and it dissolves polystyrene. In order for many polystyryl radicals to add to SWCNT, there must be a large surface area of SWCNT available to react. Higher dispersability of SWCNT corresponds to smaller bundles and greater surface area. HiPco SWCNT was lightly oxidized with nitric acid to improve the dispersability. The grafting reaction was conducted by stirring the dormant polymer and SWCNT in NMP at 130 ^{o}C for different intervals of time. Typically, 50-fold weight excess of PS-TEMPO was used with respect to the SWCNT. After grafting, SWCNT-*g*-PS mixture was added to excess THF, and SWCNT material was separated from the excess of soluble ungrafted PS by repeated centrifuging, decanting, and washing with THF followed by filtration. Increasing the amount of PS-TEMPO (2850 g/mol) above 50-fold to the weight of SWCNT for grafting reactions did not increase the wt% of grafted PS. This suggests that the grafting density depends on the molecular weight of the polymer and not on the concentration of the polymer which was also reported before.[36]

Scheme 4. Grafting of PS-TEMPO to SWCNT

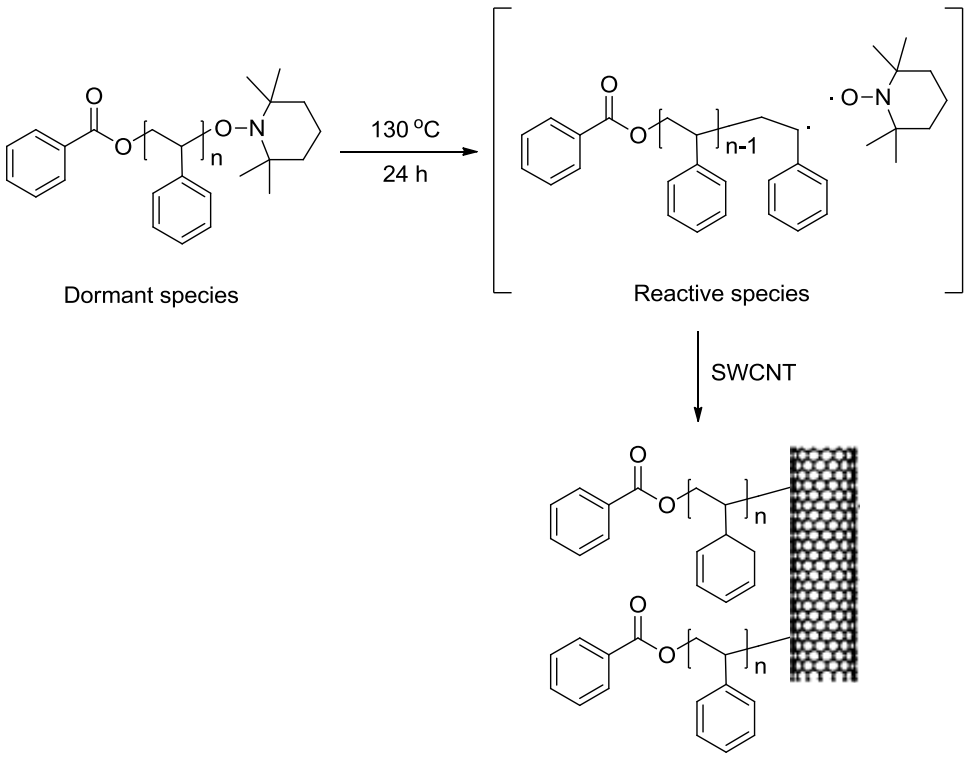

Initially, we tried to remove the ungrafted PS from the SWCNT-*g*-PS by filtering without prior centrifugation, but nanotubes passed through the 0.2 μm PTFE filter. A similar observation was reported for MWCNT-*g*-PS in THF.[37] The nanotube material in the filtrate and the nanotube material on the filter were examined by AFM (Figure 1) and appeared to be the same except for thicker bundles on the filter. Apparently, the grafted PS lubricates the SWCNT surface for passing through the pores of the PTFE membrane.

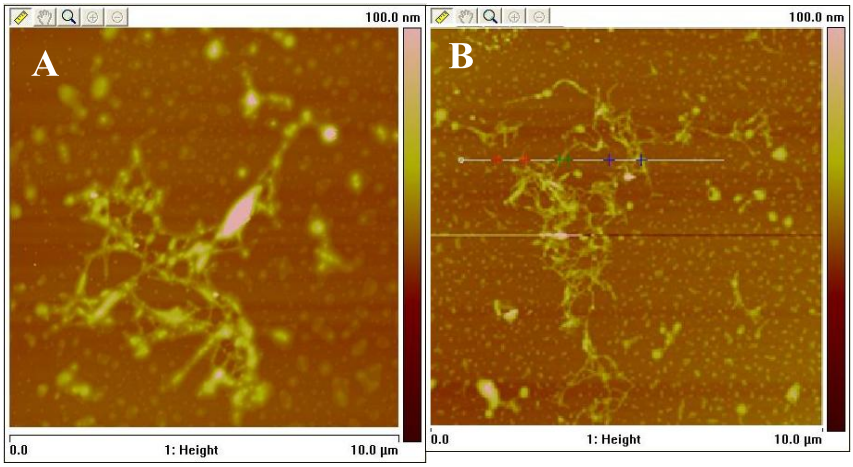

Figure 1. 10 μm x 10 μm AFM images of SWCNT-*g*-PS (M_n = 15,000 g/mol) recovered from the (A) PTFE filter, and (B) recovered from the filtrate.

2.3.4 Thermogravimetric Analysis. The weight percent of PS chains grafted to SWCNT was measured by thermogravimetric analysis (TGA). Figure 2 compares the TGA results for HiPco SWCNT, nitric acid treated SWCNT, SWCNT-*g*-PS, and pure PS under the nitrogen atmosphere. The pristine SWCNT are stable up to 600 ^{o}C (A in Figure 2). PS grafted onto the SWCNT degraded between 300-450 ^{o}C. Approximately 20-25 weight percent of covalently grafted PS was measured from all of the SWCNT-*g*-PS samples regardless of the chain length of grafted PS. Therefore the number of grafted PS chains is approximately inversely related to the molecular weight. Similar results were obtained for grafting PS of number average molecular weight 2900, 57000, and 103,000 g/mol, all with narrow PDI, to the titanium dioxide by "click" coupling reaction.[36] About ~19 wt% of PS, M_n = 2900 g/mol, was covalently grafted onto the TiO_2. Approximately 38-39.5 wt% of PS was grafted for the rest of PS samples with M_n = 57000 and 103000 g mol^{-1}. The graft densities of PS chains per 1000 carbon atoms of SWCNT are reported in

Table 2. A similar inverse relationship of grafted chain length and graft density of SWCNT-*g*-PS from nitroxide-mediated radical polymerization has been reported before, but with 39-53 weight percent PS grafted.[37] The higher graft densities are likely due to the use of shortened, better dispersed SWCNT and/or a different nitroxyl chain reactivating end group. Since PS has no favorable interaction energy with SWCNT, the grafted PS chains during the grafting reaction likely have a mushroom conformation that sterically hinders attack of a new PS radical to the surface of the SWCNT bundle that lies under the mushroom. SWCNT-*g*-PS2850 with varied graft densities were prepared by varying grafting reaction time reported in Table 2.

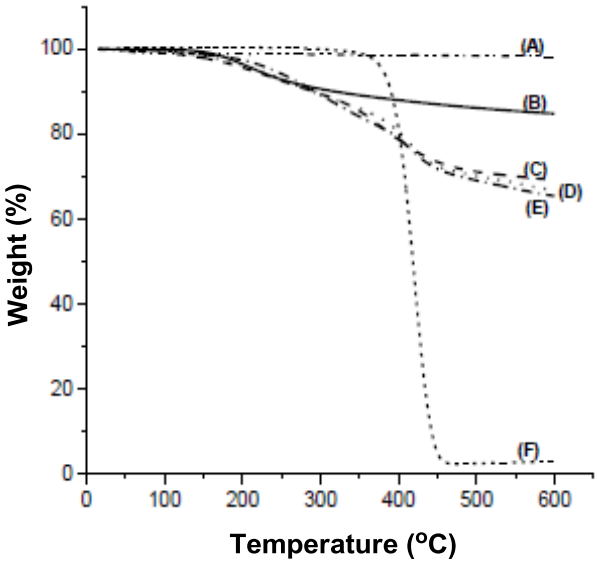

Figure 2. Thermogravimetric analysis under nitrogen at 5 ^{o}C min^{-1} of (A) HiPco SWCNT, (B) nitric acid treated SWCNT, (C) SWCNT-*g*-PS2270, (D) SWCNT-*g*-PS15000, (E) SWCNT-*g*-PS49500, and (F) PS49,500.

Table 2. TGA Results from SWCNT-*g*-PS

M_n g/mol	reaction temperature (^oC)	reaction time (h)	PS wt loss (%)	graft density[a]
2270	130	24	20	1.31
2850	130	24	22	1.18
2850	130	6.0	20	1.04
2850	130	3.0	20	1.04
2850	130	1.0[b]	18	0.93
2850	130	0.25[c]	15	0.74
2850	100	0.25[d]	12	0.58
2850	100	0.25[e]	8	0.36
15,000	130	24	23	0.23
49,500	130	24	25	0.08

[a]PS chains/1000 SWCNT carbon atoms. [b-d]Reaction time was calculated starting when the temperature of the reaction mixture reached 130 ^oC. [e]Reaction time was calculated starting when the reaction mixture was immersed in the preheated oil bath.

2.3.5 Raman Spectroscopy. The resonance Raman spectra in Figure 3 provide qualitative information about the functionalization of SWCNT by PS. The relative intensities of the disorder induced D-band at ~1350 cm^{-1} due to sp^3-hybridized carbon atoms and the tangential mode G-band at ~1580 cm^{-1} indicate differences in the degree of functionalization.[38] The Raman spectra show little difference of D/G intensities between the starting nitric acid treated SWCNT and the SWCNT-*g*-PS materials having different molecular weights. Overall, results of Raman analysis suggest that, functionalization by PS had little effect on the structure of the sidewalls and therefore little effect on the

inherent electronic properties of the SWCNT which depend on electron delocalization along the length of the tube.

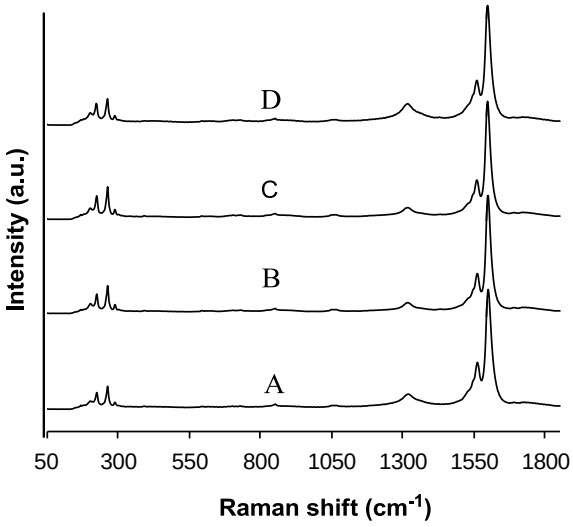

Figure 3. Raman spectra of (A) nitric acid treated SWCNT, (B) SWCNT-*g*-PS2270, (C) SWCNT-*g*-PS15000, and (D) SWCNT-*g*-PS49500.

2.3.6 VIS/NIR Spectroscopy. Figure 4 displays visible-NIR absorption spectra of SWCNT before and after HNO_3 treatment and of the SWCNT-*g*-PS of different molecular weights. The spectral region at >1000 nm shows the lowest energy electronic transitions of semiconducting SWCNT. Since HiPco SWCNT contain 33 distinguishable types of semiconducting tubes, differing in diameter and chirality, each peak in this region is due to a different type of SWCNT or to overlap of the bands of more than one type of SWCNT.[39] Although there are differences between the spectra, and the SWCNT prior to grafting have stronger peaks in the NIR, the appearance of distinct peaks in the spectra of the SWCNT-*g*-PS proves that the degrees of functionalization by HNO_3

treatment and by PS grafting are relatively low. For comparison, SWCNT shortened by more severe HNO_3 treatment lack these vis-NIR spectral peaks and have much broader D-bands in Raman spectra.[40] Highly functionalized SWCNT have no distinct bands at all in NIR spectra.[41,42]

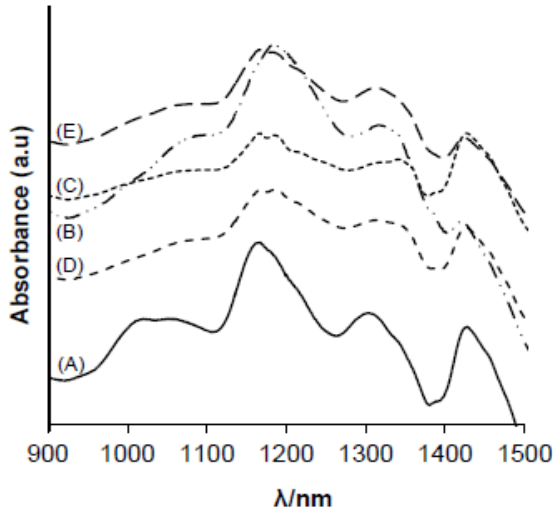

Figure 4. NIR and visible spectra of supernatant dispersions of SWCNT-*g*-PS samples (A) HiPco SWCNT, (B) nitric acid treated SWCNT, (C) SWCNT-*g*-PS2270, (D) SWCNT-*g*-PS15000, and (E) SWCNT-*g*-PS49500.

2.3.7 STEM Analysis. Dispersions of the SWCNT-*g*-PS were coated onto holey carbon grids for transmission electron micrographs as shown in Figures 5 and 6. Images of the nitric acid treated SWCNT and SWCNT-*g*-PS49500 are shown in Figure 5. The lower resolution images in Figures 5A and 5C show long bundles of a wide range of diameters over holes of the grids. The bundles in general are not uniform in diameter, which means for larger bundles that different numbers of tubes comprise the diameters at

different points over the length of the bundle. The higher resolution images of Figures 5B and 5D show a few black spots <5 nm in diameter which we attribute to catalysts from manufacture of SWCNT that were not removed by the mild nitric acid treatment. Nitric acid washing at elevated temperatures cannot always remove metal impurities completely because these metal nanoparticles are sheathed by several graphene sheets.[43] The grafted PS chains of molecular weight 15000 and 49500 g/mol exist in clumps like structures seen in STEM images. The graft densities in both cases were low compared to SWCNT-*g*-PS2850. At extremely low grafting densities polymer chains fill a mushroom shaped space on a surface.

Figure 5D shows bundles of varied sizes, the individual parallel SWCNT in the bundles, and clumps of non-SWCNT material on the surface of bundles, which is likely due to PS or to electron beam damage. The smallest diameter of a bundle in Figure 5D is 2.3 nm, about the width of two SWCNT. Thus, the 25 weight percent of PS is not coated as a monolayer on the SWCNT bundles. The STEM images reveal that polystyrene clumps rather than smooth coatings are formed on the SWCNT surface. Figure 6 shows smaller SWCNT bundles for SWCNT-*g*-PS than for pristine SWCNT.

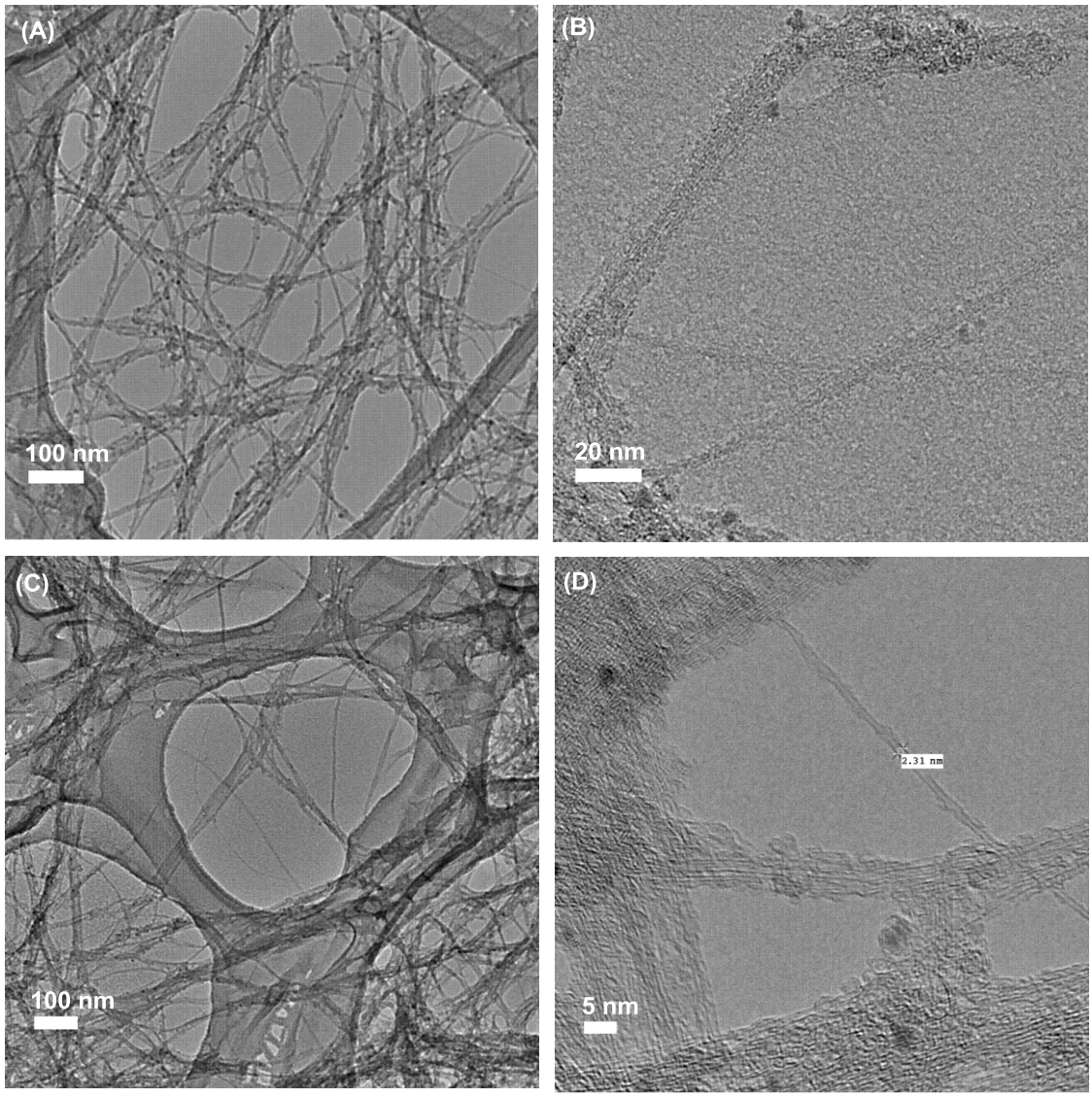

Figure 5. STEM images of (A, B) nitric acid treated SWCNT; (C, D) SWCNT-*g*-PS from 49,500 molecular weight PS. The diameter of the nanotube bundle marked in (D) is 2.31 nm.

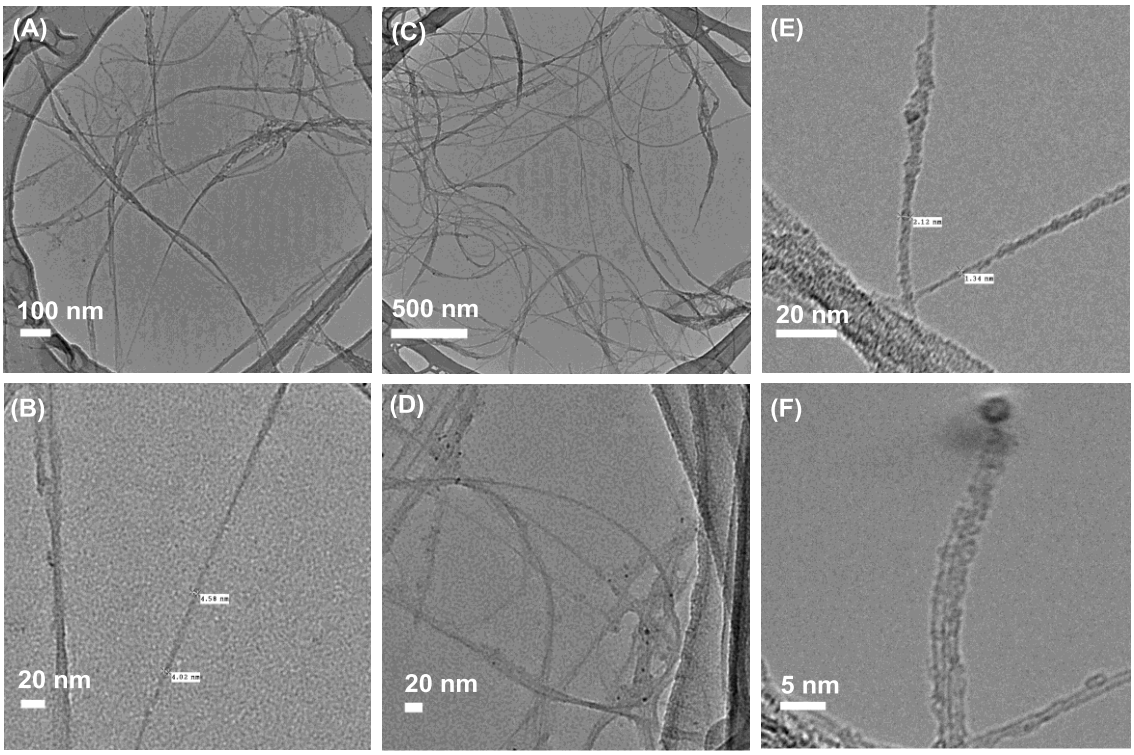

Figure 6. STEM images of SWCNT-*g*-PS (A, B) M_n = 2270, (C, D) M_n = 15,000, (E, F) M_n = 49,500. In B the diameters at the two different marked points of a bundle are 4.58 and 4.02 nm. In E the diameters at the two different marked points are 2.12 and 1.34 nm, which correspond to two and one SWCNT diameters respectively. In F four and two SWCNT in different bundles appear clearly. Figure 6F shows disintegrated carbon structure due to high voltage electron beams.

2.4 SWCNT-*graft*-Polystyrene/PS Nanocomposites. Nanocomposites with varied wt% of SWCNT were prepared by mixing SWCNT-*g*-PS and matrix PS in NMP, and precipitating the mixture into a large excess of water as shown in Figure 7. The precipitates were dried under vacuum at 70 ^{o}C for 24 h. Matrix PS had a higher molecular weight (M_n = 70,000 g mol^{-1}) and a broader polydispersity (M_w/M_n = 3.0) than all PS samples grafted to the SWCNT. The quantities of composites available with nanotube

content >6 wt% were only enough for DSC measurements, and hence we could not measure electrical or mechanical properties for those samples. On the other hand, composites for electrical conductivity measurements containing 0 to 3.0 wt% of SWCNT were pressed into films of dimensions 1.5 cm x 1.5 cm x 0.5 mm at 176 ^{o}C under 10,000 psi pressure shown in Figure 8. The mold was cooled to room temperature on the plates under atmospheric pressure before removing the composite film.

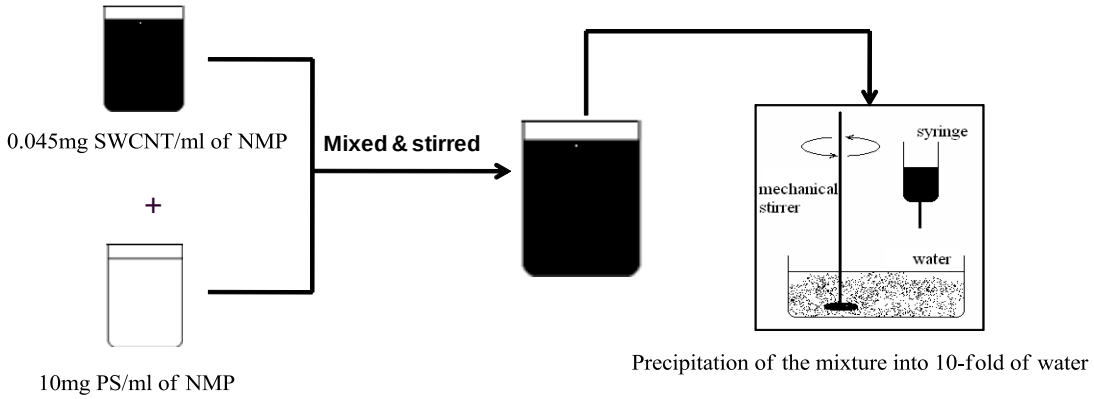

Figure 7. Preparation of 1 wt% composite of SWCNT and PS dispersions in NMP.

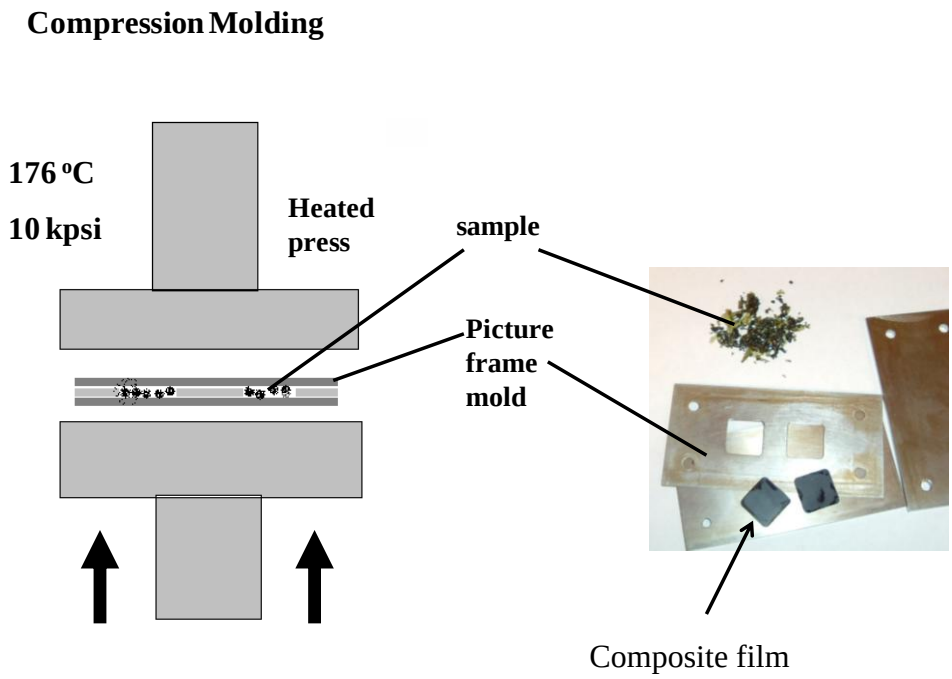

Figure 8. Preparation of composite films.

2.4.1 Electrical Conductivity. Figure 9 shows the electrical conductivity of PS composites made with SWCNT-*g*-PS (B, C, and D) and nitric acid treated SWCNT (A) measured by a two-probe technique. The conductivity was measured at 6 different places and the average value is reported. All SWCNT-*g*-PS/PS composites have very low conductivity and had no percolation threshold even at 3.0 wt% of SWCNT loading. We attribute this low conductivity to the presence of thick insulating polystyrene coatings on the nanotube surface, which prevent nanotube-to-nanotube (single or bundles) electrical contacts. However, composites of PS prepared by utilizing lightly oxidized SWCNT with no grafted polystyrene in DMF instead of NMP, have shown high conductivity and percolation threshold at 0.5 wt% of SWCNT.[44]

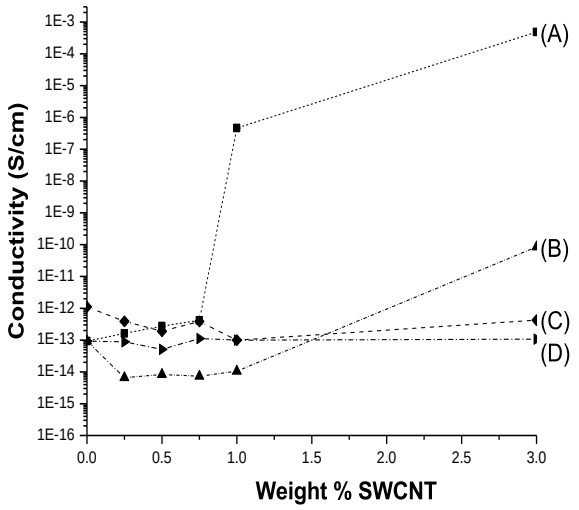

Figure 9. Electrical conductivity of (A) nitric acid treated SWCNT, (B) SWCNT-*g*-PS2850, (C) SWCNT-*g*-PS15000, and (D) SWCNT-*g*-PS49500.

2.4.2 Thermal Analysis. Previously[27] we investigated the effect of carboxylic acid functionalized SWCNT loading on the glass transition temperature (T_g) and the change in heat capacity (ΔC_p) at the T_g of SWCNT/PS nanocomposites. The glass transition temperature (T_g) increased at low nanotube fractions to a constant value about 6-7 ^oC higher than the T_g of pure polystyrene, and did not change further as the nanotube amount changed from 1 to 30 wt %. In this work we used the same carboxylic acid treated SWCNT to graft three different number average molecular weight polystyrenes and study the change in T_g and ΔC_p as a function of SWCNT loadings. Figures 10-17 show how varied amounts of SWCNT-*g*-PS affect T_g and ΔC_p of the composites, made with different chain lengths of grafted SWCNT. The change in heat capacity is normalized as per weight of total PS, both matrix PS and grafted PS. Figures 10 and 11 report data for

composites made from SWCNT-*g*-PS2850 with two different graft densities. The values of T_g increase to 106-108 ^oC at 6 wt% SWCNT, and form a plateau reaching a maximum value of 108-110 ^oC with further filler additions. However, the T_g values at 1-2 wt% SWCNT for the samples are different. Figures 12 and 13 show the effect of 15000 and 49500 g mol^{-1} grafted SWCNT loadings on the T_g and ΔC_p of nanocomposites. The T_g values for composites of SWCNT-*g*-PS15000 increase to 108-110 ^oC at 6 wt%, whereas for SWCNT-*g*-PS49500 composites increased to 104-106 ^oC at 6 wt% SWCNT. Thus, composites of SWCNT-*g*-PS with all lengths of grafted PS chains increase in T_g to a plateau at higher weight fraction of SWCNT. A similar trend was also observed for SiO_2-*g*-PS/PS nanocomposites.[45] The increase in T_g is due to a strong interfacial interaction between the matrix PS and the filler. The grafted PS chains extend into the matrix PS and occupy a sizable volume fraction of the nanocomposites. Both these effects lead to restricted chain mobility of matrix PS resulting in an increase in T_g. No change in T_g after 6 wt% of SWCNT reveals that the relaxation behavior of the matrix polystyrene is not affected after certain weight fraction of polystyrene modified SWCNT.[46] The ΔC_p in both cases for SWCNT-*g*-PS2850 decreased from 0.30-0.35 J g^{-1} $^oC^{-1}$ at 0.1 wt% SWCNT progressively to 0.15-0.20 J g^{-1} $^oC^{-1}$ at 20-25 wt% SWCNT. Thus, T_g and ΔC_p are independent of the graft densities of PS2850 chains.

Previous work on the miscibility of polymer grafted nanoparticles in a chemically identical matrix has shown that the matrix only wets the polymer brush if the melt chains are shorter than the brush.[47,48,49] However, our results are opposite to their findings. The results of T_g and ΔC_p of SWCNT-*g*-2850 composites with lower and higher graft densities suggest that SWCNT with fewer numbers of grafted PS chains can give

comparable dispersion. If dispersion is the difference between the SWCNT-*g*-PS2850 the other samples, these results suggest that the low molecular weight PS grafted SWCNT disperse well in chemically similar matrix PS. However, it is possibly not the molecular weight of the grafted PS is critical; that is the graft density of low molecular weight PS is higher than that of the other samples. Hence, higher dispersion of low molecular weight materials than that of the other samples could be due to higher graft density.

The ΔC_p for composites made from SWCNT grafted with 15000 and 49500 g mol^{-1} PS chains had little or no change with filler loading. We attribute this result to the "dewetting" between the matrix PS and the SWCNT-*g*-PS resulting in an agglomeration and poor dispersion of SWCNT. In case of SWCNT-*g*-PS15000, 20 wt% SWCNT composite has shown drastic decrease in ΔC_p. We attribute this abrupt decrease to an unknown systematic error in the sample. In summary, a small amount of SWCNT can significantly affect both T_g and ΔC_p of SWCNT/PS composite. To check the reproducibility of composite preparation, several composite samples were prepared again independently using freshly prepared SWCNT-*g*-PS and the same matrix PS. Both T_g and ΔC_p values were in close proximity to the previous value for the same weight percentage of CNT. For some remade samples, represented by open symbols, the T_g and ΔC_p values were slightly different from the old values as shown in Figures 14-17 but they are within the overall range of data. The unfilled square (□) and diamond (◊) data points symbolize remade samples. The error bars represent the standard deviations.

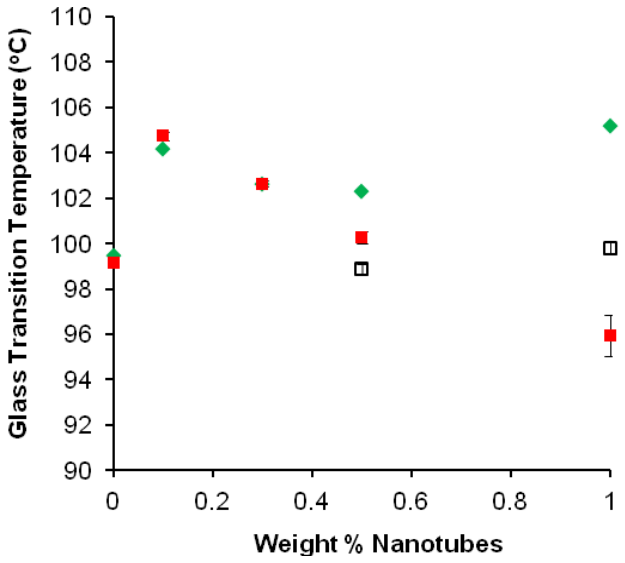

Figure 10. T_g for polystyrene filled with SWCNT-*g*-PS2850 from 0-1.0 wt% SWCNT. The graft densities for SWCNT-*g*-PS2850 are (■) 0.72 and (♦) 1.18.

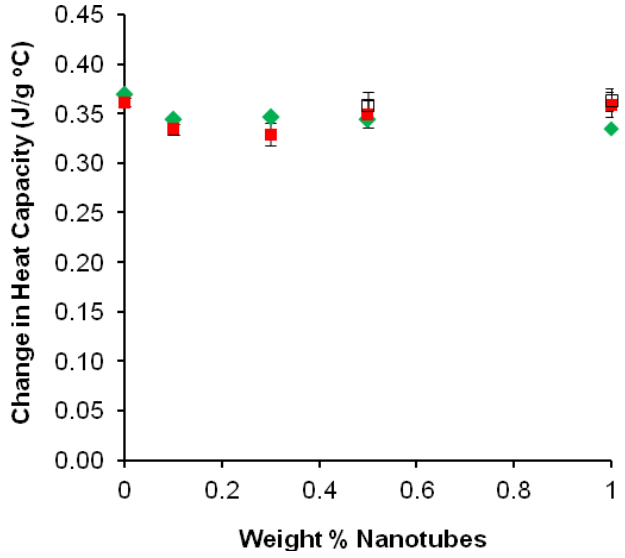

Figure 11. ΔC_p for polystyrene filled with SWCNT-*g*-PS2850 from 0-1.0 wt% SWCNT. The graft densities for SWCNT-*g*-PS2850 are (■) 0.72 and (♦) 1.18.

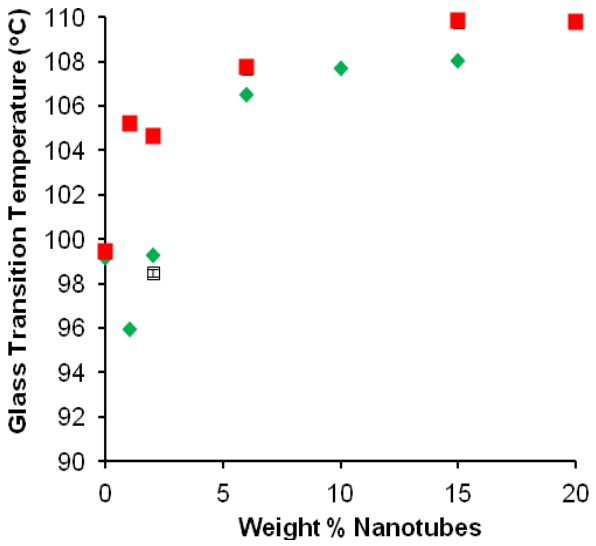

Figure 12. T_g for polystyrene filled with SWCNT-*g*-PS2850 from 0-20 wt% SWCNT. The graft densities for SWCNT-*g*-PS2850 are (■) 0.72 and (♦) 1.18.

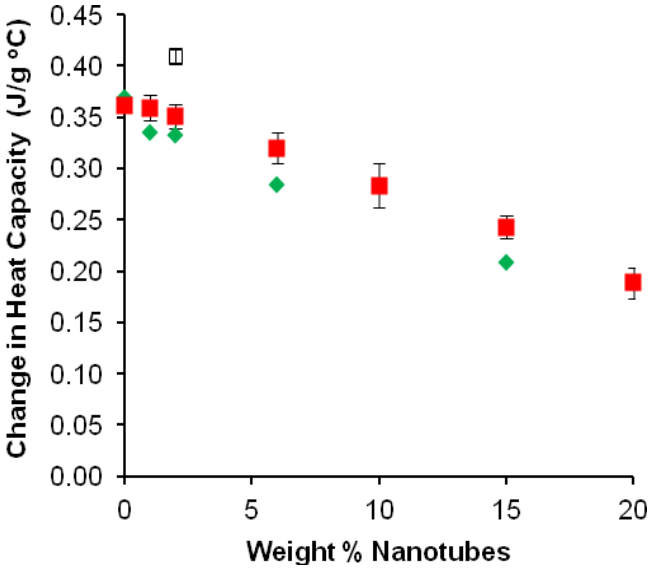

Figure 13. ΔC_p for polystyrene filled with SWCNT-*g*-PS2850 from 0-20 wt% SWCNT. The graft densities for SWCNT-*g*-PS2850 are (■) 0.72 and (♦) 1.18.

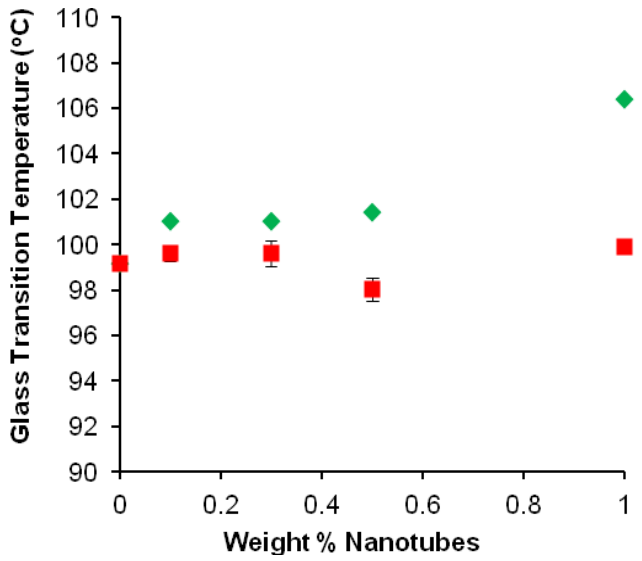

Figure 14. T_g for polystyrene filled with (♦) SWCNT-*g*-PS15000 and (■) SWCNT-*g*-PS49500 from 0-1.0 wt% SWCNT.

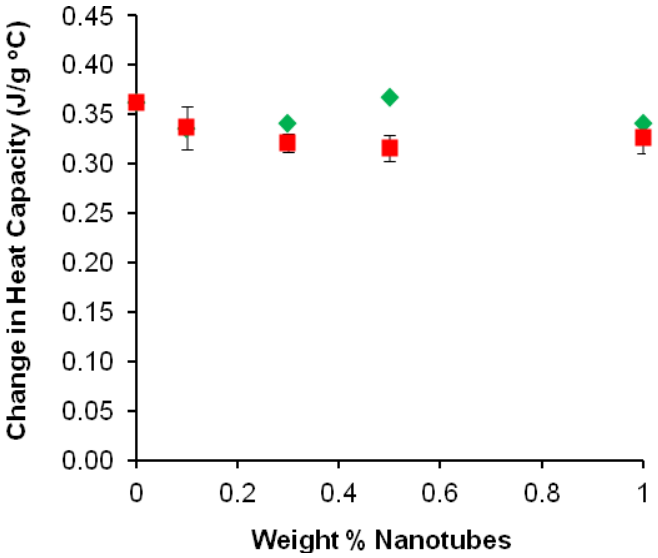

Figure 15. ΔC_p for polystyrene filled with (♦) SWCNT-*g*-PS15000 and (■) SWCNT-*g*-PS49500 from 0-1.0 wt% SWCNT.

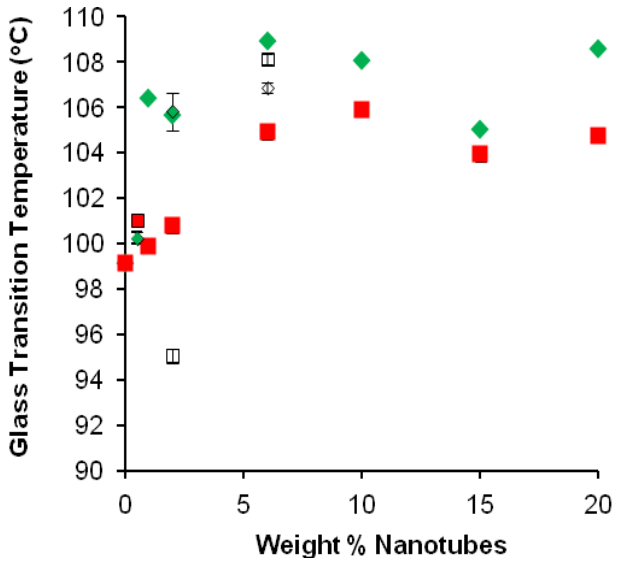

Figure 16. T_g for polystyrene filled with (♦) SWCNT-*g*-PS15000 and (■) SWCNT-*g*-PS49500 from 0-20 wt% SWCNT.

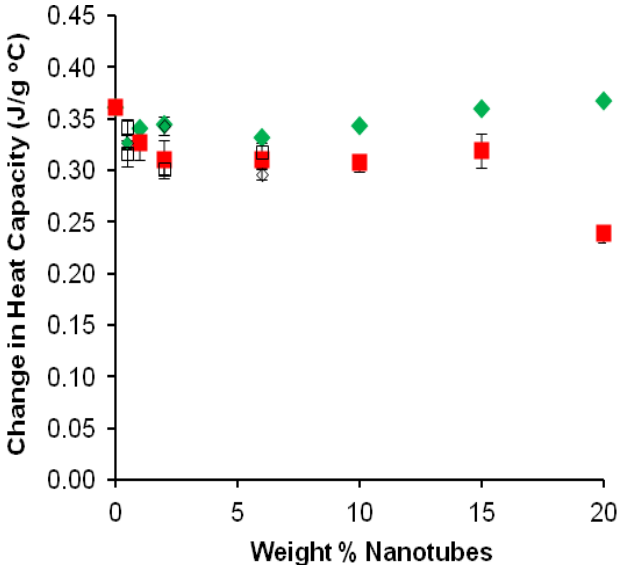

Figure 17. ΔC_p for polystyrene filled with (♦) SWCNT-*g*-PS15000 and (■) SWCNT-*g*-PS49500 from 0-20 wt% SWCNT.

2.5 Conclusions

Single-walled carbon nanotubes were functionalized with PS by radical addition. The Raman and NIR spectra of SWCNT-*g*-PS for all the grafted chain lengths indicate that functionalization had little effect on the electronic properties of the SWCNT. One of our key findings is that the weight percentage of grafted polymer is independent of molecular weight of the grafted polystyrene, which suggests that nanotube surface can only accommodate a fixed number of styrene units. SWCNT-*g*-PS/PS composites had low electrical conductivity and showed no percolation threshold of electrical conductivity due to thick polymer coatings onto the tubes. The T_g of the matrix PS increased from 99 to ~108 ^oC at 6 wt% SWCNT for all lengths of grafted PS, and formed a plateau with little change in T_g at higher filler loadings. The ΔC_p continued to decrease as SWCNT content increased for SWCNT-*g*-PS2850 composites for two different graft densities; whereas composites containing SWCNT with other higher molecular weight PS had no change in ΔC_p. This implies that the number of nanotubes that participate in the glass transition of composites reaches an asymptotic limit after 6 wt% SWCNT loading. The qualitative and quantitative characteristics of this immobilization are affected by grafting of the same polymer of different molecular weights on the nanotube surface. This investigation has been extended to matrix polymers of narrow molecular weight distribution and varied molecular weight relative to the molecular weight of the polymer grafted to SWCNT.

References

1. Grady, B. P., *Carbon Nanotube-Polymer Composites: Manufacture, Properties, and Applications*. John Wiley & Sons: New York, 2011.
2. Schnorr, J. M.; Swager, T. M., *Chem. Mater.* **2011**, *23*, 646-657.
3. Lee, W. H.; Kim, S. J.; Lee, W. J.; Lee, J. G.; Haddon, R. C.; Reucroft, P. J., *Appl. Surf. Sc.* **2001**, *181*, 121-127.
4. Kamaras, K.; Itkis, M. E.; Hu, H.; Zhao, B.; Haddon, R. C., *Science* **2003**, *301*, 1501.
5. Holzinger, M.; Vostrowsky, O.; Hirsch, A.; Hennrich, F.; Kappes, M.; Weiss, R.; Jellen, F., *Angew. Chem. Int. Ed.* **2001**, *40*, 4002-4005.
6. Holzinger, M.; Abraham, J.; Whelan, P.; Graupner, R.; Ley, L.; Hennrich, F.; Kappes, M.; Hirsch, A., *J. Am. Chem. Soc.* **200**3, *125*, 8566-8580.
7. Holzinger, M.; Steinmetz, J.; Samaille, D.; Glerup, M.; Paillet, M.; Bernier, P.; Ley, L.; Graupner, R., *Carbon* **2004**, *42*, 941–947.
8. Georgakilas, V.; Kordatos, K.; Prato, M.; Guldi, D. M.; Holzinger, M.; Hirsch, A., *J. Am. Chem. Soc.* **2002**, *124*, 760-761.
9. Tagmatarchis, N.; Prato, M., *J. Mater. Chem.* **2004**, *14*, 437-439.
10. Peng, H.; Reverdy, P.; Khabashesku, V. N.; Margrave, J. L., *Chem. Commun.* **2003**, *39*, 362-363.
11. Peng, H.; Alemany, L. B.; Margrave, J. L.; Khabashesku, V. N., *J. Am. Chem. Soc.* **2003**, *125*, 15174-15182.
12. Umek, P.; Seo, J. W.; Hernadi, K.; Mrzel, A.; Pechy, P.; Mihailovic, D. D.; Forro, L., *Chem. Mater.* **2003**, *15*, 4751-4755.

13. Stoffelbach, F.; Aqil, A.; Jerome, C.; Jerome, R.; Detrembleur, C., *Chem. Commun.* **2005**, (36), 4532–4533.

14. Valentini, L.; Puglia, D.; Armentano, I.; Kenny, J. M., *Chem. Phys. Lett.* **2005**, *403*, 385-389.

15. Yan, Y. H.; Chan-Park, M. B.; Zhou, Q.; Li, C. M.; Yue, C. Y., *Appl. Phys. Lett.* **2005**, *87*, 213101.

16. Chen, J.; Hamon, M. A.; Hu, H.; Chen, Y.; Rao, A. M.; Eklund, P. C.; Haddon, R. C., *Science* **1998**, *282*, 95-98.

17. Hamon, M. A.; Hu, H.; Bhowmik, P.; Itkis, H. M. E.; Haddon, R. C., *Appl. Phys. A.* **2002**, *74*, 333–338.

18. Bahun, G. J.; F, C.; Homenick, C. M.; Lawson, G.; Zhu, J.; Adronov, A., The Polymer Chemistry of Carbon Nanotubes. In *Chemistry of Carbon Nanotubes*, Basiuk, V. A.; Basiuk, E. V., Eds. American Scientific Publishers: Stevenson Ranch, CA USA, 2008; pp 191-246.

19. Tasis, D.; Tagmatarchis, N.; Bianco, A.; Prato, M., *Chem. Rev.* **2006**, *106*, 1105-1136.

20. Homenick, C. M.; Lawson, G.; Adronov, A., *Polym. Rev.* **2007**, *47*, 265–290.

21. Braunecker, W. A.; Matyjaszewski, K., *Prog. Polym. Sci.* **2007**, *32*, 93–146.

22. Hawker, C. J.; Bosman, A. W.; Harth, E., *Chem. Rev.* **2001**, *101*, 3661-3688.

23. Okamura, H.; Terauchi, T.; Minoda, M.; Fukuda, T.; Komatsu, K., *Macromolecules* **1997**, *30*, 5279-5284.

24. Ford, W. T.; Lary, A. L.; Mourey, T. H., *Macromolecules* **2001**, *34*, 5819-5826.

25. Audouin, F.; Nuffer, R.; Mathis, C., *J. Polym. Sci., Part A: Polym. Chem.* **2004**,

42, 3456–3463.

26. Tchoul, M. N.; Ford, W. T.; Lolli, G.; Resasco, D. E.; Arepalli, S., *Chem. Mater.* **2007**, *19*, 5765-5772.

27. Grady, B. P.; Paul, A.; Peters, J. E.; Ford, W. T., *Macromolecules* **2009**, *42*, 6152–6158.

28. Georges, M. K.; Veregin, R. P. N.; Kazmaier, P. M.; Hamer, G. K., *Macromolecules* **1993**, *26*, 2987-2988.

29. MacLeod, P. J.; Veregin, R. P. N.; Odell, P. G.; Georges, M. K., *Macromolecules* **1997**, *30*, 2207-2208.

30. Homenick, C. M.; Sivasubramaniam, U.; Adronov, A., *Polym. Int.* **2008**, *57*, 1007-1011.

31. Lou, X.; Detrembleur, C.; Sciannamea, V.; Pagnoulle, C.; Jerome, C., Polymer **2004**, 45, 6097-6102.

32. Ausman, K. D.; Piner, R.; Lourie, O.; Ruoff, R. S., Korobov, M., *J. Phys. Chem. B.* **2000**, *104*, 8911-8915.

33. Giordani, S.; Bergin, S. D.; Nicolosi, V.; Lebedkin, S.; Kappes, M. M.; Blau, W. J.; Coleman, J. N., *J. Phys. Chem. B.* **2006**, *110*, 15708-15718.

34. Bergin, S. D.; Nicolosi, V.; Streich, P. V.; Giordani, S.; Sun, Z.; Windle, A. H.; Ryan, P.; Niraj, N. P. P.; Wang, Z.-T. T.; Carpenter, L.; Blau, W. J.; Boland, J. J.; Hamilton, J. P.; Coleman, J. N., *Adv. Mater.* **2008**, *20*, 1876–1881.

35. Bergin, S. D.; Sun, Z.; Rickard, D.; Streich, P. V.; Hamilton, J. P.; Coleman, J. N., *ACS Nano* **2009**, *3*, 2340–2350.

36. Tchoul, M. N.; Fillery, S. P.; Koerner, H.; Drummy, L. F.; Oyerokun, F. T.;

Mirau, P. A.; Durstock, M. F.; Vaia, R. A., *Chem. Mater.* **2010,** *22*, 1749-1759.

37. Baskaran, D.; Sakellariou, G.; Mays, J. W.; Bratcher, M. S., *J. Nanosci. Nanotechnol.* **2007**, *7*, 1560-1567.

38. Dresselhaus, M. S.; Jorio, A.; Hofmann, M.; Dresselhaus, G.; Saito, R., *Nano Lett.* **2010,** *10*, 751–758.

39. Bachilo, S. M.; Strano, M. S.; Kittrell, C.; Hauge, R. H.; Smalley, R. E.; Weisman, R. B., *Science* **2002**, *298*, 2361-2366.

40. Liu, Y.; Yao, Z.; Adronov, A., *Macromolecules* **2005**, *38*, 1172-1179.

41. Dyke, C. A.; Tour, J. M., *Nano Lett.* **2003**, *3*, 1215-1218.

42. Bahr, J. L.; Tour, J. M., *J. Mater. Chem.* **2002**, *12*, 1952–1958.

43. Pumera, M., *Langmuir* **2007**, *23*, 6453-6458.

44. Tchoul, M. N.; Ford, W. T.; Ha, M. L. P.; Chavez-Sumarriva, I.; Grady, B. P.; Lolli, G.; Resasco, D. E.; Arepallai, S., *Chem. Mater.* **2008,** *20*, 3120-3126.

45. Bansal, A.; Yang, H.; Li, C.; Cho, K.; Benicewicz, B. C.; Kumar, S. K.; Schadler, L. S., *Nature Materials* **2005**, *4*, 693-698.

46. Ham, H. T.; Koo, C. M.; Kim, S. O.; Choi, Y. S.; Chung, I. J., *Macromol. Res.* **2004,** *12*, 384-390.

47. Bansal, A.; Yang, H.; Li, C.; Benicewicz, B. C.; Kumar, S. K.; Schadler, L. S., *J. Polym. Sci., Part B: Polym. Phys.* **2006**, *44*, 2944–2950.

48. Hore, M. J. A.; Frischknecht, A. L.; Composto, R. J., *ACS Macro Lett.* **2012,** *1*, 115−121.

49. Dutta, N.; Green, D., *Langmuir* **2008,** *24*, 5260-5269.

CHAPTER III

POLY(METHYL METHACRYLATE) FUNCTIONALIZED SINGLE-WALLED CARBON NANOTUBE-POLYMER COMPOSITES

ABSTRACT: The thermomechanical properties of single-walled nanotubes (SWCNT) polymer composites are significantly affected by particle-polymer wetting behavior. SWCNT were lightly grafted with poly(methyl methacrylate) (PMMA) chains via reversible addition fragmentation chain transfer (RAFT) polymerization with number average molecular weights (M_n) of 22600, 26000, and 35700 g/mol and mixed with chemically identical PMMA matrices of M_n 14700, 26600, and 97200 g/mol to prepare polymer-nanocomposites. Thermogravimetric analyses showed 6 wt% of PMMA was grafted onto the nanotube surface for all molecular weights of grafted PMMA. In Raman spectra the intensity ratios of D to G bands were similar for all of the PMMA-grafted nanotube samples and the starting SWCNT. Numerous near-infrared electronic transitions were retained in all SWCNT-*g*-PMMA samples similar to the pristine SWCNT. Thus, grafting experiments have little effect on the inherent electronic properties of the nanotubes. In the so-called wet brush limit, when the grafted molecular

weight equals or exceeds the matrix value, we observed 2 ^{o}C to 8 ^{o}C increase in the glass transition temperature (T_g) of PMMA/SWCNT filled composites compared with the unfilled PMMA matrix. The increase in T_g for composites is due to the favorable interaction between the matrix and brush polymers. When the molecular weight of the matrix exceeded the graft PMMA molecular weight, we observed no change in T_g for nanocomposites up to 2 wt% SWCNT loadings which could be due to the SWCNT aggregation and macro phase separation. For nanocomposites with $M_{graft} \geq M_{matrix}$, electrical conductivity increased with SWCNT loadings to a plateau conductivity of 10^{-9} S/cm at 1.0 wt% SWCNT and percolation threshold of electrical conductivity as low as <0.25 wt% SWCNT. For nanocomposites with $M_{graft} < M_{matrix}$, conductivity started to increase after 0.5 wt% SWCNT and reached the value of 10^{-11} S/cm at 2.0 wt% SWCNT. Dynamic mechanical analyses (DMA) of nanocomposites with $M_{graft} \leq M_{matrix}$ showed moderate increase in storage modulus, E', above and below T_g. We could not do DMA measurements on PMMA nanocomposites made with $M_{graft} > M_{matrix}$ because composites samples were highly brittle and samples had multiple hairline cracks.

3.1 Introduction

Dispersing carbon nanotubes in polymer matrices has became an important strategy to enhance the mechanical, electrical, thermal, or optical properties of polymeric materials.[1,2,3] Good dispersion of SWCNT into the homopolymer matrix is often critical and is controlled by their interaction with themselves and matrix polymer chains. A common approach employed to overcome the tube-tube van der Waals forces of attraction and facilitate tube-polymer interaction is grafting of polymer chains onto the

carbon nanotube (CNT) surfaces, to prepare polymer brushes. The length, density, and conformation of polymer brushes can be engineered to modulate interactions between particles or particle-polymer.[4,5,6,7]

Previous work on polymer brushes grafted on planar surfaces[8-16] and curved surfaces[17-26] in a chemically identical matrix showed that the matrix polymer wets the polymer brush surface if the molecular weight of the matrix is less than the molecular weight of the grafts. In contrast, longer matrix chains are known to dewet the brush because the matrix chains penetrating the brush cannot overcome the translational or mixing entropy. This is called "*autophobic dewetting*". An entropic barrier can be established when the polymer chains are end-grafted to a solid substrate i.e., their chain rotations are confined in specific configurations. In such cases, the entropic decrease in free energy associated with interpretation of the homopolymer chains is bigger than any abrupt change by the loss in conformational entropy due to distortion of the substrate chains and a well defined interface is formed. Additionally, due to high degree of freedom and mobility smaller matrix chains can easily penetrate polymer brushes bigger than their size, but on increasing the molecular weight of matrix chains, mobility of chains decreases resulting in immiscibility. The excess energy associated with this interface can then destabilize the film and induce dewetting.[13] Thus, free polymer chains have higher entropy than polymers grafted on a solid substrate. Unlike brushes on planar surfaces, polymer chains end-grafted to curved surfaces face less chain crowding with increased distance from the surface. For instance, silica nanoparticles (diameter 7 ± 2 nm) are grafted with polystyrene brushes (graft density = 0.27 chains/nm^2) of degree of polymerization 1050 are mixed with matrix polystyrene to form nanocomposites.[26] The

result showed that low molecular weight (MW) matrix polystyrene with DP <880 wet these particles. Concurrently, the glass transition temperature (T_g) of the nanocomposite increases. At higher MW, the matrix does not wet the particles and the T_g decreases.

As the matrix chains and the grafted brushes are chemically identical, entropic interactions are expected to direct the chain dynamics, the glass transition temperature, T_g, and phase behavior of the systems. The first experimental autophobic dewetting study demonstrated that the polystyrene (PS) homopolymer films (degree of polymerization N_H) dewet from brushes of polyvinylpyridine-*co*-polystyrene (PVP-PS) (degree of polymerization N_{PVP} and N_{PS}), coated on the silicon wafer, when the molecular weight of polystyrene homopolymer was about 5 times greater than the molecular weight of the polystyrene present on the copolymer brushes.[13] Upon increasing the lengths of polymer brushes compared to the matrix polymer, miscibility between the brush and the matrix improves from "poor" to "good". A study using self-consistent field theory (SCFT) showed that the crossover from "*dewetting"* to complete "*wetting"* also occurs when the molecular weights of the grafted polymer chain are at least equal to the matrix polymers.[27] At high grafting density nanoparticles aggregate regardless of whether the graft molecular weight is higher or lower than the matrix molecular weight. On the other hand, at low graft density the longer grafts can better shield the nanoparticles surface from particle-particle interactions than the shorter grafts and lead to the dispersion of the polymer grafted nanoparticles in the matrix melts.[28] On increasing the graft density, miscibility between polymer brushes and matrix chains goes from "good" to "poor" because of the increase in stretching cost of the grafted chains. When polymer chains of degree of polymerization *N* are grafted onto the flat surface, the interactions between the

grafted chains and the matrix chains of the degree of polymerization of P strongly depend on the surface graft density (σ).[29] At low graft densities, $\sigma \sqrt{N} << (N/P)^2$, the melt chains penetrate into the grafted chains. With increasing σ, the melt chains begin to be excluded from the grafted chains and an interfacial structure begins to form between the grafted chains and the free melt chains.[30] Such a transition occurs at $\sigma \sqrt{N} = (P/N)^{-2}$. Therefore, a "*dry-brush*" or "*dewetting*" occurs when $\sigma \sqrt{N} > (N/P)^2$. The grafted chains do rather mix with chains from another particle than with the free melt chains. There is an effective attraction between the brushes at different particles and polymer coated particles in a melt. Increasing the curvature of the grafted particle reduces crowding of grafted chains allowing the brush chains to explore more space, resulting in less entropic loss for matrix chains to penetrate the brush layers, facilitating the "*wet-brush*" regime. Further increasing the curvature when the particle size approaches the nanoscale, the curvature of the particles becomes an important facet to be considered. In such cases the radius of gyration of grafted polymer brush is similar to the size of the nanoparticle. For example when a radius (R) of spherical gold nanoparticles is similar to the brush height, $R \approx h \approx$ 1-2 nm that is $R/R_g \approx 1$, where R_g is the radius of gyration of host polymer, with graft density $\sigma \approx 2$ chains/nm^2, h is the brush height, and $N/P = 0.2$ ($M_{n\ matrix}$ = 5000 g/mol). Under such conditions, matrix chains would not intermix with the grafted chains.[5] However, these small nanoparticles, within this dry-brush regime are dispersed well in matrix melt at the maximum 5 wt% of nanoparticles. Under similar conditions, for planar surface, *wetting/dewetting* transition occurs at $N/P \approx 1$, at slightly lower graft density. These aforementioned results suggest that for larger particles, where on length scale $R >> R_g$, the *wetting/dewetting* is strictly driven by a mixing (dispersion)/(demixing)

transition. However, for a very small particle, $R \approx 1$ nm, $R \approx$ length of a particle, l, and $R < R_g$, brush/melt interactions evidently play a less important role on the particle/polymer miscibility whereas free energy due to translational entropy plays an important role toward the miscibility of nanoparticles in the polymer melts. The translational entropy varies as $1/(R)^3$, where R is the radius of a nanoparticle. Extensive experimental work[31,32,33] on a diverse set of nanoparticles indicate that when the $R < R_g$, miscibility of particles in the polymer matrix is promoted, and electrical, thermal, and mechanical properties improvement are possible. For instance, Tuteja *et al.*[32] found that the melt viscosity of PS of MW 393 kD and R_g ~17 nm decreased to 80% with an addition of 10 wt% fullerene (R ~ 0.7 nm) due to the nanoscale phenomena. In comparison to linear polymer molecules nano sized fullerenes have much shorter time scale of diffusion. Also, fullerenes do not participate in the chain entanglement dynamics, but produce dilution effect and thereby reduce the viscosity of polymers. It should also be noted down that only spherical shaped nanoparticles, for examples fullerenes, have been shown a reduction in viscosity of composites compared to other fillers such as nanoclays and carbon nanotubes. Similar results were also reported by Mackay *et al.*[33] for PS (R = 3-5 nm) nanoparticles, with 2.5 mol% and 20 mol% crosslinker, blended with linear polymer radius of gyration (R_g) equals to 7.5–15 nm.

Kumar and co-workers studied theoretically[17] and experimentally[23,26] the dispersion of polystyrene grafted silica nanoparticles into the chemically identical polymer matrices. They found that the dispersion of nanoparticles into the polymer matrix increased (a) when the molecular weights of the grafted chains were increased compared to the matrix polymer molecular weight and (b) as the particle radius was decreased. Unlike the case of

polymer brushes on the planar surfaces, polymers grafted onto the curved surfaces tangentially spread away from the silica surface and thus lessen the packing stress that originates due to high polymer grafting densities. This results in more favorable matrix/particle interfacial interactions. They have also reported that, at the highest graft density (0.1 chains/nm^2), when the ratio of the graft chain length to the matrix chain length (α) is increased, the particles were highly soluble in the matrix polymer, but aggregated when $\alpha = 1$. For intermediate graft density (0.05 chains/nm^2), similar results were obtained until $\alpha < 1$. Similar results on wet and dry brush behavior were also reported by other groups.[17,21] Thus, particle/matrix interaction plays a crucial role in improving the dispersion of nanoparticles in the matrix polymer, and T_g is important because the elastic modulus, tensile strength, and thermal conductivity change by several orders of magnitude in the vicinity of T_g. Thus, motivated by such considerations, we probe in this study whether a similar quantitative/qualitative correlation can be established between the brush on the carbon nanotube and melts of the same structure as the grafted chains.

Recently,[34] we studied the dispersion of polystyrene grafted SWCNT in chemically identical matrix PS, where the number average molecular weight (M_n) and polydispersity index (PDI) of matrix PS were higher than those of the grafted PS chains. For all chain lengths of grafted PS, T_g of nanocomposites increased from 99 to 109 ^oC from 0 to 6 wt% SWCNT loading followed by a plateau in T_g as the nanotube contents were increased further. This kind of behavior is reported previously for SiO_2-*g*-PS/PS nanocomposites.[24] The ΔC_p continued to decrease for SWCNT grafted with PS of lowest MW from 0 to 20 wt% nanotube loadings, whereas little or no change in ΔC_p was observed for SWCNT

grafted with other lengths of PS chains. Current study focuses on extending this fundamental understanding of "*wetting*" and "*dewetting*" phenomena between the surfaces of SWCNT coated with PMMA mixed with chemically identical PMMA matrices when the grafted chain molecular weight, M_{graft}, is smaller, equal to, and greater than the molecular weight of PMMA matrices (M_{matrix}). In this work, we used one of the thermomechanical properties, T_g, of nanocomposites to follow the limit of "*wetting*" and "*dewetting*" between the nanoparticles and the matrix PMMA. It is well understood that the glass transition temperature (T_g) increases locally in the vicinity of a strongly interacting particle-polymer nanocomposites except for chain segments so close to particle that they undergo no motion at all.[35] Thus, such shift in T_g will also lead to a change in the temperature at which there is a rapid change in the elastic modulus, conductivity, hardness, and other physical properties of the sample, provided the particles are well dispersed in the matrix polymer.[36] Therefore, in preparing SWCNT nanocomposites with high electrical, thermal, and mechanical properties, not only inherent properties of nanotubes are important, but one must also optimize nanotube dispersion, nanotube-polymer interface chemistry, and nanoscale morphology to take advantage of the enormous surface area per unit volume of SWCNT. Herein, we report the preparation of covalently grafted poly(methyl methacrylate) of nearly equal chain lengths to the SWCNT surface, preparation of nanocomposites by incorporating SWCNT-*g*-PMMA into the chemically identical matrix chains of different lengths than grafts, and measurements of electrical, thermal, and mechanical properties of SWCNT/PMMA nanocomposites. A major goal of this work is to elucidate the wetting behavior of PMMA grafted SWCNT as a function of mechanical properties and T_g when

the graft lengths of polymer chains are smaller, equal to, and greater than the matrix chain lengths.

3.2 Experimental Section

3.2.1 Materials. Methyl methacrylate (99.0%, Aldrich) was purified by passing though basic alumina (Al_2O_3, activated, ~ 150 mesh, 58 Å, Aldrich). Thionyl chloride ($SOCl_2$, Aldrich, 99+%), tetrahydrofuran (THF, HPLC grade, Aldrich), triethylamine (TEA, Aldrich, ≥99.5%), 4-dimethylaminopyridine (DMAP, Aldrich, ≥99.0%), *N*,*N*′-dicyclohexylcarbodiimide (DCC, Aldrich, ≥99.0%), and $CDCl_3$ (Aldrich, 99.8 atom% D) were used as received. Ethylene glycol (EG, Acros, 97%) was distilled at 1 atmosphere pressure before use. 1-Methyl-2-pyrrolidinone (NMP, anhydrous, 99.5%) and ortho-dichlorobenzene (*o*-DCB) were used as received from Aldrich or Acros Chemicals. Azobisisobutyronitrile (AIBN) (Aldrich, 98%) was recrystallized from methanol prior to the use. 4-Cyano-4-(dodecylsulfanylthiocarbonyl)sulfanylpentanoic acid, min. 97% was purchased from Strem Chemicals, Inc. SWCNT (CoMoCat, Lot # SG76-000-020) was provided by Southwest Nanotechnologies, Inc., Norman, OK. Typical properties of SWCNT include: Tube diameter (0.93 ± 0.27 nm), High aspect ratio (1,000), carbon content (>90% by weight), ~ 8 to 10% Mo oxide, and >50% of tubes with (7,6) chirality. Fluoropore 0.2 μm PTFE filters were purchased from Millipore.

3.2.2 Instruments and Measurements. The molecular weight and polydispersity index (PDI) of poly(methyl methacrylate) (PMMA) samples were measured by SEC on an Agilent series 1100 chromatograph using THF as eluent (1 mL min^{-1}) at 40 °C with differential refractive index detection and single Polymer Laboratories column (PL gel 5

μm mixed B, 300 mm length x 7.5 mm internal diameter). Poly(methyl methacrylate) standards in the range 600,000-800 g/mol were used for calibration. A 35 μL sample solution (5 mg mL^{-1} in THF) was injected. Thermogravimetric analyses were carried out in a nitrogen atmosphere with METTLER TOLEDO instrument from 25-600 ^{o}C at the heating rate of 10 ^{o}C min^{-1}. The wt% of PMMA grafted onto the nanotube surface was calculated from the TGA plots as 100*[wt% RAFT agent grafted SWCNT (from plot C) – wt% SWCNT-*g*-PMMA (from plot D, E or F)]/(wt% RAFT agent grafted SWCNT) at 600 °C.

The amounts of S-atom from the RAFT agents attached to the SWCNT surface were measured by elemental analyses by combustion using automatic analyzers at Atlantic Microlab, Inc, GA. SWCNT samples were dispersed in solvents using a Fisher FS-30 160W 3QT ultrasonic cleaner or a Microson XL-2000 22 KHz ultrasonic cell disruptor. The dispersions were filtered using a vacuum glass filtration cell and 0.2 μm PTFE filters. SWCNT-*g*-PMMA were precipitated using a DAMON IEC EXD centrifuge. Raman spectroscopy was carried out on solid samples using a Coherent He-Ne laser at 633 nm at 20 mW at University of Oklahoma, Norman. The scan time was 10 s. STEM images were obtained with a JEOL JEM-2100 Scanning Transmission Electron Microscope at 200 kV accelerating voltage. The samples were prepared by diluting 1 mL (0.45 mg of SWCNT) of SWCNT-*g*-PMMA dispersion in NMP with 20 mL of THF and centrifuged at 8400 x *g* for 15 min. The redispersion of solids in THF and centrifugation were done 4 times to remove most of the NMP solvent from the mixture. The solid SWCNT-*g*-PMMA was dispersed in 2 mL of THF. The solution was bath sonicated for 5 min and 2 drops of THF dispersion was deposited onto the ultrathin carbon film/holey carbon 400 mesh copper

grids (Ted Pella, Inc.). UV/vis/NIR spectra were obtained using a Varian 5000 spectrophotometer. Stock dispersions of 0.015 g SWCNT L^{-1} in NMP were centrifuged for 30 min at 540 x *g* and allowed to stand for 3 h. The dark supernatant solution was used to obtain the spectra. DSC data of SWCNT-*g*-PMMA/PMMA nanocomposites were recorded at the scan rate of 10 °C min^{-1} after holding at elevated temperature followed by quick cool. Further details are given in our previous publication.[37] Electrical conductivities were tested by a two-point probe method with a specially constructed resistivity chamber, calibrated by a Keithley 610C Electrometer. Composite samples were molded at 180 ^{o}C by applying 1600 psi pressure for 1 min in the mold of dimension 2.5 × 2.5 × 0.02 $inch^3$. The films were cooled to room temperature under the same pressure before being removed from the mold. Composite samples with dimensions of 30 x 5 x 0.5 mm^3 were tested by dynamic mechanical analysis (DMA) on a Rheometric Scientific (now part of TA Instruments) RSA II machine with tension clamp to determine the storage and loss moduli of SWCNT-*g*-PMMA/PMMA nanocomposites as a function of temperature thereby determine the glass transition temperature (T_g) of nanocomposites. All experiments were performed with a 1 Hz frequency and 0.05% strain, and with static force tracking dynamic force. The temperature ramp tests were performed between -90 and ~250 ^{o}C. The samples were cooled with liquid nitrogen and equilibrated for 1 min at a given temperature with a 4 K interval between data points.

3.2.3 Synthesis of SWCNT-COOH. An acidic oxidative treatment of SWCNT for purification and functionalization was adopted from the literature.[38] A 500 mL glass bottle was charged with 0.34 g of SWCNT and 300 mL of dimethylformamide (DMF). The mixture was bath sonicated at 25 ^{o}C for 1 h followed by 12 h stirring. Then tubes

were vacuum filtered through a 0.2 μm PTFE filter, and washed with DI water, and small amounts of methanol. Immediately, tubes were dispersed in 680 mL of 8 M HNO_3, stirred for 10 min, and bath sonicated for 2 h at 55-60 ^oC. The solution was cooled to 25 ^oC, diluted with 200 mL of DI water, and vacuum filtered through a 0.2 μm PTFE filter. The tubes were washed with DI water until the pH reached above 6. The solid collected on the filter was washed with 30 mL of methanol and a small amount of *o*-DCB and kept wet.

3.2.4 Synthesis of SWCNT-COCl. All of the carboxylic acid bearing SWCNT were dispersed in 300 mL of $SOCl_2$ in a three necked 500 mL round bottomed flask, bath sonicated, and magnetically stirred at room temperature for 5 min in each case. Then 25 mL of *o*-DCB was added to the mixture and heated at 70 ^oC for 30 h under a dry nitrogen atmosphere. After the reaction, 50 mL of *o*-DCB was added to the flask, and the $SOCl_2$ was distilled off at 1 atm. The SWCNT-COCl in *o*-DCB were added to 300 mL of THF and vacuum filtered through a 0.2 μm PTFE filter. The solid on the PTFE filter was washed with a small amount of NMP and dispersed into anhydrous NMP at the concentration ~ 0.5 g L^{-1}. The mixture was stirred for 15 min, bath sonicated for 1 h at room temperature, and stirred for 24 h.

3.2.5 Synthesis of SWCNT-OH. A 1000 mL round bottomed flask was charged with all of the SWCNT-COCl/NMP dispersion. The mixture was tip sonicated for 15 min at 15 Watt output. Then 4-dimethylaminopyridine (DMAP) (0.13 g, 1.1 mmol), ethylene glycol (6.8 g, 6.1 mmol), and 10 mL of triethylamine were added to the solution and stirred at room temperature for 96 h under nitrogen in the dark. After the reaction, the mixture was vacuum filtered through a 0.2 μm PTFE filter and washed with THF,

methanol, and dichloromethane (CH_2Cl_2). The solid SWCNT-OH was dispersed in CH_2Cl_2, which was previously dried overnight over 3Å molecular sieves.

3.2.6 Immobilization of the RAFT Agent (CTA) on the SWCNT Surface. The RAFT agent was immobilized on the SWCNT by similar method described elsewhere for coupling hydroxyl group terminated poly(isobutylene) with RAFT agent 4-cyano-4-(dodecylsulfanylthiocarbonyl)sulfanylpentanoic acid.[39] A 1000 mL round bottomed flask was charged with all of the SWCNT-OH/CH_2Cl_2 dispersion. The mixture was bath sonicated for 30 min with constant stirring using magnetic stir bar under a dry nitrogen atmosphere. In a separate 25 mL round bottom flask, dicyclohexylcarbodiimide (DCC) (1.1 g, 5.4 mmol), dimethylaminopyridine (DMAP) (0.13 g, 1.1 mmol), 4-cyano-4-(dodecylsulfanylthiocarbonyl-sulfanyl)pentanoicacid (chain transfer agent, CTA) (1.4 g, 3.5 mmol), and 15 mL of dry CH_2Cl_2 were stirred for 10 min under a dry nitrogen atmosphere. After 10 min, the solution was added to SWCNT-OH/CH_2Cl_2 dispersion using a glass syringe. The mixture was stirred at room temperature for 24 h in dark. After the reaction, SWCNT-CTA were washed with CH_2Cl_2, methanol, and anhydrous NMP to remove residual DCC, DMAP, CTA, and DCU (dicyclohexyl urea). The weight of DCU produced in the reaction mixture was estimated from the molar amounts of DCC used in the coupling reaction. Therefore, based on the solubility data of DCU in CH_2Cl_2[40] and the expected amounts of DCU produced in the mixture, SWCNT-CTA were washed with the calculated volume of dichloromethane to remove DCU from the reaction mixture. The solids were washed with additional 100 mL of CH_2Cl_2. The SWCNT-CTA were dispersed in anhydrous NMP at the concentration ~0.5 g L^{-1}, bath sonicated for 15 min, stirred overnight under a dry nitrogen atmosphere, and used further for grafting experiments.

3.2.7 Synthesis of SWCNT-*g*-PMMA by Surface RAFT Method. A 500 mL round bottomed flask was charged with 206 ml of SWCNT-CTA/NMP dispersion (~0.5 g L^{-1}), MMA (5 g, 50 mmol) and AIBN (0.5 mg, 0.003 mmol) (50 mg AIBN dissolved in 10 ml purified MMA, from which 0.1 ml of the stock solution was taken). Four complete freeze-pump-thaw cycles were applied to remove the dissolved oxygen. The solution was bath sonicated room temperature for 15 min and immersed in an oil-bath at 90 ^{o}C for 96 h under with constant stirring. After the reaction, the mixture was quenched in liquid nitrogen, diluted with 200 ml of THF, bath sonicated for 2 min and stirred for 15 min at the room temperature. Then the mixture was centrifuged at 540 x *g* for 30 min to remove the supernatant liquid containing ungrafted PMMA. The cycle of centrifugation and redispersion in THF was repeated three times to obtain PMMA-grafted SWCNT presumed to be free of the unbound PMMA. The mixture was vacuum filtered through a 0.2 μm PTFE filter, washed with THF until the filtrate showed no cloudiness in excess methanol. The solid was washed with a small amount of anhydrous NMP and dispersed in 210 mL of NMP, bath sonicated for 15 min and stirred for 24 h. Two more grafting experiments were done on the other two 206 mL SWCNT-CTA/NMP dispersions using equal amounts of MMA and AIBN and under the same reaction conditions.

3.2.8 Cleavage of Grafted PMMA from SWCNT. The grafted PMMA was cleaved from the SWCNT surface by modifying a method described elsewhere.[41] A 100 mL round bottomed flask was charged with 20 mg of SWCNT-*g*-PMMA dispersed in 5 mL of $CDCl_3$, 20 mL of *o*-DCB, 7 mL of methanol, and 0.5 mL of concentrated sulfuric acid. The water condenser was attached to the flask and the mixture was stirred at 65 ^{o}C for 7 days. After cooling, the mixture was sonicated for 2 min with 15 mL of $CHCl_3$ and

vacuum filtered through a 0.2 μm PTFE filter to remove the PMMA free SWCNT. The tubes were washed twice with 10 mL of chloroform slowly with stirring to remove traces of PMMA. The filtrate was washed thrice with 10 mL of DI water to remove H_2SO_4, the organic phase which contained cleaved PMMA was isolated using a separatory funnel, and the organic solvent was removed under the vacuum. The residual solid left in the flask was dispersed in 15 mL of inhibitor free THF which was evaporated to approximately 2 mL for SEC analysis. After the SEC analysis the THF was evaporated to dryness, and 0.5 mL of $CDCl_3$ was added and analyzed by ^{1}H-NMR.

3.2.9 Preparation of PMMA Matrices by RAFT Polymerization. A mixture of a stock solution composed of MMA (24.1 g, 241 mmol), AIBN (0.01 g, 0.06 mmol), and NMP (11.9 mL) was added to a 100 mL Schlenk flask containing weighed amount of RAFT agent 4-cyano-4-(dodecylsulfanylthiocarbonylsulfanyl)pentanoic acid. The mixture was degassed by four full freeze-pump-thaw cycles, and the flask was sealed with Teflon and parafilm and heated in a oil bath at 90 ^{o}C for 6 h. After the reaction, the flask was quenched in liquid nitrogen and viscous poly(methyl methacrylate) was dissolved in 10 mL of dichloromethane and precipitated in 10-fold excess of methanol by slow dropwise additions. The solid PMMA-RAFT was vacuum dried at 100 ^{o}C for 48 h to take out the residual monomers. The conversion was determined gravimetrically.

3.2.10 Preparation of SWCNT-*g*-PMMA/PMMA Composites. For SWCNT-*g*-PMMA/PMMA composites, PMMA matrices of three different number average molecular weights were used with using the same RAFT agent anchored on the nanotube surface. The concentration of SWCNT in NMP (g L^{-1}) was measured by filtering 10 mL of SWCNT-*g*-PMMA/NMP dispersion on a pre-weighed PTFE filter. The solid on the

filter was washed with THF, and vacuum dried at 100 ^{o}C for 24 h. The weight of deposited solids and wt% of grafted PMMA on SWCNT obtained from the TGA analyses were used to calculate the amount of SWCNT dispersed in the NMP solvent. The SWCNT-*g*-PMMA/NMP dispersions were found to be in the range of 0.42-0.47 g L^{-1}. Dispersions of SWCNT-*g*-PMMA in NMP and matrix PMMA dissolved in THF (1.5 g in 20 mL) were mixed to yield the desired weight fraction of SWCNT-*g*-PS in the final composite. The mixture was stirred mechanically for 15 min, bath sonicated at room temperature for 15 min, and finally precipitated dropwise into a large excess of 10 wt% aqueous solution of $CaCl_2$ under vigorous mechanical stirring. The composite was filtered and washed with water until the filtrate showed no white precipitate in 0.0500 M $AgNO_3$(aq) solution. Then the solid was washed with small amount of methanol, and dried under vacuum at 130 ^{o}C for 24 h.

3.3 Results and Discussion.

RAFT polymerization is a versatile method for synthesizing polymers of well controlled architecture (block, star, graft) with narrow molecular weight distribution, and a variety of functionality and compositions. The large functional groups tolerance and versatility make RAFT popular for preparing a wide variety of polymers. RAFT mechanism involves the chain transfer of active species such as the radicals from decomposition of the initiator and propagating polymer radicals to the RAFT agent, forming an unreactive adduct radical, followed by fast fragmentation to a polymeric RAFT agent and a new radical which continues polymerization. The equilibrium is established by subsequent chain transfer-fragmentation steps between the propagating

radicals and polymeric RAFT agents and continues until all monomers are consumed, resulting in controlled growth of chains. The general RAFT mechanism is shown in Scheme 1.

Scheme 1. General Mechanism for RAFT Polymerization

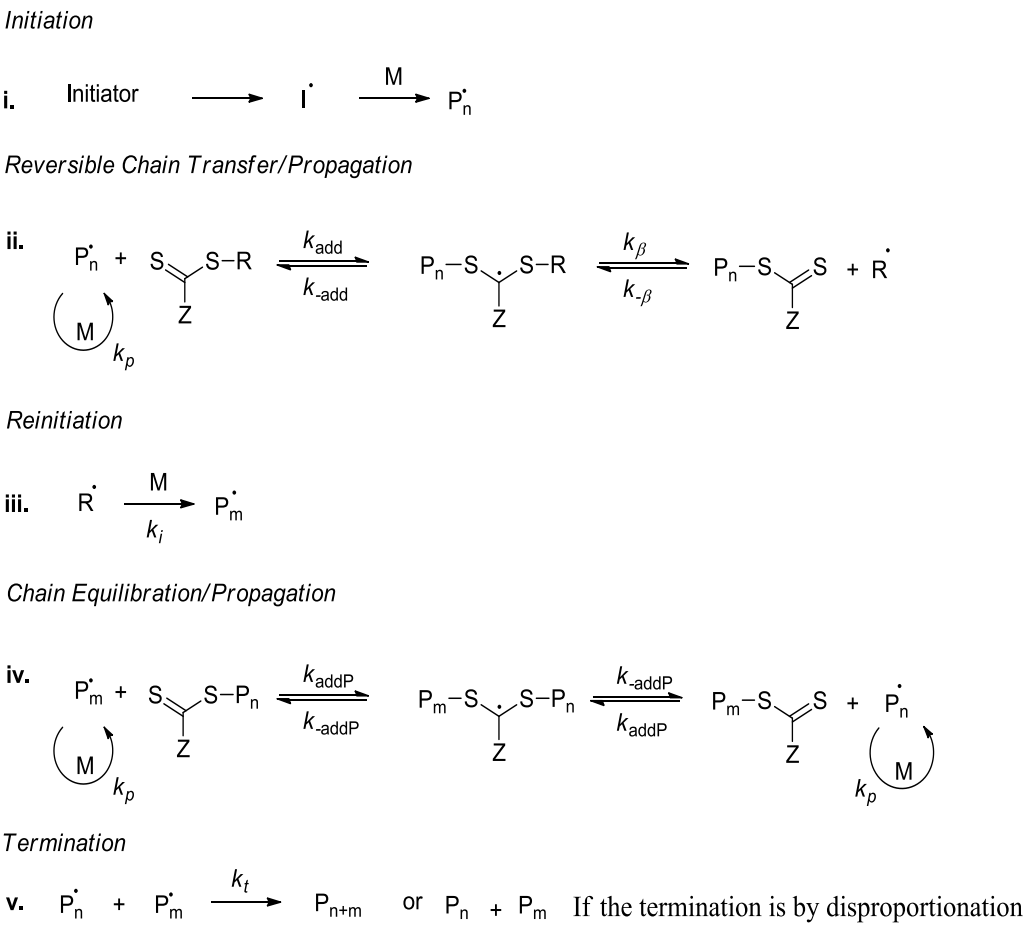

3.3.1 Immobilization of the RAFT Agent (CTA) on the SWCNT Surface. Trithiocarbonate based chain transfer agents are excellent for (meth)acrylate monomers. Therefore we have immobilized the trithiocarbonate based chain transfer agent (4-cyano-4-(dodecylsulfanylthiocarbonyl-sulfanyl)pentanoic acid) on the SWCNT surface as

shown in Scheme 2. During the nitric acid treatment, SWCNT are functionalized with carboxylic acid groups. The carboxylic acid groups bearing SWCNT were treated with thionyl chloride to get acid chloride groups on the nanotubes, and then tubes were reacted with ethylene glycol to give hydroxyl group-functionalized SWCNT denoted as SWCNT-OH. The RAFT agent immobilized SWCNT (SWCNT-CTA) were prepared by the reaction of SWCNT-OH with RAFT agent 4-cyano-4-(dodecylsulfanylthiocarbonylsulfanyl)pentanoic acid dispersed in dichloromethane in presence of DCC and DMAP as coupling agents. The SWCNT-CTA was characterized by ^{1}H-NMR, and the moles of RAFT agent grafted on the nanotubes were calculated from the amount of S-atoms by elemental analysis. ^{1}H-NMR spectra show peaks at 0.8-1.4 ppm (except CH_2 which is α to S atom) for dodecyl alkane chain. Elemental analysis showed an average of 0.85 wt% of S-atoms in the nanotube mixture on two independently prepared samples. Assuming 95 wt% C atoms in the SWCNT-RAFT, the moles of C = 0.079 moles/g and S atoms = 2.7×10^{-4} moles/g or $2.7 \times 10^{-4} / 3 = 8.9 \times 10^{-5}$ moles/g of RAFT agent attached to the SWCNT.

Scheme 2. RAFT Polymerization of Methyl Methacrylate Monomer from the Surface of SWCNT

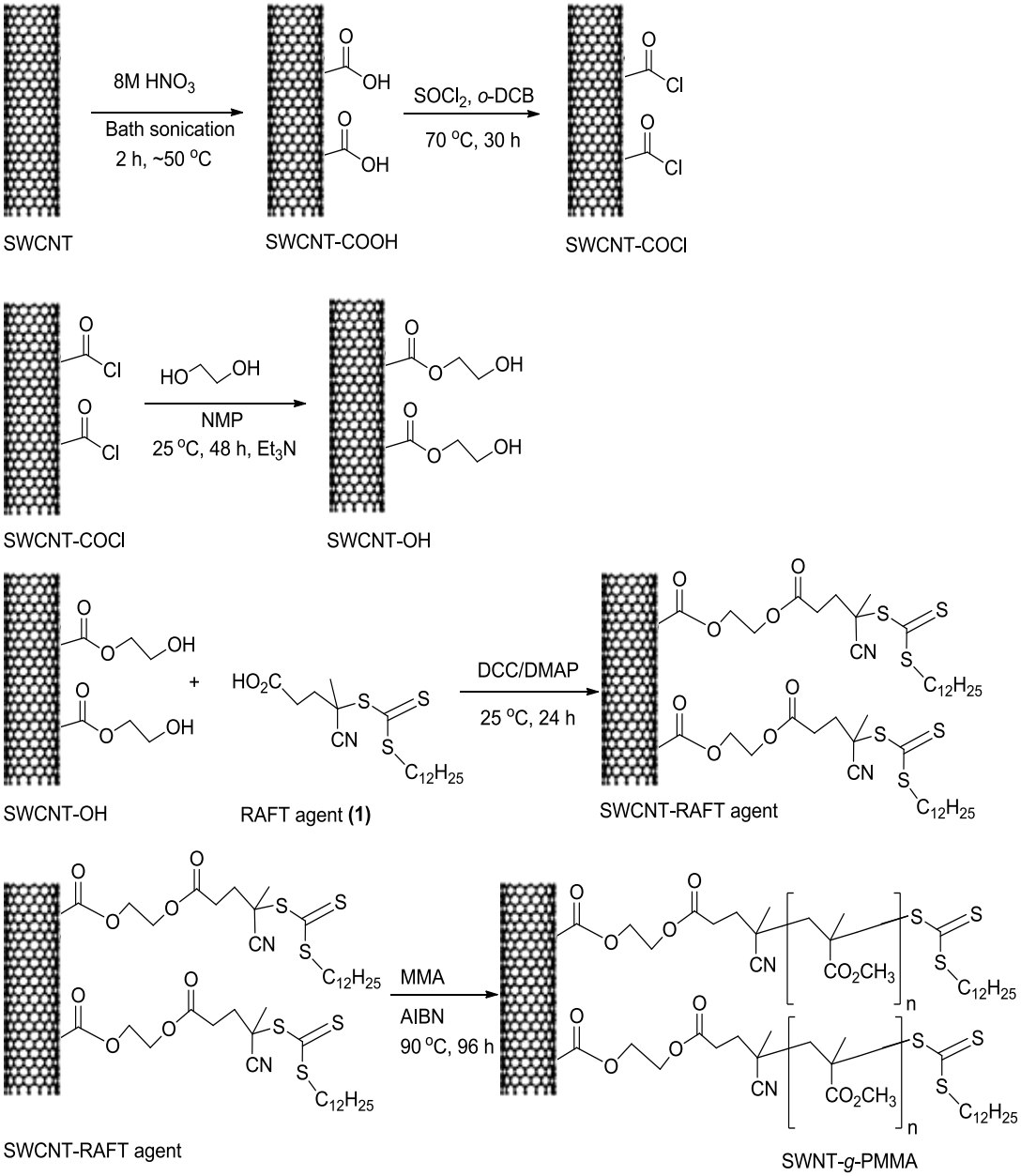

3.3.2 Preparation of SWCNT-*g*-PMMA via Surface RAFT Polymerization. The preparation of SWCNT-PMMA is shown in Scheme 1. Methyl methacrylate (MMA) was

polymerized using AIBN as an initiator and SWCNT-CTA as a chain transfer agent at 90 ^{o}C for 96 h. The product was washed thoroughly and dispersed in NMP for composite preparation. The PMMA grafted SWCNT were soluble in tetrahydrofuran, dimethylformamide, and ortho-dichlorobenzene at the concentration of 0.40 g/L. The grafted PMMA was cleaved from the SWCNT by acid-catalyzed transesterification in methanol to ensure that the methyl ester groups of the grafted PMMA remained intact during the reaction. The free PMMA was removed from the SWCNT-*g*-PMMA by extensive washing with THF. Then the molecular weight (MW) and the molecular weight distribution (MWD) of the cleaved PMMA were analyzed by SEC and reported in Table 1. The narrow MWD of grafted PMMA obtained from SEC analyses reveal that the RAFT polymerization of MMA from the SWCNT surface is controlled.

Table 1. Properties of Grafted and Ungrafted PMMA

grafted PMMA			ungrafted PMMA (filtrate)[a]		
M_n (g/mol)	M_w (g/mol)	M_w/M_n	M_n (g/mol)	M_w (g/mol)	M_w/M_n
22,600	31,400	1.39	19,100	23,500	1.23
26,000	34,100	1.31	18,200	22,600	1.24
35,700	40,700	1.14	18,700	24,700	1.32

[a]PMMA recovered from the filtrate of the grafting reaction mixture. The molecular weights are the average value of two SEC analyses.

Three different PMMA matrices of number average molecular weights smaller, equal, and greater than the molecular weights of the grafted PMMA were synthesized in NMP

solvent using the same chain transfer agent. The details of the reaction conditions, concentration of CTA used, and the T_g of the PMMA are given in Table 2.

Table 2. Molecular Weights and Polydispersities of PMMA Synthesized by RAFT Polymerization[a]

sample	$[RAFT]_0$ ($M\times10^2$)	M_n (g/mol)	M_w (g/mol)	M_w/M_n	yield (%)[b]	T_g (^oC)
PMMA14700	4.95	14,700	17,100	1.16	93	106
PMMA26600	2.48	26,600	31,900	1.20	98	113
PMMA97200	0.32	97,200	158,000	1.63	100	117
Blank	-	207000	840000	4.06	-	-

[a]MMA (6.55 M in N-methylpyrrolidinone) with azobisisobutyronitrile (0.0018 M) as initiator and RAFT agent (1) for 6 h at 90 ^{o}C. [b]Measured by gravimetric method.

The molecular weights of the ungrafted PMMA for all grafting experiments were 18,000 -19,000 g/mol, which is close to the grafted PMMA 22,000 - 26,000 g/mol (except 35,7000 g/mol), which suggests that the cleaved graft polymer and the free polymer were produced simultaneously. Similar results are reported in the literature for grafting poly(*n*-butyl methacrylate) onto the SWCNT by atom-transfer radical polymerization (ATRP)[41] and for grafting of PS onto silica by ATRP[42] and RAFT[43] polymerization.

3.3.3 Thermogravimetric Analysis. The weight percent of PMMA chains grafted to the SWCNT was measured by thermogravimetric analysis (TGA) as shown in Table 3. Figure 1 compares the TGA results for pristine SWCNT, nitric acid treated SWCNT, SWCNT-*g*-CTA, SWCNT-*g*-PMMA, and pure PMMA under the nitrogen atmosphere. The pristine SWCNT are stable up to 600 ^{o}C whereas PMMA grafted to the SWCNT

degraded at 300-450 ^{o}C. Initial weight loss started at 150-200 ^{o}C due to the loss of other functionalities such as COOH and unreacted CTA present on the nanotube surface. The weight losses from SWCNT-*g*-CTA and SWCNT-*g*-PMMA indicate 6 wt% percent of covalently grafted PMMA in all of the SWCNT-*g*-PMMA samples. The graft density reported in Table 3, is defined as the number of polymer chains per 1000 SWNT carbons. The weight loss of SWCNT-COOH is compared with pristine SWCNT assuming loss of CO_2; SWCNT-*g*-CTA weight loss is compared with SWCNT-COOH assuming the loss of $CH_2{=}CHO_2C(CH_2)C(CN)(CH_3)S_2CSC_{12}H_{25}$, and SWCNT-g-PMMA weight loss is compared with SWCNT-*g*-CTA. TGA data suggest that we have only functionalized a small fraction of RAFT agents into poly(methyl methacrylate).

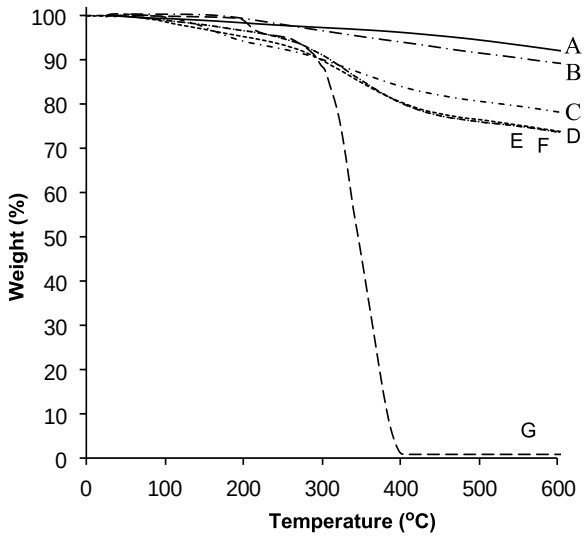

Figure 1. Thermogravimetric analysis under nitrogen at 10 ^{o}C min^{-1} of (A) Pristine CoMoCat, (B) nitric acid treated SWCNT, (C) SWCNT-RAFT agent, (D) SWCNT-*g*-PMMA22600, (E) SWCNT-*g*-PMMA26000, (F) SWCNT-*g*-PMMA35700, and (G) PMMA-RAFT (M_n = 44100 g/mol and PDI = 1.2).

Table 3. TGA Results From SWCNT-*g*-PMMA

M_n (g/mol)	weight loss (%)	graft density[a]
SWCNT-*g*-PMMA22600	5.9	0.03
SWCNT-*g*-PMMA26000	5.9	0.03
SWCNT-*g*-PMMA35700	5.9	0.02

[a]Functional groups or PMMA chains/1000 SWCNT carbon atoms.

3.3.3.1 Graft density (CTA/1000 SWCNT C atoms).

Moles of CTA (RAFT agent)

$$1\text{ g SWCNT-}g\text{-CTA} \times \frac{0.12\ g\text{ CTA}}{1\text{ g SWCNT-}g\text{-CTA}} \times \frac{1\text{ mol CTA}}{403.67\text{ g CTA}} = 3.0 \times 10^{-4}\text{ mol CTA}$$

Moles of SWCNT carbons

$$1\text{ g SWCNT-}g\text{-CTA} \times \frac{0.88\ g\text{ SWCNT}}{1\text{ g SWCNT-}g\text{-CTA}} \times \frac{1\text{ mol SWCNT C's}}{12.011\ g\text{ SWCNT C's}} = 7.3 \times 10^{-2}\text{ mol SWCNT C's}$$

$$\text{Graft Density} = \frac{3.0 \times 10^{-4}\text{ mol CTA}}{7.3 \times 10^{-2}\text{ mol SWCNT C's}} = 4.1 \times 10^{-4}\text{ mol CTA / mol of SWCNT C's}$$

$$= 4.1\text{ CTA / 1000 SWCNT C's}$$

3.3.3.2 Graft density (polymer chains/1000 SWCNT C atoms). A sample calculation of graft density for the sample SWCNT-*g*-PMMA22600 is shown below.

Moles of PMMA

$$1\text{ g SWCNT-}g\text{-PMMA} \times \frac{0.059\ g\text{ PMMA}}{1\text{ g SWCNT-}g\text{-PMMA}} \times \frac{1\text{ mol PMMA}}{22600\text{ g PMMA}} = 2.6 \times 10^{-6}\text{ mol PMMA}$$

Moles of SWCNT carbons

$$1\text{ g SWCNT-}g\text{-PMMA} \times \frac{0.94\ g\text{ SWCNT}}{1\text{ g SWCNT-}g\text{-PMMA}} \times \frac{1\text{ mol SWCNT C's}}{12.011\ g\text{ SWCNT C's}} = 7.8 \times 10^{-2}\text{ mol SWCNT C's}$$

$$\text{Graft Density} = \frac{2.6 \times 10^{-6}\text{ mol PMMA}}{7.8 \times 10^{-2}\text{ mol SWCNT C's}} = 0.33 \times 10^{-4}\text{ mol PMMA / mol of SWCNT C's}$$

$$= 0.033\text{ PMMA chains / 1000 SWCNT C's}$$

3.3.3.3 Graft density (PMMA chains/nm^2 of SWCNT). For a narrow SWCNT diameter = 1 nm

= 1 nm for C_{60}, which includes the van der Waals radii of C atoms. Across a tube the internuclear distance of C atoms is diameter = 0.7 nm.

For a 1.0 nm diameter armchair tube the carbon skeleton is shown below:

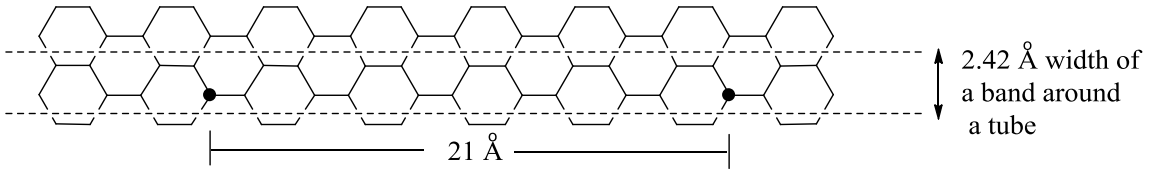

The circumference is $\pi \times$ (diameter) = 3.14 × (1 nm) = 3.14 nm. The circumference measured around C nuclei = $\pi \times$ (diameter) = 3.14 × (0.7 nm) = 2.20 nm = 22.0 Å.

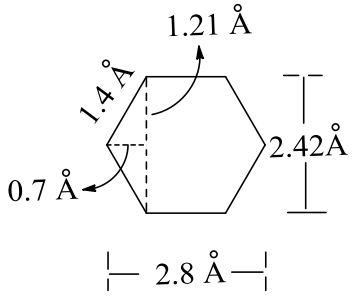

A six-membered ring has the C-C distances shown

1.4 Sin 30° = 0.70 Å
1.4 Cos 30° = 1.21 Å

On wrapping the carbon skeleton into a cylinder so that the marked C atoms superpose, the cylinder will have a circumference of 21 Å. There is no armchair tube with a circumference of 21 Å, but 21 Å is close and will have a distance of 21/π = 6.7 Å C to C across the cylinder and a van der Waals diameter of 9.5 Å = 0.95 nm. The shortest repeating distance along the length of the tube is 2.42 Å. There are 20 C atoms in the 2.42 Å × 21 Å around the tube.

Let us approximate the diameter of a tube = 1.00 nm with 20 C atoms per 2.42 Å = 0.242 nm length of the tube.

The surface area of this band is (0.242 nm) (2.1 nm) = 0.51 nm^2.

The surface area of a tube of 1000 C atoms is $\frac{1000}{20}$ x 0.51 nm^2 = 25.4 nm^2.

The cross-sectional area of a tube is $\pi \times (0.5\ nm)^2 = 0.785\ nm^2$.

The volume of the band is (0.785 nm^2) (0.242 nm) = 0.190 nm^3.

Let us consider bundles of tubes parallel and closely packed.

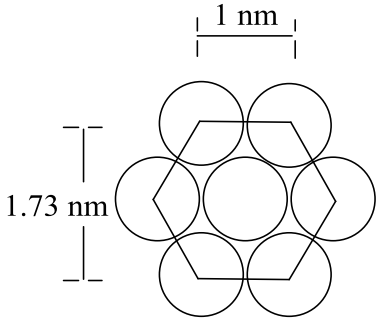

One tube cross-section area = 0.785 nm^2

The hexagon contains 3 tubes (1 whole tube + 6 x $\frac{1}{3}$ tube).

The area of the hexagon is (1.5 nm) (1.73 nm) = 2.60 nm^2.

Packing fraction of tubes in a cross-section = $\frac{3(0.785\ nm^2)}{2.60\ nm^2}$ = 0.91.

The area per tube in the cross-section of a cylindrical bundle is $\frac{0.785\ nm^2}{0.91}$ = 0.87 nm^2.

The volume per tube in a cross-section is $\frac{0.190\ nm^3}{0.91}$ = 0.21 nm^3.

Let us check if these numbers give a reasonable density for a bundle of tubes.

$$\text{Density} = \frac{\text{Mass}}{\text{Volume}}$$

$$= \frac{20 \text{ mol} \times 12 \text{ g mol}^{-1} \times \dfrac{1}{6 \times 10^{23}}}{0.21 \text{ nm}^3 \times \dfrac{1 \text{ cm}^3}{10^{21} \text{ nm}^3}}$$

$= 1.9 \text{ g cm}^{-3}$ which is a resonable value.

Less than perfect packing of cylinders would give lower density.

(a) Considering a 5-nm diameter bundle.

Circumference = π x (diameter) = 15.7 nm.

Cross-sectional area = π x $(\text{radius})^2 = 19.6 \text{ nm}^2$.

Surface area of a 0.242 nm bond around the bundle is (15.7 nm) (0.242 nm) = 3.80 nm^2.

Volume of a 0.242 nm length of the bundle is (19.6 nm^2) (0.242 nm) = 4.74 nm^3.

Assuming that the number of C atoms per unit surface area is the same for a 5-nm bundle as for a 1-nm single tube.

$$\text{Then number of C atoms on the surface of the bond} = 3.80 \text{ nm}^2 \times \frac{20 \text{ C}}{0.51 \text{ nm}^2} = 149 \text{ C atoms.}$$

$$\text{Density calculation in } \frac{\text{C atoms}}{\text{nm}^3}$$

$$= \frac{20 \text{ C atoms}}{0.21 \text{ nm}^3} = 95 \text{ C nm}^{-3}.$$

$$\text{In the 0.242 nm length of a 5-nm bundle there are } 4.74 \text{ nm}^3 \times \frac{95 \text{ C}}{\text{nm}^3} = 450 \text{ C atoms.}$$

$$\text{Fraction of C atoms on surface} = \frac{149}{450} = 0.33.$$

Surface area per 1000 C atoms = $\frac{3.80\ \text{nm}^2}{450\ \text{C}}$ x 1000 C = 8.4 nm^2.

(a) Considering a 10-nm diameter bundle.

Circumference = π x (diameter) = 31.4 nm.

Cross-sectional area = π x $(\text{radius})^2$ = 78.5 nm^2.

Surface area of a 0.242 nm bond around the bundle is (31.4 nm) (0.242 nm) = 7.60 nm^2.

Volume of a 0.242 nm length of the bundle is (78.5 nm^2) (0.242 nm) = 19.0 nm^3.

Assuming that the number of C atoms per unit surface area is the same for a 10-nm bundle as for a 1-nm single tube.

Then number of C atoms on the surface of the bond = 7.60 nm^2 x $\frac{20\ \text{C}}{0.51\ \text{nm}^2}$ = 298 C atoms.

In the 0.242 nm length of a 10-nm bundle there are 19.0 nm^3 x $\frac{95\ \text{C}}{\text{nm}^3}$ = 1805 C atoms.

Fraction of C atoms on surface = $\frac{298}{1805}$ = 0.17.

Surface area per 1000 C atoms = $\frac{7.60\ \text{nm}^2}{1805\ \text{C}}$ x 1000 C = 4.2 nm^2.

Surface density of PMMA chains for:

Individual tube: $\frac{0.033\ \text{chains}}{25.4\ \text{nm}^2}$ = 0.001 chains nm^{-2}

5-nm bundle: $\frac{0.033\ \text{chains}}{8.4\ \text{nm}^2}$ = 0.004 chains nm^{-2}

10-nm bundle: $\frac{0.033\ \text{chains}}{4.2\ \text{nm}^2}$ = 0.008 chains nm^{-2}

Table 4 summarizes graft densities of polymer chains on an individual SWCNT and SWCNT bundles.

Table 4. Grafting Densities of Polymer Chains on SWCNT and SWCNT Bundles

PMMA MW	chains/1000 C	1-nm tube chains/nm^2	5-nm bundle chains/nm^2	10-nm bundle chains/nm^2
22600	0.03	0.001	0.004	0.008
26000	0.03	0.001	0.004	0.008
35700	0.02	0.0008	0.002	0.005

3.3.4 UV-vis-NIR Spectroscopy. Figure 2 displays UV-visible-NIR absorption spectra of CoMoCat SWCNT before and after HNO_3 treatment, SWCNT-CTA, and SWCNT-*g*-PMMA of different molecular weights PMMA. The UV-vis-NIR spectra showed distinct first and second van Hove optical transitions for different nanotube species. CoMoCat CNT samples contain >50% of SWCNT with (7,6) chirality, as reported in the technical data sheet received with the CNT sample. On the pristine SWCNT Figure 2(A) and functionalized SWCNT Figures 2(B)-(F) materials prominent bands near 1174 and 667 nm are clearly observed which correspond to the S11 and S22 transitions of (7,6) nanotube[44,45] Other bands near 1189 and 740 nm correspond to (8,6) and (8,7) nanotubes. The peak intensities for the semiconducting tubes are much higher than corresponding metallic tubes. The appearance of distinct peaks in the spectra of SWCNT-*g*-PMMA similar to the spectrum of pristine SWCNT proves that the degree of functionalization by HNO_3 treatment and by PMMA grafting are relatively low because high degree of functionalization gives spectra with no distinct NIR peaks.[46] Therefore, our grafting method had little effect on the original structures of the carbon nanotubes.

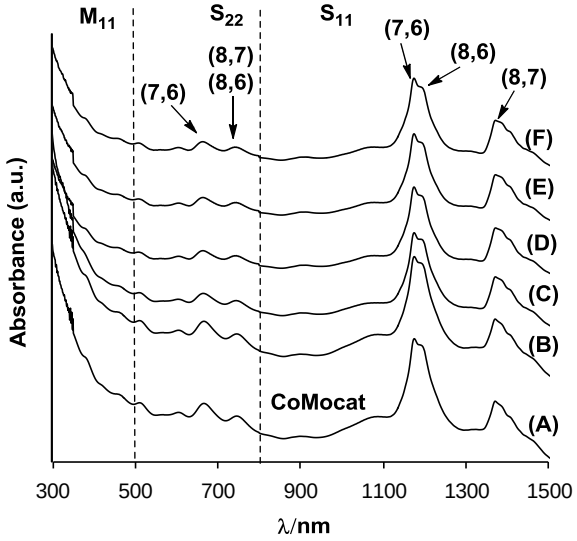

Figure 2. UV-vis-NIR of (A) pristine CoMoCat SWCNT, (B) nitric acid treated SWCNT, (C) SWCNT-RAFT agent, (D) SWCNT-*g*-PMMA22600, (E) SWCNT-*g*-PMMA26000, and (F) SWCNT-*g*-PMMA35700.

3.3.5 Raman Spectroscopy. The resonance Raman spectra in Figure 3 provide qualitative information about the degree of functionalization of SWCNT by carboxylic acid groups, RAFT agents, and PMMA compared to the starting nanotube. The Raman bands at 150-300 cm^{-1} for the spectrum 'a' are different from the rest of the spectra b-f which are either carboxylic acid functionalized, RAFT agent attached, or PMMA grafted SWCNT. The relative intensities of the disorder induced D-band at ~1350 cm^{-1} due to sp^3-hybridized carbon atoms and the tangential mode G-band at ~1580 cm^{-1} indicate differences in the degree of functionalization. The Raman spectra show little difference of D/G intensities between the starting SWCNT, nitric acid treated SWCNT, SWCNT-RAFT agent, and the SWCNT-*g*-PMMA materials. Overall, results of Raman analysis suggest that functionalization by PMMA had little effect on the structure of the sidewalls or on the inherent electronic properties of the SWCNT. Our initial mild nitric acid

treatment is known to produce a small number of carboxylic acid groups at sp^3 hybridized C atoms on the SWCNT[38] surface. Those acid groups were further used to graft PMMA on the nanotube surface, by reactions that in principle do not involve SWCNT carbon atoms. Thus, there is a likelihood of little or no effect on the morphology and inherent electronic properties of the conjugated sp^2 hybridized carbon nanotubes. For comparison highly functionalized nanotubes have broad D-bands in Raman spectra.[47]

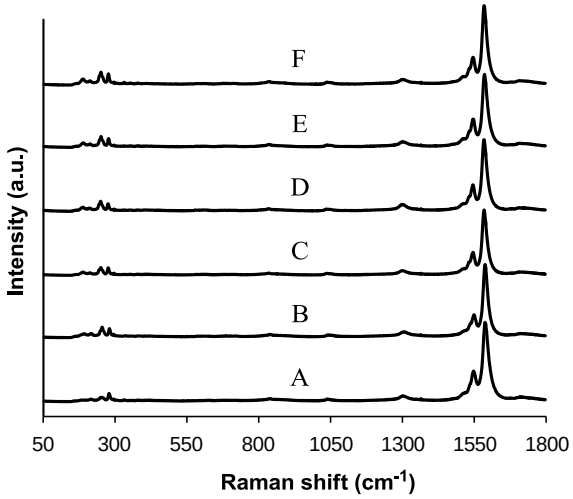

Figure 3. Raman spectra of (A) Pristine CoMoCat, (B) nitric acid treated SWCNT, (C) SWCNT-CTA, (D) SWCNT-*g*-PMMA22600, (E) SWCNT-*g*-PMMA26000, and (F) SWCNT-*g*-PMMA35700.

3.3.6 ^{1}H-NMR Analysis.

Figures 4 and 5 show ^{1}H-NMR spectra of RAFT agent, PMMA synthesized by RAFT polymerization, SWNT-RAFT agent, SWCNT-*g*-PMMA35700, and cleaved PMMA of all lengths. In the ^{1}H-NMR spectra of SWCNT-RAFT agent, the characteristic peaks at δ = ~0.8 ppm ascribed to methyl protons and δ = 0.8-1.8 ppm are for methylene protons of

long alkyl chain ($C_{12}H_{25}$) except methylene proton present at the α to the S-atom of trithiocarbonate. The methylene protons present adjacent to the trithiosulphur group appear at δ ~ 3.55 ppm in 4(a). In 4(b) peak at δ ~ 3.70 ppm is due to residual ethylene glycol. In the ^{1}H-NMR spectrum (5(a)) of PMMA synthesized by RAFT polymerization, peaks from 0.8 to ~2.0 ppm are due to alkyl groups of PMMA. A singlet at δ ~ 3.60 ppm is due to methoxy (OCH_3) group of PMMA. For ^{1}H-NMR spectra (5(b)) of SWCNT-*g*-PMMA for all chain lengths, protons from the alkyl chain of the RAFT agent and PMMA CH_2 groups appears at δ = 0.5-2 ppm and there is a distinct singlet peak for methoxy (OCH_3) group from the grafted PMMA at δ ≈ 3.6 ppm. ^{1}H-NMR spectra of cleaved PMMA are similar to the SWCNT-*g*-PMMA ^{1}H-NMR spectra. ^{1}H-NMR spectra of RAFT agent and PMMA chains attached to SWCNT suggest that only a small fraction of RAFT agents were used for RAFT polymerization.

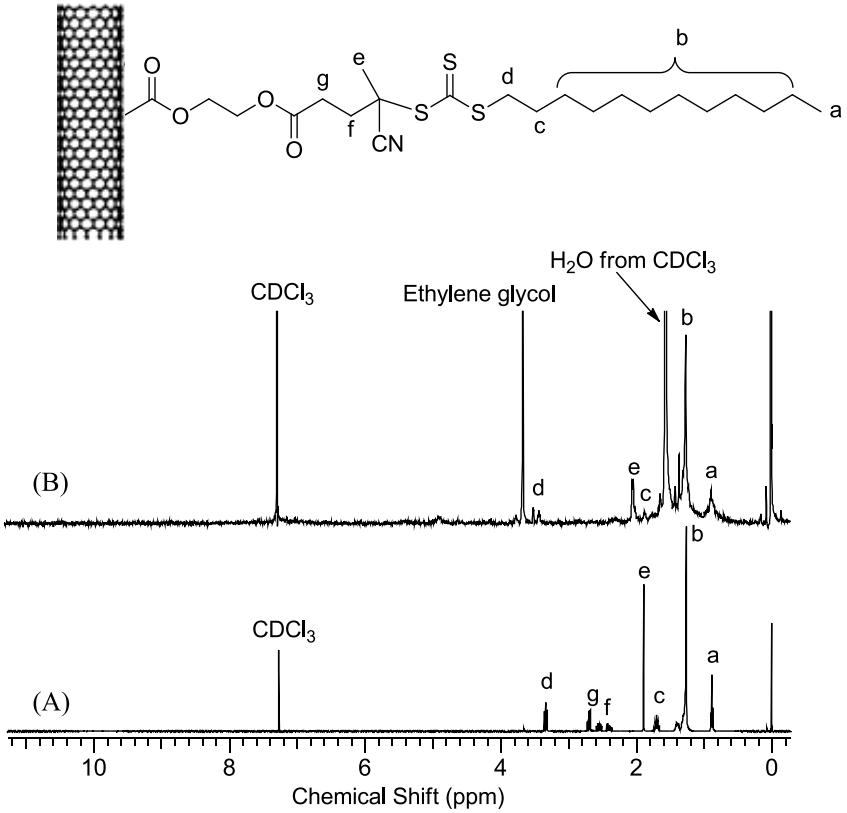

Figure 4. ^{1}H-NMR of (A) RAFT agent and (B) RAFT agent immobilized to SWCNT.

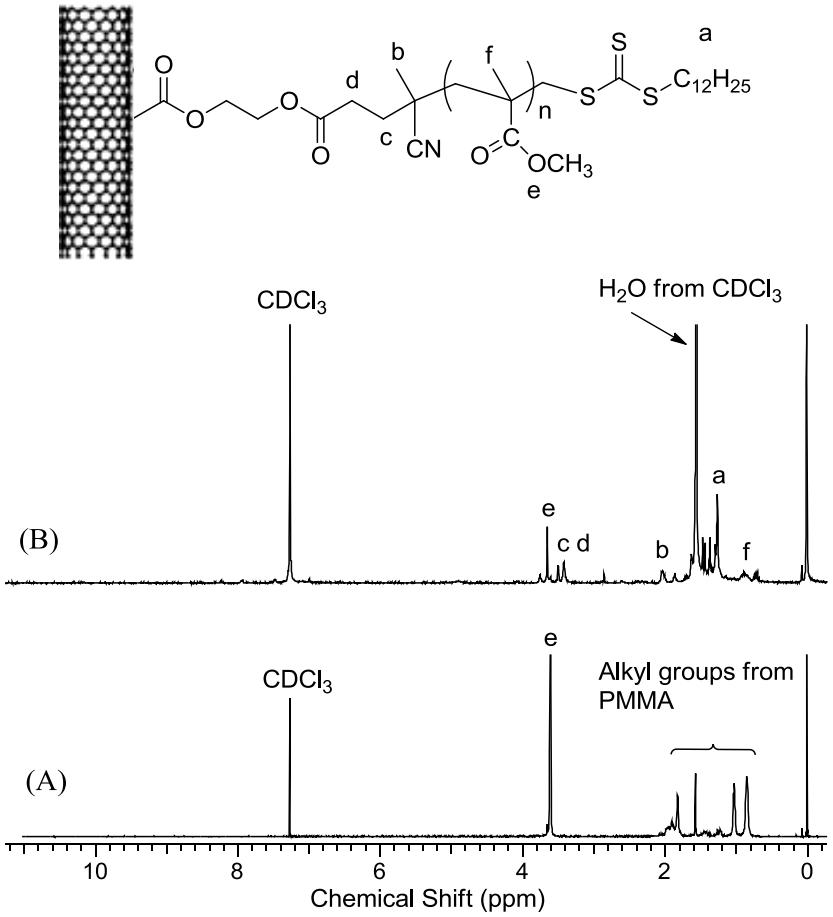

Figure 5. ^{1}H-NMR of PMMA grafted on SWCNT. (A) PMMA (M_n = 41300 g/mol and PDI = 1.14) and (B) SWCNT-*g*-PMMA35700.

3.3.7 STEM Analysis. STEM images of pristine SWCNT and nitric acid treated SWCNT are shown in Figure 6. The lower resolution images in Figures 6A and 6C show long bundles of a wide range of diameters over holes of the grids. The diameters of individual bundles also are not uniform, which means that different numbers of tubes comprise the diameters at different points over the length of a bundle. The higher resolution images of Figures 6B and 6D show a few black spots <5 nm in diameter, which we attribute to catalyst residues that were not removed by the nitric acid treatment. Figure 9D shows bundles of varied sizes and the individual parallel SWCNT in the bundles. Figure 7

shows SWCNT intertwined bundles of SWCNT-*g*-PMMA26000 and SWCNT-*g*-35700 samples of similar diameters seen in pristine SWCNT and nitric acid treated SWCNT samples. The black spots on images B, D, F, and G are likely due to residual catalyst particles. Nitric acid washing at elevated temperatures cannot always remove metal impurities completely because these metal nanoparticles are sheathed by several graphene sheets.[48] We did not see the amorphous grafted PMMA onto the nanotube surface, which could be due to the small amount (6 weight %) of PMMA grafted to the SWCNT.

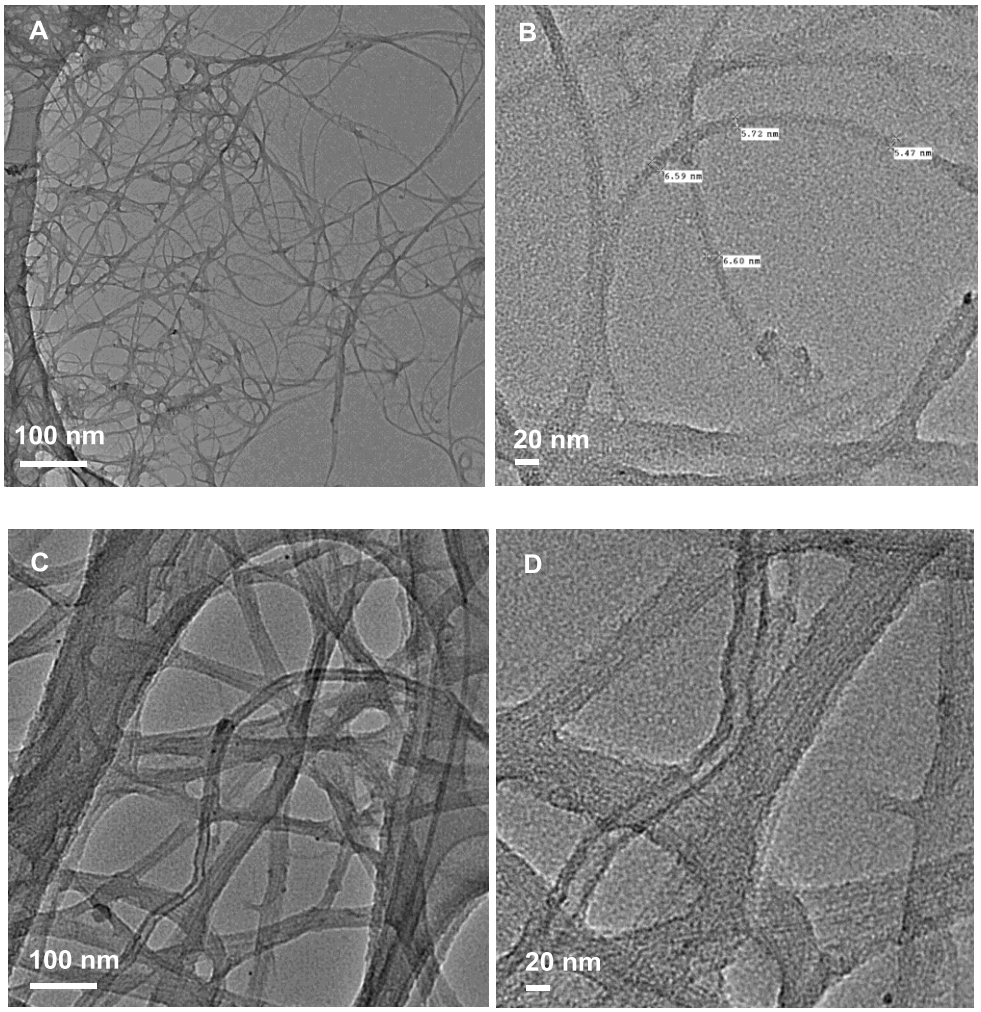

Figure 6. STEM images of (A, B) SWCNT (pristine) and (C, D) nitric acid treated SWCNT. EM magnifications of A, B, C, and D are 12000, 100000, 50000, and 150000 respectively. In image B the diameters at four different marked points are 5.47, 5.72, 6.59, and 6.60 nm, which correspond to six and seven SWCNT diameters.

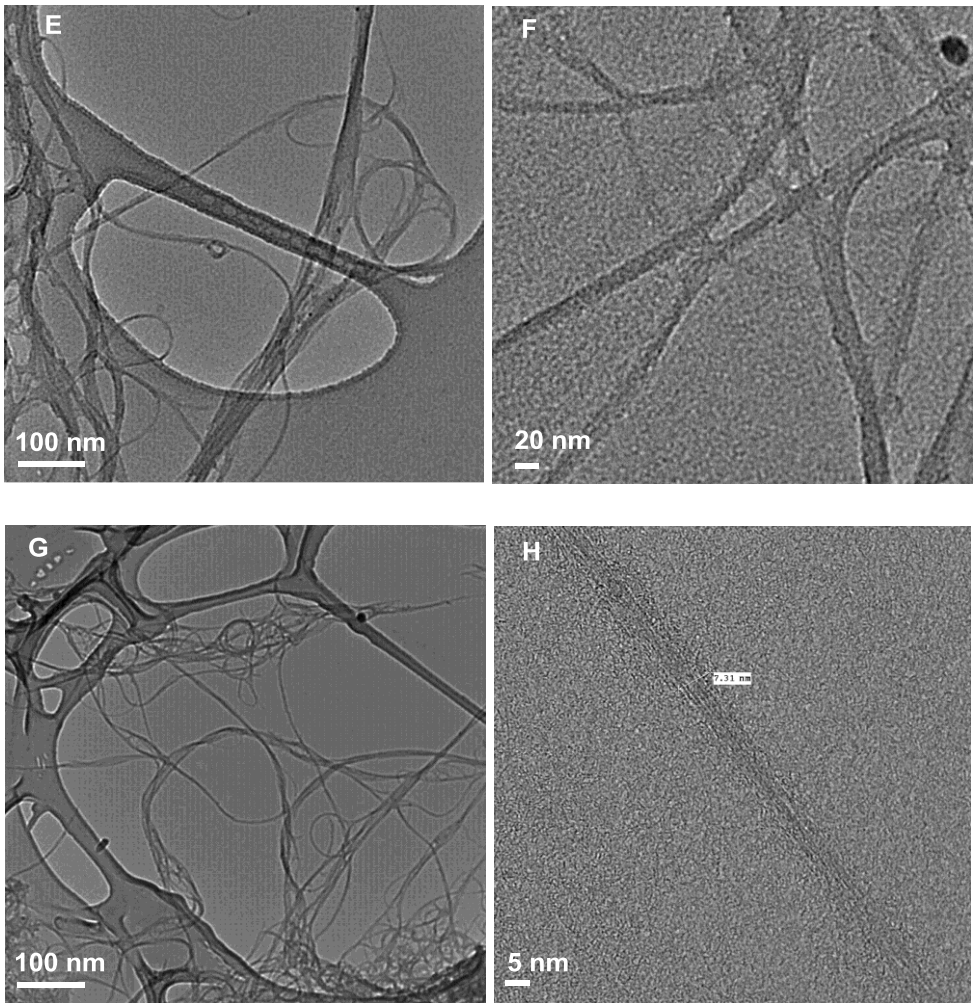

Figure 7. STEM images of (E, F) SWCNT-*g*-PMMA26000 and (G, H) SWCNT-*g*-PMMA35700. In H the diameter at the marked point of a bundle is 7.31 nm, which corresponds to 7 SWCNT diameters. EM magnifications of A, B, C, and D are 40000, 120000, 12000, and 250000 respectively.

3.4 SWNT-*graft*- PMMA/PMMA Nanocomposites.

3.4.1 Electrical Conductivity. Figure 8 shows the electrical conductivity of PMMA incorporated with varied weight fractions of SWCNT-*g*-PMMA measured by a two-probe technique. The conductivity was measured at 2 different places by applying two different

voltages 100 and 30 V. The average value of electrical conductivity in S/cm is reported. When $M_{graft} > M_{matrix}$, the conductivity of nanocomposites increased from 10^{-16} to 10^{-10} S/cm over 0.25 to 1.0 wt% SWCNT loadings and formed a plateau with further nanotube additions. For $M_{graft} = M_{matrix}$, the conductivity of nanocomposites reached the value 10^{-10} S/cm at 1.0 wt% and formed a plateau at higher SWCNT loadings. In case of $M_{graft} < M_{matrix}$, there was no sharp percolation threshold of electrical conductivity of nanocomposites. The conductivity increased only after 0.5 wt% SWCNT loading to 10^{-11} S/cm at 2.0 wt% SWCNT. In this case a plateau is not formed up to 2.0 wt% SWCNT loadings as observed in other two cases. The composites have percolation threshold of electrical conductivity at ~0.5 wt% SWCNT. The conductivity of composites with SWCNT-*g*-PMMA (CoMoCat) is similar to the data reported by Tchoul[49] for oxidized CoMoCat/PS composites in a polydisperse M_n = 70,000 g/mol matrix. But the percolation threshold for SWCNT-*g*-PMMA35700/PMMA14700 composites in our case is lower than the SWCNT/PS composites (CoMoCat) reported by Tchoul.[49] The grafted PMMA enhanced the dispersion of SWCNT in the PMMA matrix. The conductivity of CoMoCat composites, both here and reported by Tchoul,[49] was lower than the HiPco/PS composites because metallic tubes carry most of the current in SWCNT networks, and the resistance is dominated by semiconducting SWCNT. CoMoCat SWCNT contains 9.0% metallic tubes whereas HiPco tubes contain 20%.[49] Hence composites made from CoMoCat tubes would be expected to have lower conductivity in the plateau region than composites made from HiPco tubes.

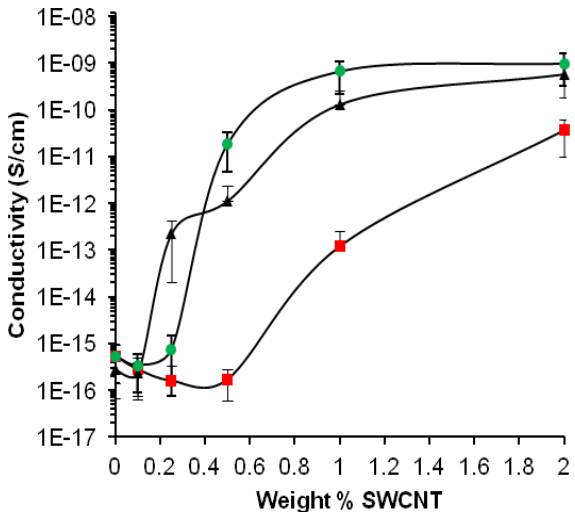

Figure 8. Electrical conductivity of SWCNT-g-PMMA/PMMA nanocomposites. The symbols used are: (■) Matrix PMMA97200 with SWCNT-*g*-PMMA22600, (▲) Matrix PMMA26600 with SWCNT-*g*-PMMA26000, and (●) Matrix PMMA14700 with SWCNT-*g*-PMMA35700. The error bars represent standard deviation.

3.4.2 Thermal Analysis. Table 5 shows the characteristics of composites and matrix polymers studied. Even at low filler loadings well dispersed nanoparticles create a large particle-polymer interface which can affect the behavior of matrix polymer over several radii of gyration, resulting in a dramatic change in thermal and mechanical properties of nanocomposites.[50]

Table 5. SWCNT-*g*-PMMA/PMMA Composites

sample identification number (SIN)	weight % of SWCNT	M_n (g/mol) of the grafted PMMA chains	M_n (g/mol) of the matrix PMMA chains
AC-67	0.10	22,600	97,200
AC-68	0.25	22,600	97,200
AC-69	0.50	22,600	97,200
AC-70	1.0	22,600	97,200
AC-71	2.0	22,600	97,200
AC-72	0.10	26,000	26,600
AC-73	0.25	26,000	26,600
AC-74	0.50	26,000	26,600
AC-75	1.0	26,000	26,600
AC-76	2.0	26,000	26,600
AC-77	0.10	35,700	14,700
AC-78	0.25	35,700	14,700
AC-79	0.50	35,700	14,700
AC-80	1.0	35,700	14,700
AC-81	2.0	35,700	14,700

Literature shows that the graft density and the relative lengths of graft chains (M_{graft}) on nanoparticles and matrix chains (M_{matrix}) play a crucial role in dictating the effective interparticle interactions in the polymer matrix.[25] To understand the effect of variation of those interparticle interactions with changes in the length of PMMA matrices, we studied the shift in T_g for SWCNT-*g*-PMMA/PMMA nanocomposites as a function of nanotube loadings. The PMMA matrices used for composite preparation had number average molecular weights of 14700, 26600, and 97200 g/mol and corresponding glass transition

temperatures of 106, 113, and 118 ^{o}C respectively. These data are in agreement with inverse relationship between the T_g and the molecular weight for PMMA. The molecular weight dependence of T_g is usually described reasonably well by the empirical Fox-Flory equation $T_g(M_n) = T_g(\infty) - K/M_n$, where K is a material dependent parameter and $T_g(\infty)$ is the asymptotic value of T_g at infinitely high MW.[51] The values of K and $T_g(\infty)$ were considered to be 1.06 x 10^5 and 123 ^{o}C from the literature.[52] Table 6 compares the T_g calculated by using Fox-Flory equation and measured by DSC.

Table 6. Comparison of T_g of PMMA Matrices Calculated by Fox-Flory Equation and Measured by DSC

sample	T_g (^{o}C) Fox-Flory equation	T_g (^{o}C) measured by DSC
PMMA14700	116	106
PMMA26600	119	113
PMMA97200	122	118

Figures 9 and 10 show the changes in glass transition temperature (T_g) and change in heat capacity (ΔC_p) at T_g for composites prepared by mixing SWCNT grafted with PMMA of different graft lengths and PMMA matrices with chain lengths smaller, equal to, and greater than the grafts for different weight % of SWCNT. For nanocomposites containing M_{graft} = 35700 g/mol and M_{matrix} = 14700 g/mol, T_g increases from 106 to 113 ^{o}C due to wetting between the particles and the PMMA matrices. In case of nanocomposites containing M_{matrix} = 26000 g/mol and M_{graft} = 26600, there is a moderate increase in the T_g from 113 to 115 ^{o}C due to the partial wetting. The increase in T_g for low MW PMMA matrix is comparatively steeper than the composites made with matrix

MW equals to the grafts PMMA, this suggests that low MW PMMA matrix strongly wets the nanotubes, intertwined with the brush ("wet" brush behavior), creating a strong interfacial interactions. When $M_{matrix} = M_{graft} \approx 26600$ g/mol or equal, we find that the increase in T_g was at the most 2 ^oC up to 2 wt% with SWCNT loadings. For nanocomposites made with $M_{graft} = 22600$ g/mol and $M_{matrix} = 97200$ nanocomposites, we saw no change in T_g compared to the unfilled PMMA matrix with the increase in wt% of SWCNT in composites. The reason for such behavior could be due the neutral particle surface.[26] Another important observation is that the behavior of SWCNT-*g*-PMMA/PMMA composites is analogous to polymer thin films containing two different lengths of chemically same polymers. For example, the stability of polystyrene (degree of polymerization *P*) films on silicon wafer was increased by blending with poly(styrene-*block*-methyl methacrylate) having a short and adsorbing MMA block and long, dangling polystyrene block (degree of polymerization *N*). The instability of polymer films were characterized by the formation of holes in the coatings. This process is called "*dewetting*". The hole growth velocity on the films were increased by 5 and 17 times for $N \sim P$ and $N > 4P$ at the 0.05 volume fraction of poly(styrene-*block*-methyl methacrylate).[16]

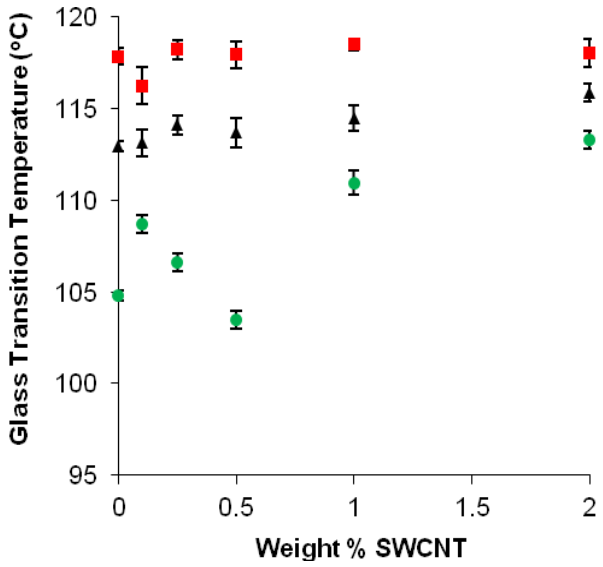

Figure 9. T_g for poly(methyl methacrylate) filled with SWCNT-*g*-PMMA from 0-2.0 wt% SWCNT. The symbols used are (■) Matrix PMMA97200 with SWCNT-*g*-PMMA22600, (▲) Matrix PMMA26600 with SWCNT-*g*-PMMA26000, and (●) Matrix PMMA14700 with SWCNT-*g*-PMMA35700. The error bars represent the standard deviations.

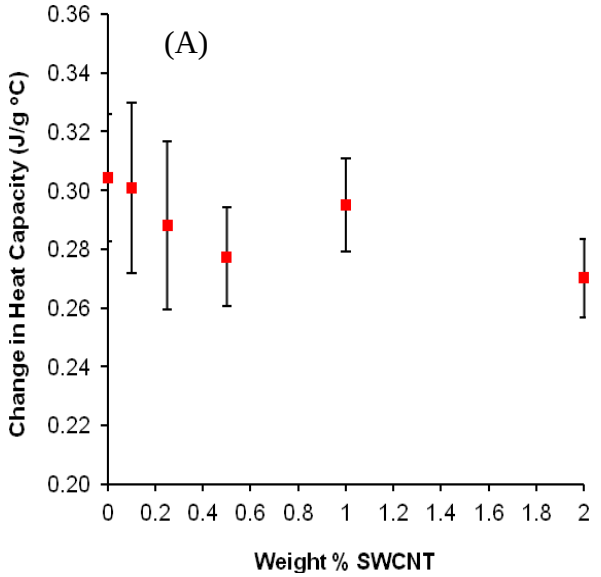
(A)
Change in Heat Capacity (J/g °C)
0.36
0.34
0.32
0.30
0.28
0.26
0.24
0.22
0.20
0
0.2
0.4
0.6
0.8
1
1.2
1.4
1.6
1.8
2
Weight % SWCNT

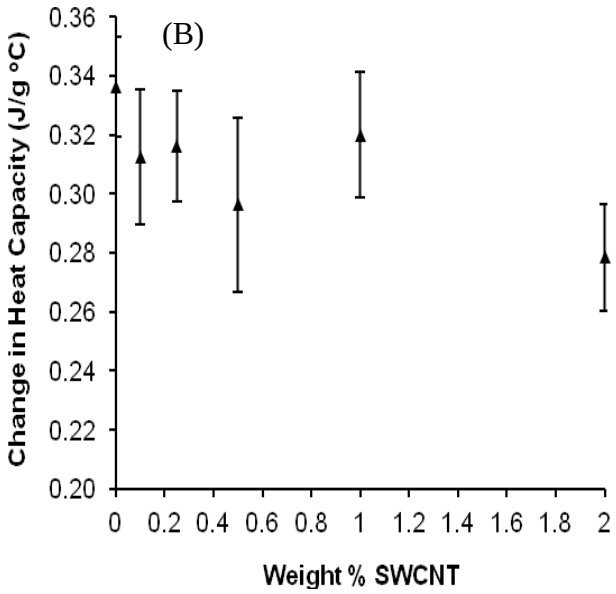
(B)
Change in Heat Capacity (J/g °C)
0.36
0.34
0.32
0.30
0.28
0.26
0.24
0.22
0.20
0
0.2
0.4
0.6
0.8
1
1.2
1.4
1.6
1.8
2
Weight % SWCNT

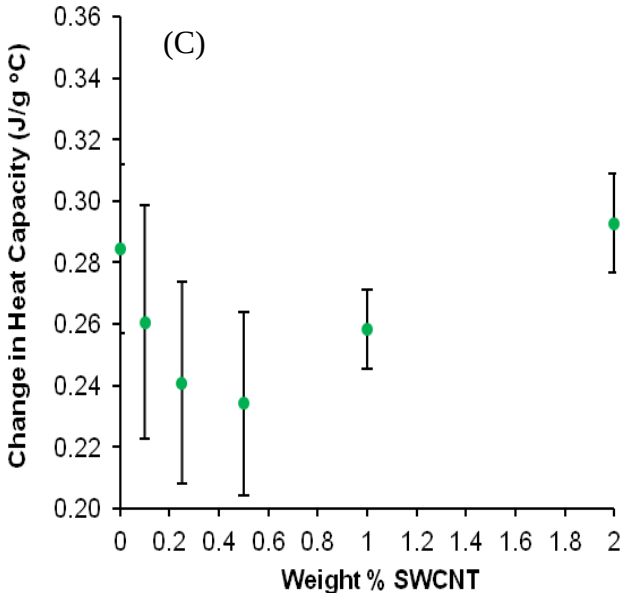

Figure 10. Change in heat capacity (ΔC_p) at T_g of poly(methyl methacrylate) filled with SWCNT-*g*-PMMA from 0-2.0 wt% SWCNT. The symbols used are (A) (■) Matrix PMMA97200 with SWCNT-*g*-PMMA22600, (B) (▲) Matrix PMMA26600 with SWCNT-*g*-PMMA26000, and (C) (●) Matrix PMMA14700 with SWCNT-*g*-PMMA35700. The error bars represent the standard deviations.

It is well documented that in polymer matrices filled with nanoparticles, a strong interfacial interaction between the particle and matrix can increase the T_g and a non-wetting interaction can decrease the T_g.[26] This suggests that the low MW matrix, which strongly wets the particles by forming a interlock like arrangements with the graft chains of the particles resulting in the rise in T_g. Thus, increase in T_g for nanocomposites accounts for a strong interfacial interaction between the matrix PMMA and the SWCNT. In case of favorable particle-polymer interactions, the brush chains stretch out of several times their radius of gyration. In this study, when $M_{graft} \geq M_{matrix}$, the grafted PMMA

chains extend further and occupy a greater volume fraction of the nanocomposites. Both these effects led to restricted chain mobility of matrix PMMA resulting in the increase in T_g. When the matrix PMMA are small, the free chains penetrate grafted chains to maximize translational entropy termed as wetting regime. On increasing the length of matrix PMMA, the transitional entropy decreases resulting in the increase in PMMA brushes swelling which expel the matrix free chains resulting in "*dewetting*" regime. Similar results were also reported by other groups. Schadler *et al.*[26] studied the "*wetting*" and "*dewetting*" of mixtures of PS chains grafted on silica particles of radius 7 ± 2 nm, with grafting density σ = 0.27 chains/nm^2 in homopolymer matrices of PS of different chain lengths. The radius of silica particle was nearly equal to the radius of gyration of the grafted PS, ≈ 8 nm. To evaluate the effect of the variation in interfacial properties on matrix molecular weight, they studied the T_g of SiO_2-*g*-PS/PS nanocomposites. The T_g of nanocomposites increased when the MW of the matrix was lower than the grafts, which suggests that the lower molecular weight PS matrix wets the particle surface, and the crossover to autophobic dewetting occurred when P/N ~ 0.7. A similar "*wetting/dewetting*" dependency on the lengths of graft to matrix molecular weights has been recently reported by Composto *et al.*[53] for PS grafted gold (Au) nanorods of radius = 6 nm and length = 42 nm mixed with PS matrices of different chain lengths. They studied the dispersions and aggregations of Au particles in the PS melts by using UV-visible plasmon absorption spectroscopy and transmission electron microscopy (TEM). The graft densities in this case were between 0.15 and 0.53 chains/nm^2, slightly higher than the value reported by Schadler's group for SiO_2-*g*-PS. These PS-Au(*N*):PS(*P*) films have a uniform dispersion of nanorods for the conditions $P \leq N$. For $P \geq N$, the inter-rod

interaction energy is weak, and nanorods clustered into small aggregates. For $P >> N$, the nanorods were found almost exclusively in aggregates. In this case the radius of the particle (R_p) was less than the radius of gyration (R_g) of matrix PS. The foregoing examples reveal that the "*wetting/dewetting*" transition strongly influenced by the phase separation/miscibility of the system. Table 7 summaries few experimental results of miscibility of nanoparticles grafted with polymers with varied chain lengths and graft density in chemically similar matrix polymers.

Table 7. Wetting/Dewetting Between Polymer Brushes Grafted to Nanoparticles and Matrix Polymers

particle/ diameter	polymer brushes (M_n)	matix M_n (g/mol) PDI	graft density chains/nm^2	results	Ref.
L. Schadler *et.al.* 3D systems					
Silica dia. 14 ± 4 nm 15 wt% silica loading	PMMA 55000 g/mol PDI 1.38	PMMA 188600 g/mol PDI = 1.04	0.12	Dewetting	54
	PMMA 55000 g/mol PDI 1.38	PMMA 18000 g/mol PDI = 1.15	0.12	Wetting	
	PMMA 60000 g/mol PDI 1.20	PMMA 204700 g/mol PDI = 1.02	0.05	Dewetting	
	PMMA 60000 g/mol PDI 1.20	PMMA 10200 g/mol PDI = 1.03	0.05	Wetting	

Silica dia. 14 ± 4 nm 0.5, 1.0, 5.0, and 15 wt % of silica	PS 105000 g/mol PDI = 1.15	PS 44000 g/mol PDI = 1.1 PS 150000 g/mol PDI = 1.1	0.05	Wetting Dewetting	55
R. J. Composto *et. al.* 2D systems					
Silica dia. 12.8 nm	PMMA 1800 g/mol 21000 g/mol 160000 g/mol	PMMA:SAN (50:50) wt% M_w = 106000 and 1.20 R_g = 11.6 nm and 118000 and 2.24 R_g = 9.5 nm	0.70	Only brushes with M_n = 160000 are miscible with the matrix PMMA:SA	56
Au rods avg. dia. 14 nm and an avg. length of l = 47 Au NR vol. fraction 0.011 0.048 0.095 0.161	Poly(ethylene glycol) (PEG) M_w = 5000 g/mol	PMMA , M_w 38500, 82400, 32000 g/mol R_g = 5.4-15.9 nm Poly(ethylene oxide) (PEO) M_w 102000 g/mol All polymers have PDI ≈ 1.05-1.1, So, $M_n \approx M_w$	-	Au-PEG mixed well with PMMA matrix regardless of higher MW of melt matrices and aggregated when the matrix melt was changed to PEO (CH_2CH_2O)	57

D. Green *et. al.* 1D systems					
Silica dia. 200 ± 5 nm vol. fractions 0.6 - 1.0	*N* = 4,18, and 36 kg/mol R_g = 1.58, 3.35, and 4.74 nm	*P* = 2.05 and 23.2 kg/mol R_g = 1.1 ± 0.2 nm to 3.8 ± 1.0	0.17	When N > P particles were stable When N < P aggregated	58
Silica radius 592 nm 100 nm 16 nm	PDMS-OH 25.20 kg/mol PDI = 1.64 R_g = 3.95 nm	PDMS-CH_3 2.05 kg/mol PDI = 1.01 R_g = 1.13 nm 8.46 kg/mol PDI = 1.49 R_g = 2.30 nm 13.30 kg/mol PDI = 1.89 R_g = 2.90 nm	0.15-0.24		59

In our sample, the dispersion of SWCNT-*g*-PMMA of all grafted lengths in PMMA matrices of different molecular weights are good because we saw increase or no change in the T_g, but no decrease in T_g. These results are consistent with earlier results for polymer brushes grafted on planar and spherical surfaces mixed in the melt of the same polymer. For all of our SWCNT-g-PMMA/PMMA nanocomposites, ΔC_p at T_g does not decrease systematically but remains at 0.33-0.27 J g^{-1} $^oC^{-1}$ over the composition range of 0.5-2.0 wt % of SWCNT. However, ΔC_p for matrix PMMA14700 with SWCNT-*g*-PMMA35700 is lower than the other two matrices 26000 and 97200 g/mol, which indicates that the lowest MW matrix PMMA, 14700 mol/g, wets the SWCNT surface.

The decrease in ΔC_p indicates a reduction in the amount of material participating in the glass transition. Our results on SWCNT qualitatively agree with the results of polystyrene (PS) grafted gold nanorods[53] and silica[26,58,59] nanoparticles mixed with chemically similar homopolymer melts of different chain lengths.

3.4.3 Dynamic Mechanical Analysis. To study the reinforcing effects of SWCNT grafted with PMMA on PMMA matrix, visco-elastic properties of SWCNT-*g*-PMMA/PMMA nanocomposites were measured by the dynamic mechanical analysis (DMA). Figures 11 and 12 show the temperature dependence of storage modulus (E') and tan δ for unfilled and SWCNT-*g*-PMMA filled PMMA nanocomposites. Note that we have only reported DMA results for the samples where $M_{graft} \leq M_{matrix}$. For $M_{graft} > M_{matrix}$, the SWCNT/PMMA nanocomposites were so brittle that we could not recover the nanocomposite films intact from the mold. The unfilled PMMA14700 itself was highly brittle to handle during the compression molding. Further addition of SWCNT made composites harder and more brittle. We conjecture that for cases where $M_{graft} > M_{matrix}$, the PMMA functionalized SWCNT would have a stronger interfacial bonding between the grafted PMMA chains and PMMA matrix via their polymer chain entanglements. This strong interfacial interaction would further hamper the dynamics of polymer chains, hindering segmental motion, and thus lead to a higher storage modulus. Increase in modulus corresponds to increase in stiffness of nanocomposites.[60]

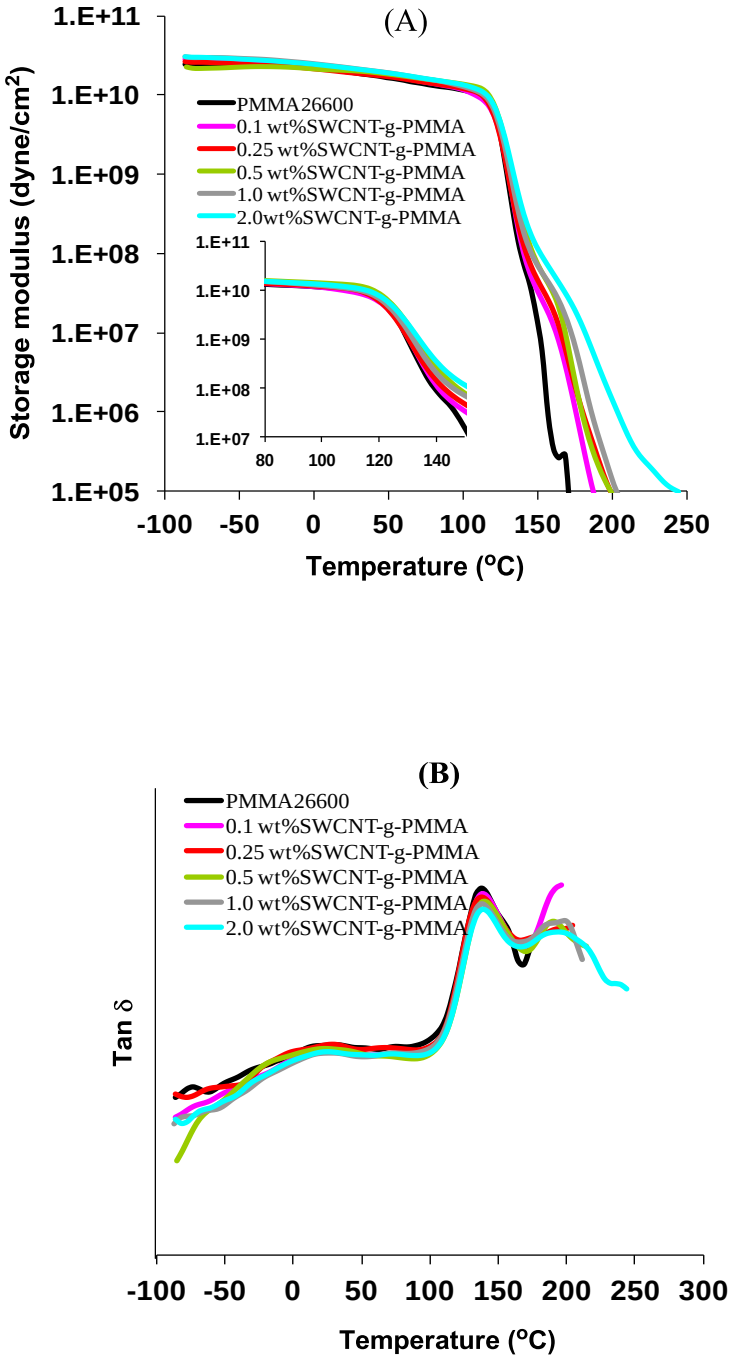

Figure 11. DMA of SWCNT-*g*-PMMA26600/PMMA26000 nanocomposites with temperature sweep. (A) storage modulus and (B) tan δ.

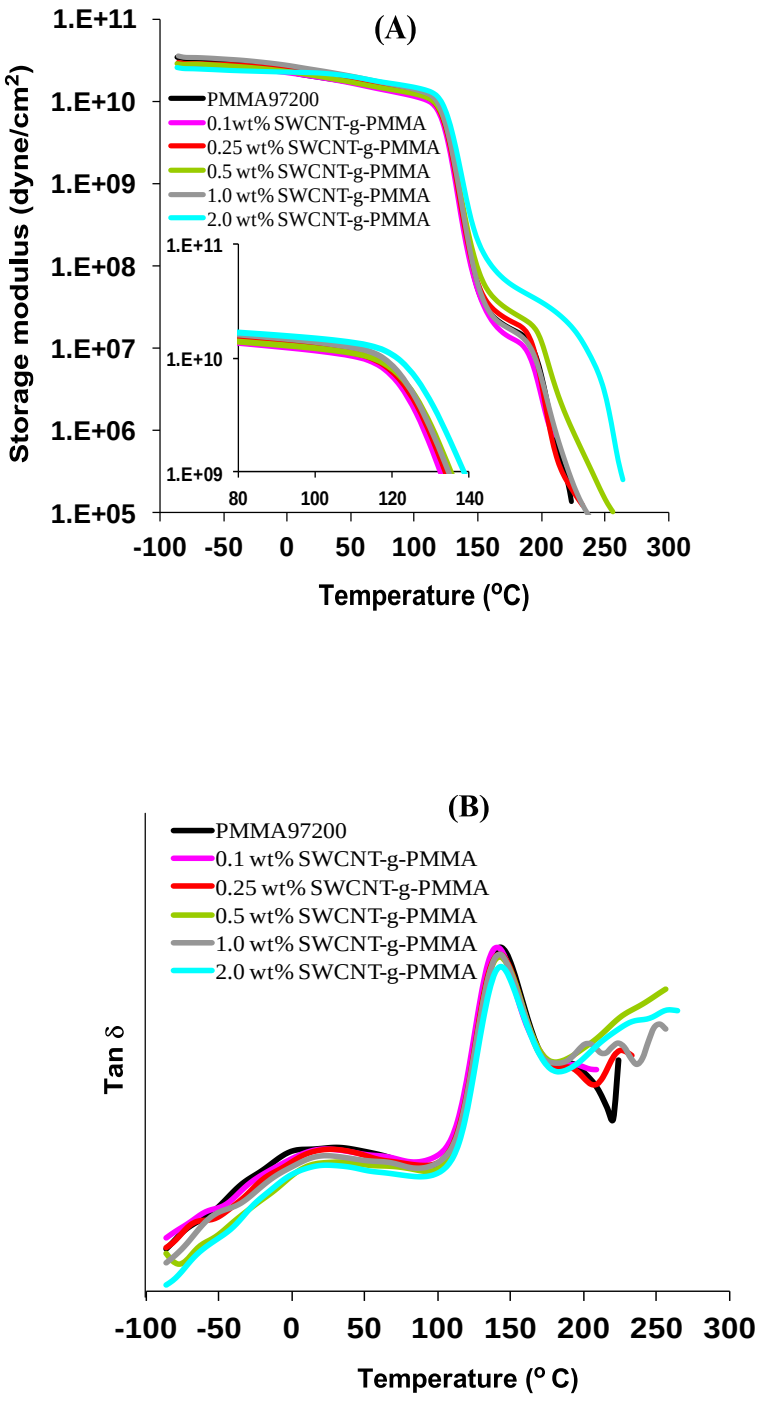

Figure 12. DMA of SWCNT-*g*-PMMA22600/PMMA97200 nanocomposites with temperature sweep. (A) storage modulus and (B) tan δ.

We focused on the storage modulus (E') because the largest changes occur in this rheological property due to the reinforcement of polymers by nanotube additions. For SWCNT-*g*-PMMA/PMMA nanocomposites where $M_{graft} \leq M_{matrix}$, the increase of the storage modulus, E', of PMMA after addition of SWCNT-*g*-PMMA is associated with the PMMA grafts on the SWCNT walls are compatible with chains of matrix PMMA. Similar increase in storage modulus of SWCNT/PMMA nanocomposites with nanotube loadings were reported on mixing of SWCNT into pure poly(methyl methacrylate) and on *in situ* polymerized single-walled carbon nanotube (SWNT)/PMMA nanocomposites.[61,62]

There is a substantial increase in storage modulus in both cases, $M_{graft} = M_{matrix}$ and $M_{graft} < M_{matrix}$ due to poor dispersion of SWCNT in PMMA matrices. Below T_g, the storage modulus, E', values of SWNT-*g*-PMMA/PMMA nanocomposites are almost identical to neat PMMA. At the vicinity of the glass transition (α), the E' values of SWNT-*g*-PMMA/PMMA nanocomposites are virtually identical because of large cohesive interactions between the high-surface area nanotubes and PMMA. Above T_g, there is a light increase in the storage modulus, E', for 0.25 and 0.5 wt% SWCNT-*g*-PMMA26600/26000 nanocomposites (Figure 11a) and 0.5 and 2.0 wt% SWCNT-*g*-PMMA22600/PMMA97200 nanocomposites (Figure 12a). The magnitude of increase in storage modulus, E', for 0.25 and 0.5 wt% SWCNT-*g*-PMMA26600/26000 nanocomposites is higher than 0.25 and 0.5 wt% SWCNT-*g*-PMMA22600/PMMA97200 nanocomposites, which indicates that nanocomposites with $M_{graft} = M_{matrix}$ are stiffer than nanocomposites consist of $M_{graft} < M_{matrix}$. Above T_g, nanocomposites made with matrix PMMA of number average molecular weight of 97200 g/mol have shown a substantial rubbery plateau which was absent for nanocomposites made with matrix PMMA of

number average molecular weight 26600 g/mol. The rubbery plateau may be due to the high molecular weight PMMA where there is not enough time for polymer chains to disentangle. This plateau region reflects the elastic nature of entangeled PMMA chains. Moreover, at the rubbery region there might be a formation of nanotube-nanotube networks or nanotube network entangled with polymer chains result in moderate control on the orientation of polymer chains, which leads to the formation of a rubbery plateau.[63,64] DMA T_g values are usually higer than those of DSC because DMA operates at higher frequency. Table 8 compares the T_g of composites measured from DSC and DMA analyses. The maximum change in T_g for composites where $M_{graft} = M_{matrix}$ is 3 ^oC at 2.0 wt% SWCNT measured by DSC and 5 ^oC at 1.0 wt% SWCNT obtained from tan δ value. On the other hand, the maximum change in T_g for composites where $M_{graft} = M_{matrix}$ is 1 ^oC at 1.0 wt% SWCNT measured by DSC and 2 ^oC at 0.25 wt% SWCNT obtained from tan δ value.

Table 8. Comparison of T_g of Composites Measured by DSC and DMA

sample identification number (SIN)	weight % of SWCNT	T_g (^oC) DSC	T_g (^oC) DMA
Composites where $M_{graft} = M_{matrix}$			
AC-83	0	113	137
AC-72	0.1	113	137
AC-73	0.25	114	137
AC-74	0.5	114	137
AC-75	1	115	142
AC-76	2	116	139
Composites where $M_{graft} < M_{matrix}$			
AC-84	0	118	142
AC-67	0.1	116	142
AC-68	0.25	118	144
AC-69	0.5	118	143
AC-70	1	119	143
AC-71	2	118	143

The maximum change in T_g obtained from both DSC and DMA measurements is higher for composites made from $M_{graft} = M_{matrix}$ than those of $M_{graft} < M_{matrix}$, which suggests that matrix PMMA of equal length to grafted PMMA wets the particles well than matrix PMMA smaller in length to grafted PMMA. These results are consistent with electrical conductivity data obtained on the same samples.

3.5 Conclusions

In summary, the wetting behavior of SWCNT in a chemically identical matrix melt can be controlled by grafting PMMA chains smaller, equal, and greater than the length of the PMMA matrices. Our functionalization method has little effect on the nanotube morphology and its electronic properties. DSC studies showed 8 ^oC rise in T_g for nanocomposites with $M_{graft} > M_{matrix}$ from the unfilled PMMA, 2 ^oC rise in T_g for when

$M_{graft} \approx M_{matrix}$ from the unfilled PMMA, and no change in T_g for nanocomposites where $M_{graft} < M_{matrix}$. When $M_{graft} \geq M_{matrix}$, conductivities reached a plateau value of 10^{-10} S/cm at 1.0 wt% SWCNT with percolation threshold of electrical conductivity at ~0.25 wt% of SWCNT. When $M_{graft} < M_{matrix}$, there was no sharp percolation threshold of electrical conductivity. There was a little increase in the storage modulus, E', with increasing SWCNT loadings for nanocomposites $M_{graft} \leq M_{matrix}$. At low temperature, we saw little change in storage modulus for nanocomposites, but storage modulus increased at the vicinity of T_g. Our method provides a facile way of tuning the nanotube surfaces controlling the thermal and mechanical properties of nanocomposites. Possible extensions of the results include the study of nanotube grafted brushes on chemically different melts and with copolymers.

References

1. Grady, B. P., *Carbon Nanotube-Polymer Composites: Manufacture, Properties, and Applications*. John Wiley & Sons: New York, 2011.
2. Winey, K. I.; Vaia, R. A., *MRS Bull.* **2007,** *32*, 314-319.
3. Krishnamoorti, R.; Vaia, R. A., *J. Polym. Sci: Part B: Polym. Phys*. **2007**, *45*, 3252-3256.
4. Krishnamoorti, R., *MRS Bull.* **2007,** *32*, 341-347.
5. Oh, H.; Green, P. F., *Nat. Mater.* **2009,** *8*, 139-143.
6. Meli, L.; Arceo, A.; Green, P. F., *Soft Matter* **2009,** *5*, 533–537.
7. Arceo, A.; Meli, L.; Green, P. F., *Nano Lett.* **2008,** *8*, 2271-2276.
8. Halperin, A.; Tirrell, M.; Lodge, T. P., *Adv. Polym. Sci.* **1992,** *100*, 31-71.
9. Grest, G. S., *Adv. Polym. Sci.* **1999,** *138*, 149-183.
10. Currie, E. P. K.; Norde, W.; Stuart, M. A. C., *Adv. Colloid Interface Sci.* **2003,** *100-102*, 205–265.
11. Shull, K. R., *J. Chem. Phys.* **1991,** *94*, 5723-5738.
12. Clarke, C. J.; Jones, R. A. L.; Edwards, J. L.; Shull, K. R.; Penfold, J., *Macromolecules* **1995,** *28*, 2042-2049.
13. Liu, Y.; Rafailovich, M. H.; Sokolov, J.; Schwarz, S. A.; Zhong, X.; Eisenberg, A.; Kramer, E. J.; Sauer, B. B.; Satija, S., *Phys. Rev. Lett.* **1994,** *73*, 440–443.
14. Sharma, S.; Rafailovich, M. H.; Sokolov, J.; Liu, Y.; Qu, S.; Schwarz, S. A.; Eisenberg, A., *High Perform. Polym.* **2000,** *12*, 581–586.
15. Oslanec, R.; Vlcek, P.; Hamilton, W. A.; Composto, R. J., *Phys. Rev. E* **1997,** *56*, R2383–R2386.
16. Oslanec, R.; Costa, A. C.; Composto, R. J., Vlcek, P., *Macromolecules* **2000,** *33*,

5505-5512.

17. Harton, S. E.; Kumar, S. K., *J. Polym. Sci., Part B: Polym. Phys.* **2008,** *46*, 351–358.

18. Trombly, D. M.; Ganesan, V., *J. Chem. Phys.* **2010,** *133*, 154904.

19. Jayaraman, A.; Schweizer, K. S., *Macromolecules* **2008,** *41*, 9430-9438.

20. Jayaraman, A.; Schweizer, K. S., *Macromolecules* **2009,** *42*, 8423–8434.

21. Lan, Q.; Francis, L. F.; Bates, F. S., *J. Polym. Sci., Part B: Polym. Phys.* **2007,** *45*, 2284–2299.

22. Xu, J.; Qiu, F.; Zhang, H.; Yang, Y., *J. Polym. Sci., Part B: Polym. Phys.* **2006,** *44*, 2811–2820.

23. Maillard, D.; Kumar, S. K.; Rungta, A.; Benicewicz, B. C.; Prudhomme, R. E., *Nano Lett.* **2011,** *11*, 4569–4573.

24. Green, P. F.; Oh, H.; Akcora, P.; Kumar, S. K., In *Dynamics of Soft Matter: Neutron Applications, Neutron Scattering Applications and Techniques*, Sakai, V. G.; Alba-Simionesco, C.; Chen, S., Eds. Springer Science Business Media LLC: Philadelphia, 2012.

25. Kalb, J.; Dukes, D.; Kumar, S. K.; Hoy, R. S.; Grest, G. S., *Soft Matter* **2011,** *7*, 1418–1425.

26. Bansal, A.; Yang, H.; Li, C.; Benicewicz, B. C.; Kumar, S. K.; Schadler, L. S., *J. Polym. Sci., Part B: Polym. Phys.* **2006,** *44*, 2944–2950.

27. Shull, K. R., *Faraday Discuss.* **1994,** *98*, 203-217.

28. Nair, N.; Wentzel, N.; Jayaraman, A., *J. Chem. Phys.* **2011,** *134*, 194906.

29. Ferreira, P. G.; Ajdari, A.; Leibler, L., *Macromolecules* **1998,** *31*, 3994-4003.

30. Pastorino, C.; Binder, K.; Kreer, T.; Muller, M., *J. Chem. Phys.* **2006,** *124*, 064902.

31. Mackay, M. E.; Tuteja, A.; Duxbury, P. M.; Hawker, C. J.; Horn, B. V.; Guan, Z.; Chen, G.; Krishnan, R. S., *Science* **2006,** *311*, 1740-1743.

32. Tuteja, A.; Duxbury, P. M.; Mackay, M. E., *Macromolecules* **2007,** *40*, 9427-9434.

33. Mackay, M. E.; Dao, T. T.; Tuteja, A.; Ho, D. L.; Horn, B. V.; Kim, H.-C.; Hawker, C. J., *Nat. Mater.* **2003,** *2*, 762-766.

34. Paul, A.; Grady, B. P.; Ford, W. T., *Polym. Int.* **2012**.

35. Becker, C.; Krug, H.; Schmidt, H., *Mat. Res. Soc. Symp. Proc.* **1996,** *435*, 237-242.

36. Berriot, J.; Montes, H.; Lequeux, F.; Long, D.; Sotta, P., *Macromolecules* **2002,** *35*, 9756-9762.

37. Grady, B. P.; Paul, A.; Peters, J. E.; Ford, W. T., *Macromolecules* **2009,** *42*, 6152–6158.

38. Tchoul, M. N.; Ford, W. T.; Lolli, G.; Resasco, D. E.; Arepalli, S., *Chem. Mater.* **2007,** *19*, 5765-5772.

39. Magenau, A. J. D.; Martinez-Castro, N.; Storey, R. F., *Macromolecules* **2009,** *42*, 2353-2359.

40. Tartar, A.; Gesquiere, J., -C., *J. Org. Chem.* **1979,** *44*, 5000-5002.

41. Qin, S.; Qin, D.; Ford, W. T.; Resasco, D. E.; Herrera, J. E., *J. Am. Chem. Soc.* **2004,** *126*, 170-176.

42. Tchoul, M. N.; Dalton, M.; Tan, L.-S.; Dong, H.; Hui, C. M.; Matyjaszewski, K.;

Vaia, R. A., *Polymer* **2012,** *53*, 79-86.

43. Ohno, K.; Ma, Y.; Huang, Y.; Mori, C.; Yahata, Y.; Tsujii, Y.; Maschmeyer, T.; Moraes, J.; Perrier, S., *Macromolecules* **2011,** *44*, 8944-8953.

44. Weisman, R. B.; Bachilo, S. M., *Nano Lett.* **2003,** *3*, 1235-1238.

45. Bachilo, S. M.; Balzano, L.; Herrera, J. E.; Pompeo, F.; Resasco, D. E.; Weisman, R. B., *J. Am. Chem. Soc.* **2003,** *125*, 11186-11187.

46. Dyke, C. A.; Tour, J. M., *Nano Lett.* **2003,** *3*, 1215-1218.

47. Liu, Y.; Yao, Z.; Adronov, A., *Macromolecules* **2005,** *38*, 1172-1179.

48. Pumera, M., *Langmuir* **2007,** *23*, 6453-6458.

49. Tchoul, M. N.; Ford, W. T.; Ha, M. L. P.; Chavez-Sumarriva, I.; Grady, B. P.; Lolli, G.; Resasco, D. E.; Arepallai, S., *Chem. Mater.* **2008,** *20*, 3120-3126.

50. Ramanathan, T.; Abdala, A. A.; Stankovich, S.; Dikin, D. A.; Herrera-Alonso, M.; Piner, R. D.; Adamson, D. H.; Schniepp, H. C.; Chen, X.; Ruoff, R. S.; Nguyen, S. T.; Aksay, I. A.; Prudhomme, R. K.; Brinson, L. C., *Nat. Nanotechnol.* **2008,** *3*, 327-331.

51. Flory, P. J.; Fox, T. G., *J. Am. Chem. Soc.* **1951,** *73*, 1904-1908.

52. Vasudevan, P.; Santappa, M., *J. Polym. Sci., Part B: Polym. Phycs.* **1971,** *9*, 483-497.

53. Hore, M. J. A.; Frischknecht, A. L.; Composto, R. J., *ACS Macro Lett.* **2012,** *1*, 115−121.

54. Akcora, P.; Kumar, S. K.; Sakai, V. G.; Li, Y.; Benicewicz, B. C.; Schadler, L. S., *Macromolecules* **2010,** *43*, 8275-8281.

55. Akcora, P.; Kumar, S. K.; Moll, J.; Lewis, S.; Schadler, L. S.; Li, Y.; Benicewicz,

B. C.; Sandy, A.; Narayanan, S.; IIavsky, J.; Thiyagarajan, P.; Colby, R. H.; Douglas, J. F., *Macromolecules* **2010,** *43*, 1003-1010.

56. Chung, H.-J.; Kim, J.; Ohno, K.; Composto, R. J., *ACS Macro Lett.* **2012,** *1*, 252-256.

57. Hore, M. J. A.; Composto, R. J., *ACS Nano* **2010,** *4*, 6941-6949.

58. Dutta, N.; Green, D., *Langmuir* **2008,** *24*, 5260-5269.

59. McEwan, M.; Green, D., *Soft Matter* **2009,** *5*, 1705-1716.

60. Brostow, W.; Lobland, H. E. H.; Narkis, M., *Polym. Bull.* **2011,** *67*, 1697–1707.

61. Ramanathan, T.; Liu, H.; Brinson, L. C., *J. Polym. Sci., Part B: Polym. Phycs.* **2005,** *43*, 2269-2279.

62. Putz, K. W.; Mitchell, C. A.; Krishnamoorti, R.; Green, P. F., *J. Polym. Sci., Part B: Polym. Phycs.* **2004,** *42*, 2286-2293.

63. Potschke, P.; Abdel-Goad, M.; Alig, I.; Dudkin, S.; Lellinger, D., *Polymer* **2004,** *45*, 8863-8870.

64. Du, F.; Scogna, R. C.; Zhou, W.; Brand, S.; Fischer, J. E.; Winey, K. I., *Macromolecules* **2004,** *37*, 9048-9055.

CHAPTER IV

SEMI-FLUORINATED QUATERNARY AMMONIUM POLYMER COLLOIDS AND COATINGS

ABSTRACT: Semifluorinated polymer latexes were prepared by semi-continuous emulsion polymerization of 10-30% of a fluoroalkyl methacrylate, 24% chloromethylstyrene, 3% styrylmethyl(trimethyl)ammonium chloride, and the reminder 2-ethylhexyl methacrylate under surfactant free conditions. The vinylbenzyl chloride units present only in the core were converted into quaternary ammonium ions by reacting with trimethylamine. These fluorine rich quaternary ammonium ions latexes at the concentration below 0.5 mg polymer / mL in the total reaction mixture were assessed as phase transfer catalysts in the form of both colloidal particles and coatings for the hydrolysis of Paraoxon. The dialyzed latexes and coatings, and the coatings made from undialyzed latexes showed no increase in the rate of hydrolysis. In contrast, undialyzed latexes in the form of colloidal particles had substantial catalytic activities which were probably due to the presence of soluble oligomers and/or unreacted monomers bearing quaternary ammonium ions sites. The glass transition temperatures for copolymers before

and after the quaternization of latexes were 10-17 ^{o}C and 39-40 ^{o}C respectively. The static contact angles of films of copolymers were from 117-121^{o} against water and 62-79^{o} against hexadecane were similar to homopolymers of perfluoroalkyl acrylates and methacrylates. Advancing and receding contact angles of spin coated quaternized latexes annealed at 130 ^{o}C for 48 h were found to be in the range of 106-115^{o}. AFM images of quaternized latexes showed that particles fused together after annealing latex coatings at 130 ^{o}C for 48 h, however, coatings were not uniform and had some rough surfaces. In nutshell, we conclude that the semi-fluorinated latexes were catalytically not active for the hydrolysis of Paraoxon because large numbers of fluorine atoms in the shell retarded the transport of Paraoxon from the solution to the catalytic quaternary ammonium sites in the core.

4.1 Introduction

Catalysis is important for many chemical reactions whether it is enzymatic reactions in living organism or in producing commodity chemicals. Two types of catalysts exist: homogeneous and heterogeneous. Heterogeneous catalysts that can be easily separated from the products are often reusable if they are not degraded chemically and physically or both, and are mostly stable under the reaction conditions. However, due to their complex structures heterogeneous catalysts are difficult to study, hence their reaction mechanisms are not well known. This chapter focuses on polymer-supported catalyst systems, a type of heterogeneous catalyst where catalytically active species are immobilized through chemical bonds, and their role in hydrolyses of Paraoxon, a toxic insecticide, in alkaline media. A universal challenge is to design and engineer the catalyst system considering

cost, applications, and ease of use without tempering their high activity and selectivity. The activity of heterogeneous catalysis depends on the high surface area of supports exposing the catalysts to the surrounding reactants. However, rates of reaction with heterogeneous catalysts depend on the mass transfer of reactants to the catalytic sites and products going away from the catalytic sites during the course of the reaction.[1] In the past decades, polymer-supported catalysis have been studied for a variety of chemical reactions.[2-7] In polymer-supported reactions, polymers are in the form of cross-linked beads and therefore totally insoluble in the reaction medium. These catalysts can be separated from the products or residual reactants by simple filtration. After removal of residual contaminants by repetitive washings, collected catalysts can be further used for catalysis reactions. This advantage has led many researchers to explore polymers as a support for synthesis and catalysis for variety of organic reactions.

Polymer colloids are defined as a dispersion of submicron polymer particles in a liquid, typically in an aqueous medium. A polymer colloidal particle contains a large number of polymer chains within the particle. Brownian motion is a key factor to stabilize colloidal particles because the thermal motion of the solvent molecules transfers momentum to the particles and maintains them in constant motion. The particle may be charge-stabilized or sterically-stabilized to prevent coagulation. The charged groups on the surface of a polymer colloid particle help in producing a stable dispersion of polymer particles. The particles repel each other and remain as separate entities in the medium for very long periods.[8] The common method used to synthesize polymer colloids of variety of sizes and compositions is free-radical emulsion polymerization. These polymer colloids are transformed into phase transfer catalysts by converting specific functional group (e.g. $-CH_2Cl$) of a monomer to quaternary ammonium ions. These quaternary

ammonium ions bearing colloids resemble other catalyst species such as micelle, polyelectrolyte, and ion-exchange resin, in terms of primary structures and compositions. They are crosslinked with a crosslinker such as divinylbenzene as shown in Scheme 1 to avoid dissolution in aqueous or organic media. Polymer colloids may have charged surfaces and nonpolar interiors like micelles. A colloidal particle catalyst has a typical diameter of 100 nm and is polymeric inside whereas a micelle has a diameter of 5 nm and its interior consists of aliphatic hydrocarbon chains. In some cases, colloidal particles may have their polymer chains extended into the water like polyelectrolyte, but those extended chains remain connected to the particle by cross-linking. Ion exchange latexes contain charged sites on the surface and inside may have similar structures and compositions as ion exchange resins. Ion exchange resins have diameters in the range of 10^4 to 10^6 nm whereas a colloidal catalyst has a diameter of 10^2 nm. In ion exchange resin catalysts, intraparticle diffusion of reactants and a catalyst's intrinsic reactivity often limit the reaction rates. On the other hand, polymer colloids offer much shorter average time for the reactants to reach the catalyst sites due to the smaller diameter. Since surface area per unit mass of a catalyst is inversely proportional to the diameter of a particle and the intraparticle diffusion times, the high surface area of polymer colloids eliminates mass transfer and diffusional limitations of the reactants and increases the rates of the reaction. However, high surface area does not indicate that the catalysis occurs only on the catalyst surface, and does not guarantee higher intrinsic activity of catalytic sites. Rather intrinsic activity of catalytic sites could be higher or lower than larger polymer particles.

Polymer colloids can be functionalized with specific groups or binding sites according to the need for the catalysis in many organic reactions, and catalysis occurs both on the particle surface which contains small amounts of charged species and inside the particle where maximum numbers of catalytic sites are present. The surface of particles is covered with charged species which are hydrated by water while the interior contains lipophilic hydrocarbon polymers or hydrophilic ion exchange sites.[9] Scheme 1 shows a synthesis of crosslinked copolymer latexes by emulsion copolymerization of 2-ethylhexyl methacrylate, vinylbenzyl chloride (VBC) which was finally converted to quaternary ammonium ion latexes by reaction with trimethylamine or tributylamine, divinylbenzene as a crosslinker, and a small amount of an ionic monomer (vinylbenzyl)trimethylammonium chloride.[9]

Scheme 1. General Structure of Copolymers as Phase Transfer Catalysts

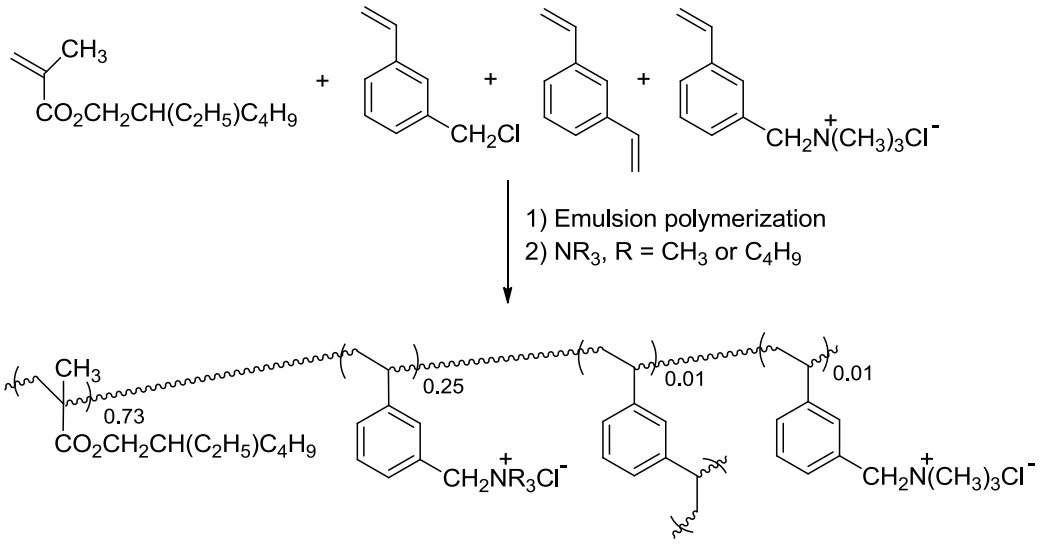

The major component in the core can be replaced by different types of alkyl methacrylates or styrene with varied weight fractions of VBC. The polymeric components inside the particles can be fine tuned to balance the hydrophobic/hydrophilic domains intended for improving particles intrinsic chemical activity. The groups on the surface of the particle may be varied, but the surface must be charged to stabilize the colloid. The reaction rates in colloidal particles depend on the intrinsic chemical reactivity of ion exchange sites and the intraparticle diffusion of reactants from the reactive solution to the particle. Hence, the reaction rates in colloidal particles can be altered by selecting proper materials and methods.

4.2 Colloidal Support and Phase Transfer Catalysts. Emulsion polymerization can be employed to synthesize cationic latexes with nonpolar monomer such as styrene or methyl methacrylate in presence of small amounts of ionic surfactants, for example hexadecyltrimethylammonium bromide (CTAB), and ionic initiators. In such latexes, surfactant and initiator are the components responsible for charges on the latex particles. One can synthesize latexes with more cationic charges by two steps: (1) First by polymerization of chloromethylstyrene by conventional emulsion polymerization, and (2) reaction of polymers with tertiary amines which converts the chloromethyl groups to quaternary ammonium ions. The resulting latexes were lightly cross-linked which makes colloids insoluble in the reaction medium.

Kinetics of displacement reaction between the water insoluble alkyl halides and water soluble inorganic salts using insoluble polymer-supported quaternary ammonium and phosponium ions, crown ethers, and poly(ethylene glycol)s of particle sizes 75-150 μm was low due to the poor mass transport of the reactant to ion exchange sites.[10] For

instance, polystyrene bound tetraalkylphosphonium ion (1) was used as a phase transfer catalyst in the displacement reaction between sodium cyanide and 1-bromoctane shown in Scheme 2, and the rate of the reaction was slower in the absence of vigorous agitation because of slower mass transfer of one or all reactants.[11,12] The rate of reaction of 1-bromooctane with aqueous sodium cyanide catalyzed by insoluble polystyrene-bound benzyltri-n-butylphosphonium salts was increased when the speed of mechanical stirring was increased to a maximum rate at 600 rpm and particle radius 'r' was decreased to a limiting value of $1/r = 1000\ cm^{-1}$. Further decrease in particle size had no effect on the rates of the reaction. The reaction rates were decreased as the percent of divinylbenzene cross-linking in the polymer was increased from 2% to 10% as the degree of swelling is decreased. The reaction rates were increased when the swelling power of the solvent was increased in the order decane < toluene < chlorobenzene. The lower the degree of cross-linking, greater is the swelling and the greater the volume fraction of the mobile liquid phase inside the particle. In bigger particles, reactants take longer time to reach the catalyst sites whereas highly cross-linked particles offer convoluted reactant flow to catalyst sites. Alternatively, smaller particles have higher surface area and shorter diffusion path length to the active sites per unit weight of the catalyst. The reactions with inherently slower reaction rates are independent of the stirring rate or the particle size. Thus, one can avoid intraparticle diffusional as well as mass transfer limitations by carrying out kinetics in a longer period of time.

Scheme 2. Displacement Reaction between Sodium Cyanide and 1-Bromoctane

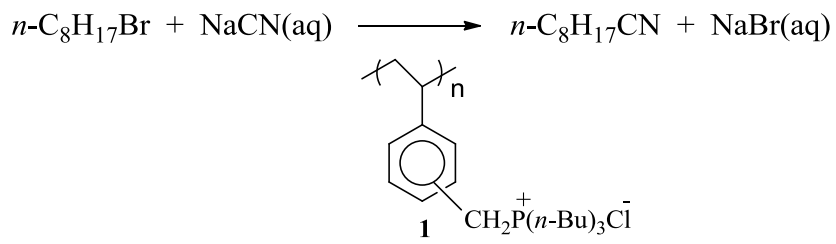

4.3 Catalytic Decontamination of Chemical Warfare Agents by Colloidal Polymers.

Certain chemical warfare agents (CWA) share chemical characteristics that present an opportunity for the development of countermeasures. The chemical agents, sarin, soman, and tabun (G-agents) are all examples of phosphorus-containing compounds which, when altered chemically at —P—X (X = F or CN) bond, can lose their toxicity. Mustard (an example of H-agent) and VX (an example of V-agent) can also be altered chemically to reduce their toxicity by oxidizing the S atom. Paraoxon is a type of organophosphorus compound and commonly used as a insecticide even though it displays high toxicity to humans.

The decontamination of toxic CWA is of great interest to the scientific community because of CWA threat to military and civil society. The aim of decontamination is to rapidly and effectively mitigate the toxicity of CWA both on personnel and equipment. The need for decontamination could be minimized to the extent possible by contamination prevention and early warning. For example, sensitive equipment and vehicle can be protected from toxic chemicals by means of suitable design and covering them with CWA resistant coatings. The "nerve" agents such as *O*-ethyl *S*-[2-(diisopropylamino)ethyl] methylphosphonothioate (VX), (*RS*)-propan-2-yl methylphosphonofluoridate (GB or Sarin), and 3,3-dimethyl-2-butyl

methylphosphonofluoridate (GD or Soman) and other toxic chemicals causing injury to human skin can easily penetrate plastics, rubber, and paint, and corrode metal surfaces, all of which make decontamination more difficult. Figure 1 shows the general structure of a CWA and Figure 2 shows chemical structures of few "nerve" agents.

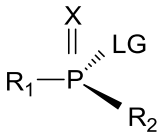

Figure 1. The general chemical structure of deadly organophosphorus compounds. Here, X = O or S; LG = leaving group; R_1 and R_2 = alkyl, O-alkyl, or O).

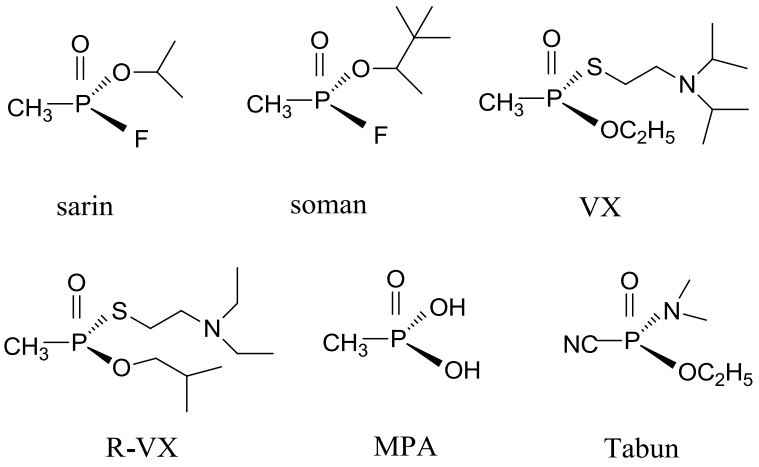

Figure 2. Chemical structures of some chemical warfare agents (sarin, soman, VX, R-VX, Tabun, and the degradation product common to all nerve agents, methylphosphonic acid (MPA).

In the past decades, much work has been done to develop a general method of detoxification of CWA.[13-16] One way of decontamination of these toxic materials is by

using nanoparticles like MgO,[17] CaO,[18] Al_2O_3[19] or TiO_2.[20] which absorb and chemically convert them into non-toxic compounds. Another way of decontamination of sensitive equipment and machinery is to transfer the toxic contaminants from the substrate to the fluorous solvents such as HFE-7100 and HFE- 7200 (isomeric mixtures of perfluoro-*n*-butyl and perfluoroisobutyl methyl and ethyl ether, respectively) and subsequent removal by adsorption onto activated carbon. However, this method does not reduce the toxicity of CWA and is linked to a scenario where disposal of carbon materials soaked with toxic organic chemicals is done either by burning or burying in landfills. Another class of materials that can be used for the decomposition of toxic organic compounds are polymers functionalized with primary amines or imines,[21-23] oximates,[24,25] amidoximes,[26] sulfonamides,[27] and quaternary ammonium fluorides.[28] Recently, we have reported catalytic hydrolysis of organophosporous and fluorophosphosporous esters by semi-fluorinated colloidal particles and coatings bearing 25 wt% of quaternary ammonium ions monomers in the polymer. These latexes promoted the hydrolysis of organophosporous esters in aqueous and fluorous media as phase transfer catalysts[29,30]

In 1971, Starks introduced the term "phase transfer catalyst" (PTC) to explain the catalytic role a tetralkylammonium or tetralkylphosphonium salt (Q^+X^-) plays in the displacement reactions of alkyl halides in an organic phase with an inorganic anions in an aqueous phase.[31] In this system, the rate of the reaction of 1-chlorooctane with aqueous sodium cyanide increases by 1000-fold on addition of 1.5 mol% of phase transfer catalysts Q^+X^- (hexadecyltributylphosphonium bromide). Key to this increase in the reactivity of cyanide ion is the generation of quaternary phosponium cyanide, which makes the cyanide ion available in the organic phase for nucleophilic reaction. The high

rate of reaction is due to the lipophilic nature and larger ionic radius of Q^+ pairing cation. Ever since that time, quaternary ammonium ions have been used in many forms such as surfactant micelles,[32] soluble polyelectrolyte,[33] colloidal particles,[21,34-36] and polymer-supported phase-transfer catalysts to promote reactions between water-soluble anions and organic substrates.[10,12,37,38] The polymer particles containing quaternary ammonium ions, extract the reactive anions or nucleophiles from the water and the organic reactants from the organic phase near the catalytic sites present inside the particles. Therefore, under such conditions the bimolecular reaction rate is much higher because of the higher concentration of the reactants at the vicinity of the nucleophile than in the overall reaction mixture. Kinetics of polymer colloids as a phase transfer catalyst often fit to the model shown in Scheme 3. In such systems, substrate partitions between the water phase and the particle phase with an equilibrium constant K_S and reacts with hydroxide ions or any other reagents in each phase with rate constants k_{2W} in water and k_{2L} in particles to form products.[36]

Scheme 3. Schematic of Kinetics of Hydrolysis of Substrate (S) to Product P in Aqueous Latex Dispersions

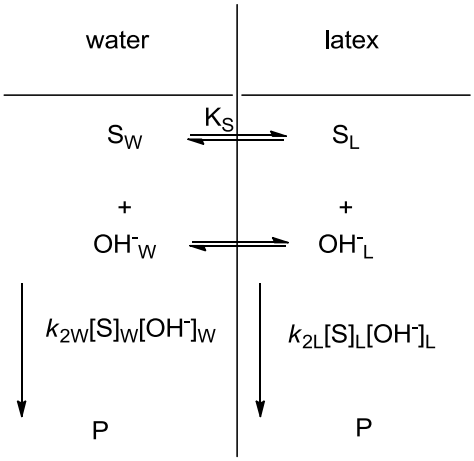

Summarizing, polymer-supported phase transfer catalysts are insoluble polymers or colloidal particles containing immobilized functional groups which act as a catalyst for reactions between anions and neutral organic substrates. Polymer colloidal particles promote the hydrolysis and oxidation reactions between the catalyst and the organic substrate in aqueous phase by increasing the concentration of catalysts and chemical reactants in the colloidal phase compared to the bulk at any point of reaction. The most common functional groups used on the polymer support are quaternary ammonium ions, phosphonium ions, crown ethers, or poly(ethylene glycols). Usually colloids are partially cross-linked to control the solubility of the particles, but highly cross-linked latexes reduce the diffusion of reactants to the catalytic sites resulting in decreasing the rates of hydrolysis. Other factors responsible for decreasing the hydrolysis of reactants are poor mass transfer of reactants from the solution to the particles and/or intraparticle diffusion of reactants to the catalytic sites of the particles. Thus, phase transfer catalysis by functionalized polymer colloids remains an effective way of detoxification of chemical warfare agents.

Herein we report the syntheses by the method of Scheme 1 of colloidal particles with core-shell morphology, where a core of 2-ethylhexyl methacrylate/VBC with a small amount of styrylmethyl(trimethyl)ammonium chloride is covered with 10-30 wt% of perfluoroalkyl methacrylate shell. We studied catalytic effects of latexes in the form of both colloidal particles and coatings for promoting decontamination of an organophosphate insecticide called Paraoxon. This is an extension of our previous work[30] where the semi-fluorinated latexes in both forms, particles and films, increased the rate of hydrolysis of *p*-nitrophenyl hexanoate (PNPH) and diethyl *p*-nitrophenyl phosphate

(Paraoxon). However, the type of fluoromonomer used, size of the particles, and amounts of the quaternary ammonium ions had very little effect on the rate of hydrolysis.[30] The purpose of the hydrophobic and oleophobic fluoro-shell is to repel the toxic organic compounds, and the purpose of the core containing quaternary ammonium ions is to hydrolyze toxic organic compounds that manage to penetrate the shell.

4.4 Research Objectives. The objectives of this work are as follows: (1) Prepare colloidal particles with fluorous surface which can be coated onto solid surfaces to repel Paraoxon, a simulant for nerve agents or other toxic chemicals. (2) Test the catalytic activity of the latexes in the forms of both particles and coatings towards hydrolysis of Paraoxon or other toxic chemicals. The long term applications for the latexes will be for protecting military equipment, buildings, aircraft and vehicle interiors, and developing self-cleaning coatings.

4.5 Experimental Section

4.5.1 Materials. Vinylbenzyl chloride (VBC, 96%, *m/p* isomeric mixture, Scientific Polymer Products, Inc.), 2-ethylhexyl methacrylate (*2*-EHMA, 98%, Aldrich), 1*H*,1*H*,2*H*,2*H*-perfluorodecyl methacrylate (PFDMA, SynQuest), and Zonyl® TM (2-(perfluoroalkyl)ethyl methacrylate) (DuPont, obtained from Aldrich; the value of *n* in the C_nF_{2n+1} group ranged from 6 to 8, and the fluorine concentration was 60 wt %) were purified before use by passing through basic aluminum oxide. Aluminum oxide (Al_2O_3, activated, basic, ~ 150 mesh, 58 Å, Aldrich), vinylbenzyl(trimethyl)ammonium chloride (VBTMACl, ≥ 98.0%, Aldrich), and 1-dodecanethiol (1-DT, ≥ 98.0%, Aldrich) were used as received. Acetonitrile (Aldrich) was dried overnight using 4 Å molecular sieves

prior to kinetic experiments. The initiator, 2,2-azobis(2-methylpropionamidine) dihydrochloride (V50, Aldrich) and aqueous 25% w/w solution of trimethylamine (Aldrich) were used as received. Diethyl *p*-nitrophenyl phosphate (Paraoxon) was purchased from Aldrich. Triply deionized water was used in all experiments.

4.5.2 Instruments and Measurements. FTIR spectra were recorded on Perkin Elmer 2000 FTIR spectrophotometer at a resolution 4 cm^{-1}. The spectra were averaged over 64 scans. Kinetic measurements were carried out on a Varian Cary 5000 spectrophotometer at 30 ± 0.3 ^{o}C. Spectrophotometer baseline was set to zero before for all experiments to avoid the contributions of the light scattering to the observed absorbance. DSC analyses were performed on TA Instruments DSC Q2000 by MDSC method over a temperature range of -85 to 200 ^{o}C with the ramp of 3 ^{o}C min^{-1}. The average value of glass transition temperature (T_g) of three different experiments were reported. The particle sizes (intensity average) of dilute unquaternized and quaternized colloidal latexes were obtained at 25 ^{o}C by dynamic light scattering on Malvern HPPS 3.1 instrument equipped with He-Ne, 3.0 mW, 633 nm laser. The samples for DLS measurement were prepared by diluting a drop of aqueous dispersion of copolymer with 10 mL of deionized water. Static contact angles on coatings from unquaternized latexes and dynamic contact angles on coatings from quaternized latexes before and after the dialysis were measured at 25 ^{o}C by an optical goniometer (Ramé-hart, 100 series). Each static contact angle value for water is the mean of six drops on two independently prepared polymer samples, whereas 3 data points were considered for hexadecane. In both types of experimental liquids, the average value of contact angles was reported. Wetting liquids used for contact angle measurements were 2 μL each of water and hexadecane. Advancing and receding contact

angle measurements were carried out on the same spin coated annealed films that were used for kinetic experiments. Morphologies of annealed coatings prepared on a glass surface with copolymers and quaternized latexes before and after the dialysis were studied by Veeco Multimode V SPM system with tapping mode at 25 ^{o}C.

4.5.3 Synthesis of Semi-Fluorinated Core-Shell Latexes. The core-shell particles were prepared by two-stage semicontinious emulsion polymerization technique described elsewhere.[39] In a typical reaction, 45 g of water and 0.220 g (1.04 mmol) of VBTMACl were added to a 150 mL round bottomed flask. After purging nitrogen gas for 20 min, this solution was heated under the mechanical stirring to reach the temperature 65 ^{o}C. Then 4.88 g (24.70 mmol) of 2-EHMA, 1.89 g (12.4 mmol) of VBC, and 0.117 g (0.58 mmol) of DT as a chain transfer agent were added to the solution and emulsified for 20 min with stirring under constant supply of nitrogen gas. The V50 initiator (0.075 g, 0.28 mmol) dissolved in 1 mL of water was then added to the solution. The addition of second stage monomer perfluoroalkyl methacrylate (FA) was started 60 min after initiation of the core part. FA of 0.751 g (1.41 mmol) was pre-emulsified with 0.050 g (0.23 mmol) of VBTMACl, and 0.71 g (13 mmol) of acetone as a co-solvent in water using ultrasonic emulsifier for 2 to 4 min at the power output of 15 W for 10-30 wt% of fluoromonomer. The FA pre-emulsion was added continuously at the rate of 0.01 g FA/min using a precision syringe pump. To ensure complete consumption of FA, the reaction mixture was stirred for another 2 h at 65 ^{o}C after the addition of FA pre-emulsion was finished. The reaction mixture was cooled to room temperature and filtered through a cotton plug to remove traces of coagulum to get a stable dispersion. The same procedure was repeated for synthesizing latexes with different amounts of perfluoroalkyl methacrylate

monomers and decreasing the same amounts of EHMA from the formulation. A blank latex sample was prepared by following the same procedure without adding any fluoromonomer. The weight percent solids were used to estimate the percent yield of latexes. Solid contents on all latexes were measured by weighing 1.0 g of latex accurately and drying to a constant weight at 110 ^{o}C. Determinations measured in triplicate were reproducible within 1% of the mean. Copolymers AF-22 and AF-24 were dialyzed through a cellulose membrane of MWCO 12500 for elemental analysis of F content whereas quaternized copolymers AFQ-22 and AFQ-24 were dialyzed through a cellulose membrane of MWCO 50000 for kinetic experiments for both particles and coatings.

4.5.4 Elemental Analyses for Fluorine Content in Copolymers before and after the Dialysis. Elemental analyses were done on latexes before and after the dialysis to determine fluorine content in copolymers. Fluorine content was determined by flask combustion followed by the ion chromatography at Atlantic Microlab, Inc. A sample calculation of mol% of fluoromonomer incorporated in copolymers is shown below for the sample AF-22. Total amount of monomers in AF-22 = 7.79 g. Amount of Zonyl® TM used in AF-22 recipe = 0.751 g.

$$\text{Zonyl® TM} = \frac{0.0964 \text{ g}}{\text{g copolymers}}$$

$$\text{Zonyl® TM} = \frac{0.18 \text{ mmol}}{\text{g copolymers}}$$

Elemental analysis showed 4.2 wt% of F in copolymers. Zonyl® TM contains 60 wt % of F atoms by weight.

$$\text{Zonyl}^{\circledR}\text{ TM} = \frac{0.042\text{ g}}{\text{g copolymers}} \times \frac{1\text{ mmol Zonyl}^{\circledR}\text{ TM}}{0.32\text{ g F Zonyl}^{\circledR}\text{ TM}}$$

$$= \frac{0.13\text{ mmol Zonyl}^{\circledR}\text{ TM}}{\text{g copolymers}}$$

The percent of fluoromonomer (Zonyl® TM) incorporated in the sample AF-22:

$$= \frac{0.13\text{ mmol}}{0.18\text{ mmol}} \times 100$$

$$= 72\ \%$$

Similarly, mol% of Zonyl® TM incorporated in other samples was calculated in the same fashion.

4.5.5 Quaternization of Copolymers. In a typical reaction, a 100 mL round bottomed flask was charged with 20 mL of latex (2.3 g of solid, 3.6 mmol of VBC groups), 14 mL of DI water, and 2.6 mL (2.5 g) of 25 wt% aqueous solution of trimethylamine. The reaction mixture was stirred at 60 ^{o}C for 48 h. The same amount of trimethylamine was added 3 more times during the reaction time. After 48 h excess trimethyl amine was removed by purging nitrogen gas in a fume hood for 4 h, and the reaction mixture was filtered through a cotton plug. Other latexes were quaternized by the same procedure. Quaternized latexes were dialyzed in 50,000 molecular weight cut-off regenerated cellulose Spectra/Por dialysis tubing for one week with constant stirring with magnetic stir bar. The water was changed 3 times on day 1 and twice per day for the rest of the 6 days. The amounts of chloride in the latexes were determined by potentiometric titration using an Orion 9617 chloride-selective electrode.[30] Quaternized latexes and quaternized dialyzed latexes were designated by ‘AQF’ and ‘AQFD’ respectively.

4.5.6 Percent Yield of Quaternization of Copolymers. The percent yield (%) of quaternization was calculated by the following steps:

Step (1)- Figure 3 shows the plot of ΔmV versus the volume of $AgNO_3$ (mL) used in the titration.

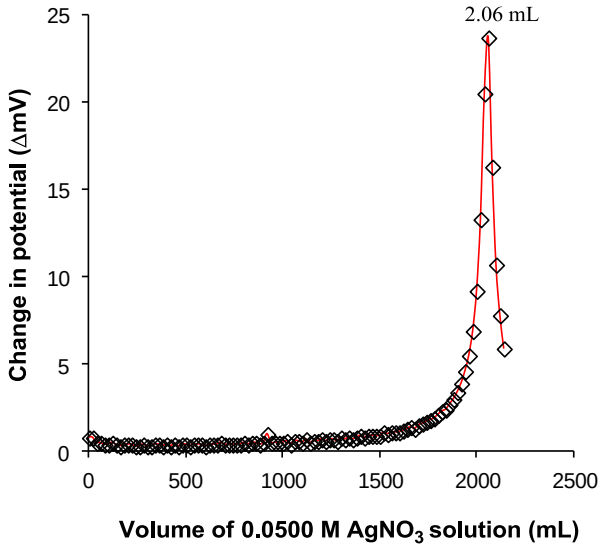

Figure 3. Potentiometric titration curve for AFQ-22 against 0.0500 M $AgNO_3$ (aq) solution.

The total amount of N^+Cl^- (mmol) = 0.0500 mmol/mL of Ag^+ ions x 2.06 mL

= 0.103 mmol of Cl^- ions per mL of AFQ-22 latex

Step (2)- The solid content (mg/mL) for the sample AFQ-22 is 61 mg/mL. The amount of N^+Cl^- in mmol/g = 0.103 mmol x 1/61 mg x 1000 mg/g = 1.69 mmol/g.

The contribution of chloride ions from the ionic monomer and the initiator was subtracted from the total chloride content while calculating the amount of Cl^- ions from the quaternization of VBC monomer.

Step (3)- From the weights of VBTMACl and V-50 used in the copolymers, mmol/g of both monomers were calculated and subtracted from the value of N^+Cl^- mmol/g calculated in step (2).

Total weight of monomers used in the sample AF-22 = 7984 mg.

(a) VBTMACl monomer used in the recipe = 1.0 mmol (0.271 g).

VBTMACl ions in 1 mL (61 mg) of latex = 1.0 mmol x 61 mg/ 7984 mg

$= 7.64 \times 10^{-3}$ mmol of VBTMACl ions.

VBTMACl ions (in mmol/g) $= 7.64 \times 10^{-3}$ mmol x 1000 mg/g x 1/61 mg

= 0.13 mmol/g of VBTMACl ions.

(b) V50 used in the recipe $= 2.77 \times 10^{-4}$ mmol (0.075 g).

V50 (mmol) in 1 mL (61 mg) of latex $= 2.77 \times 10^{-4}$ mmol x 61 mg/ 7984 mg

$= 2.11 \times 10^{-6}$ mmol of Cl ions.

V50 (in mmol/g) $= 2.11 \times 10^{-6}$ mmol x 1000 mg/g x 1/6 mg

$= 3.46 \times 10^{-6}$ mmol/g of VBTMACl ions.

The amount of N^+Cl^- from V50 is very low and ignored.

The final value of N^+Cl^- mmol/g = 1.69 mmol/g – 0.13 mmol/g.

= 1.56 mmol/g of Cl^- ions.

The final value of N^+Cl^- mmol/g corresponds to the amount of VBC monomer quaternized in the latex.

Amount of N^+Cl^- (mg) = N^+Cl^- mmol/g x 152.62 mg/mmol (molecular weight of VBC monomer).

Amounts of VBC monomer quaternized = 1.53 mmol/g x 152.62 mg/mmol = 234 mg/g. The weight% of VBC monomer used in the reaction is 24% which corresponds to 240 mg/g.

Thus, % yield of quaternization was calculated as follows:

$$\frac{N^{+}Cl^{-}\ mg/g}{240\ mg/g} \times 100 \quad \text{.....(1)}$$

Therefore, % yield of quaternization for AFQ-22 is:

$$\frac{234\ mg/g}{240\ mg/g} \times 100$$

$$= 98\ \%.$$

4.5.7 Preparation of Coatings. *(a) Drop-Cast Films.* The glass slides (2 cm x 0.8 cm) were washed with acetone and soaked in concentrated nitric acid for 1 h. Then the glass slides were washed with DI water, dried at 110 ^{o}C for 1 h, and stored in a desiccator. For static contact angle measurements unquaternized latex coatings were prepared by spreading a diluted dispersion (0.2-0.3 wt %) on a cleaned glass slide, coatings were dried at room temperature for 4 days, and annealed at 130 ^{o}C for 24 h. The annealed coatings were used to measure static contact angle using water. The same films were further used to measure the contact angle against hexadecane.

(b) Spin-Coated Films. The glass slides (2 cm x 0.8 cm) were washed with acetone, dried, and treated with a mixture of isopropyl alcohol and potassium hydroxide (1:1 w/w) for 1 h. Then the glass slides were washed with DI water, dried at 110 ^{o}C for 1 h, and stored in a desiccator. To a rectangular glass slide 10 μL of polymer dispersion was applied at the center and two edges and spun at 1200 rpm. Then speed of the spin coater

was slowly increased to 3000 rpm and held for 1 min. The dispersions were applied multiple times on the glass substrate, dried at room temperature for 24 h, and annealed at 130 ^{o}C for 48 h. The film thickness was measured from the weight of polymer deposited and the area of the glass substrate, assuming the density of latex to be 1.0 g/mL.

4.5.8 Kinetic Measurements for the Hydrolysis of Paraoxon in Presence of Colloidal Particles and Coatings. A stock solution of 2.5 mM of diethyl *p*-nitrophenyl phosphate (Paraoxon) was prepared with dried acetonitrile on the day of analysis. A 0.10 M NaOH solution was prepared in nitrogen-purged water and stored in an airtight container. Colloidal particles as a dispersion of AFQ-22 (1.22 mg, 20 μL) and 2.2 mL of nitrogen purged 0.1 M NaOH solution were added to a polystyrene cuvette. The mixture was equilibrated at 30.0 ± 0.3 ^{o}C for 20 min with magnetic stirring in the thermostated cell compartment of a Varian Cary 5000 spectrophotometer, and absorbance was set to zero. Then 74 μL Paraoxon stock solution in acetonitrile was added to make the reaction mixture concentrations [Paraoxon] = 8.5×10^{-5} M and $[N^{+}] = 9.1 \times 10^{-4}$ M. The absorbance of the solution at 400 nm was recorded every 0.9 s with constant stirring. The same procedure was followed for studying hydrolyses of Paraoxon using particles and coatings of AFQ-22 and AFQ-24 before and after the purification by dialysis.

First-order observed rate constants k_{obsd} were calculated using the equation

$$k_{obsd}\, t = \ln[(A_\infty - A_0) / (A_\infty - A_t)] \quad \text{.....(1)}$$

where t = time, A_0 = measured absorbance at t = 0, A_∞ = measured absorbance after 100% conversion, and A_t = measured absorbance at time t. The slope k_{obsd} was calculated by the linear least-squares method from the data over the first 60% conversion.

After completion of Paraoxon hydrolysis, the amounts of $PNPO^-$ in the solution and in the particles were determined. The reaction mixture was filtered through a 0.2 μm PTFE filter. The filter was washed with 1 mL of DI water. The volume of the combined filtrates and absorbance at 400 nm were measured to determine the amount of $PNPO^-$ in the aqueous phase. Then, the PTFE filter was washed with 2 mL of aqueous solution of 0.05 M $NaClO_4$ slowly over a period of 20 min followed by 1 mL of 0.1 M NaOH solution. The amounts of $PNPO^-$ ions displaced from the particles by perchlorate ions were calculated from the absorbance at 400 nm and the total volume of the filtrate in a cuvette. The sum of the amounts of $PNPO^-$ in the aqueous phase and in the particle phase accounted for 77-94 % of the starting Paraoxon.

4.6 Results

4.6.1 Synthesis of Semi-fluorinated Random Copolymers and their Corresponding Quaternary Ammonium Ion Latexes. The surfactant-free semi-fluorinated core-shell particles were prepared by a two-stage semi-continuous emulsion polymerization as shown in Scheme 4. By the semi-continuous method the solvent monomer 2-ethylhexyl methacrylate (*2*-EHMA) and the reactive monomer vinylbenzyl chloride (VBC) were polymerized to 80-90% conversion using the cationic monomer vinylbenzyl(trimethyl)ammonium chloride (VBTMACl) and the cationic initiator 2,2'-azobis(2-methylpropionamidine) dihydrochloride (V-50) for charge stabilization of the colloidal particles. The second stage of polymerization formed a shell by adding pre-emulsion containing fluoromonomer (1*H*,1*H*,2*H*,2*H*-perfluorodecyl methacrylate (PFDMA) or Zonyl® TM (mixture of homologous fluoroalkyl methacrylate esters), small

amount of VBTMACl, DI water, and acetone without further addition of initiator. Table 1 reports formulation details, polymerization conditions, and physical properties of core-shell latex particles.

Scheme 4. Synthesis of Cationic Polymer Colloids

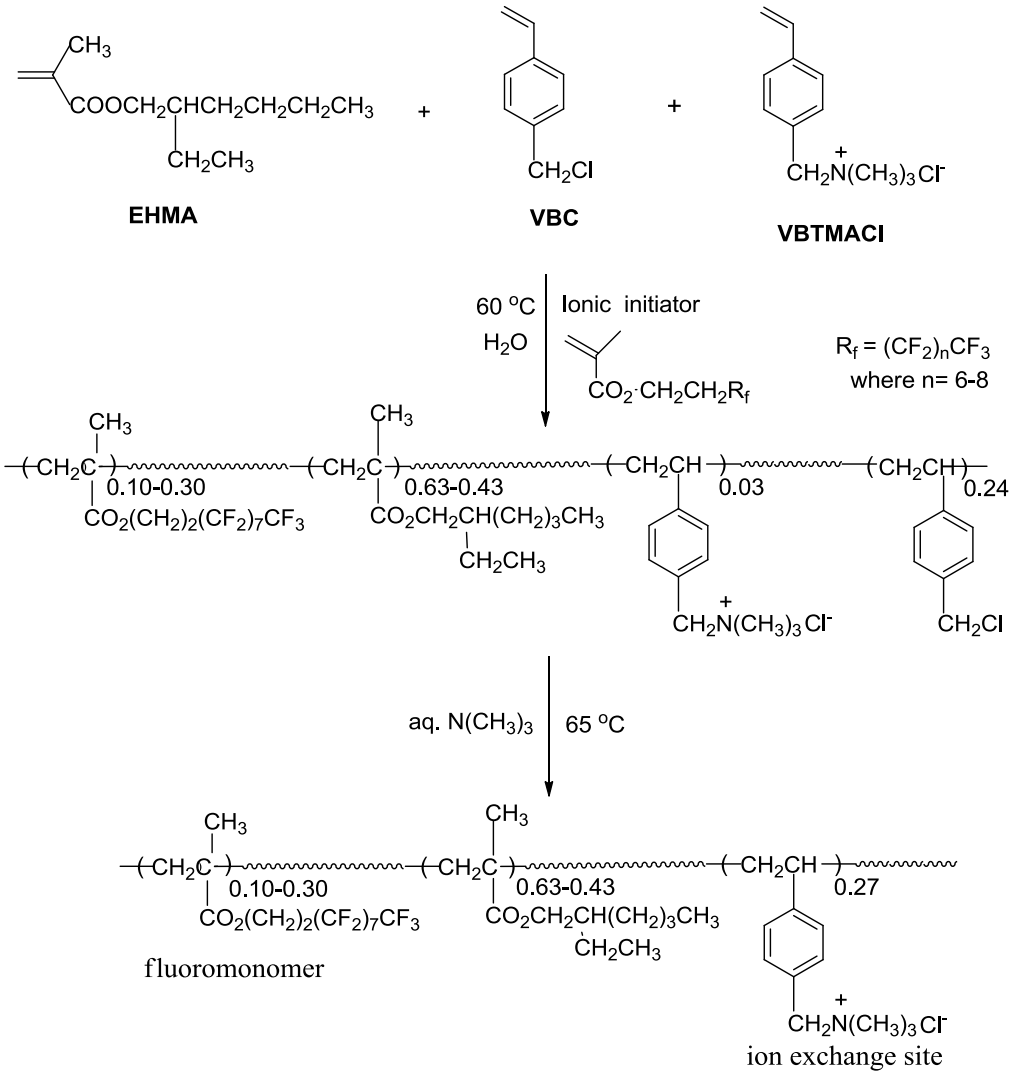

Table 1. Poly(perfluoroalkyl methacrylate) Core-Shell Latex Particles

ingredient	AF-11	AF-12	AF-13	AF-22	AF-23	AF-24
			First Stage (Batch)			
Water (g)	45	30	30	45	30	30
2-EHMA (g)	4.88	3.10	2.90	4.88	3.11	2.91
VBC (g)	1.89	1.40	1.61	1.89	1.41	1.60
VBTMACl (g)[a]	0.220	0.150	0.150	0.221	0.150	0.151
1-dodecanethiol (g)[b]	0.113	0.081	0.078	0.117	0.084	0.080
V-50 (g)[c]	0.075	0.050	0.050	0.075	0.050	0.050
			Second Stage (Semicontinuous)			
water (g)	5	7.3	13	5	7.3	13
FA (g)[d]	0.770	1.11	1.91	0.751	1.11	1.91
VBTMACl (g)[e]	0.049	0.070	0.130	0.050	0.071	0.130
acetone (g)	0.757	1.11	1.90	0.752	1.10	1.91
feeding time (min)	77	111	191	75	111	191
Wt% of FA	10	20	30	10	20	30
Yield (%)[f]	89	91	89	88	90	89
Core-shell particle size (nm)[g]	h	h	h	70	h	70

[a]Vinylbenzyl(trimethyl)ammonium chloride (VBTMACl), 3.3 % based on liquid monomers. [b]1.7 wt% based on liquid monomers. [c]2,2-azobis(2-methylpropionamidine) dihydrochloride, 1.1 wt% based on liquid monomers. [d]AF-11 to AF-13 contain 1*H*,1*H*,2*H*,2*H* perfluorodecyl methacrylate whereas AF-22 to AF-24 contain Zonyl® TM. [e]6.7 wt% based on FA. [f]Calculated from the weight of copolymers obtained and the weight of monomer mixture used for polymerization. [g]Hydrodynamic diameter measured by dynamic light scattering. [h]Not measured.

According to the preliminary study on the emulsion polymerization of 2-EHMA and VBC under the same reaction conditions described in Table 1, 80% of 2-EHMA and VBC were polymerized during the first 60 min of the polymerization as measured by gravimetric analysis. We employed the reactive ionic monomer VBTMACl and no low molar mass surfactant because cationic surfactant micelles have catalytic activity similar to that of the cationic particles and consequently could blur the distinction between the micellar and latex catalysis. In this study 1-dodecanethiol (DT) was used as a chain transfer agent to limit the molecular weight of the polymer in order to avoid early gelation and achieve high conversion. DT leads to lower molecular weight polymers and consequently lower viscosity within the particles.

Literature reported that the addition of 15-25 wt% of acetone increased the conversion of poly(perfluorooctylethyl methacrylate) or poly(perfluorooctylethyl acrylate) containing small amount of butyl acrylate with an average particle size less than 100 nm in diameter.[40] The resulting copolymers had less coagulation and excellent storage stability. Following the literature, in the second stage of emulsion polymerization we added 1.2-3.5 wt% of acetone as a co-solvent to the total amount of components used in the recipe including the weight of the water to facilitate the absorption of perfluoroalkyl methacrylate monomers into the shell of the particles. The mol percent of fluorine atoms, determined by elemental analysis, was found to be 15-26 mol % of fluoromonomers incorporated for copolymers EHMA-*co*-VBC-*co*-perfluoroalkyl methacrylate synthesized by shot-growth emulsion polymerization in the absence of acetone reported in the ref 30. The fluoromonomer content in the copolymers was increased to 67-83 mol% for the same copolymers synthesized by semi-continuous

emulsion polymerization and using acetone as a cosolvent in the second stage latex synthesis. Particles containing long chains of perfluoroalkyl groups on their surfaces are unfavorable for latex stability because heavy perfluoroalkyl groups repel water and attract one another. However, the presence of sufficient numbers of ionic sites on the particle surface aid in stabilizing the latexes. We noticed small amount of white colored deposit at the bottom of the bottle, where latexes were stored, which disappeared with slight shaking into the rest of the latex. In two separate vials small amount of AF-22 and AF-24 were dispersed in 20-fold of DI water and left for 24 h, similar deposit was observed which disappeared after slight shaking of the dispersion. We suspect that bigger latex particles settled at the bottom of the bottle, however, we did not observe bimodal distribution of particle size for any latex in DLS experiments. In emulsion polymerization, ionic sites on the particle surface are responsible for the stability of particles in water. Our latex particles consist of (a) a core rich in 2-EHMA, VBC, and a small amount of ionic monomer VBTMACl, (b) a shell containing 10-30 wt% of perfluoroalkyl methacrylate and a small amount of VBTMACl, and (c) a particle surface covered with ionic VBTMACl units. In some parts of copolymer chains, perfluoroalkyl methacrylate and the ionic repeat units mostly from the quaternized VBC monomer are immiscible. Note that the VBC and VBTMACl content of latexes were constant, and the sum of the EHMA and fluoroalkyl methacrylate contents was constant. Only the relative amounts of EHMA and fluoroalkyl methacrylate were varied in the syntheses of particles. The copolymers were modified into quaternary ammonium ions by treating with excess 25 wt% aqueous solution of trimethylamine as shown in Scheme 4. The percent yields of ionic groups in the copolymers were determined by measuring the amounts of chloride

counter ions of the quaternary ammonium ions in the latex and are reported in Table 2. AF samples reported in this work differ from BK samples[30] in three ways: (a) AF samples were prepared by a semi-continuous method whereas we used shot-growth polymerization technique to prepare BK samples, (b) In AF samples, all of the VBC monomer was added during the 1st stage of core formation. However, in BK samples, 73 wt% of VBC monomer was added during the core formation and the rest of the 27 wt% monomer was added in the second stage along with other monomers for the shell formation, (c) an outer shell of AF particles is more fluorous than BK samples and contains small amounts of quaternary ammonium ion units (VBTMACl) but no 2-EHMA. In BK samples, the outer shell contains fluoro monomers, EHMA, and quaternary ammonium ion units.

Table 2. Quaternized Latex Copolymers

N^+ polymer	diameter (nm)[a]	quaternization yield (%)[b]	volume ratio[c]	N^+Cl^- (mmol/g)	T_g (^oC)[d]
AFQ-22	92	97	2.3	1.69	40
AFQ-24	82	95	1.6	1.61	39
AFQD-22	120	50	5.0	0.83	e
AFQD-24	114	70	4.3	1.15	e
BK-6QF[f]	279	82	12.6	1.25	83
BK-11QF[f]	207	53	7.6	0.63	102

[a]Hydrodynamic diameter of quaternized undialyzed and dialyzed particles measured by dynamic light scattering. [b]Calculated from the chloride ion content values. [c](Volume of quaternized polymer particle)/(volume of precursor polymer particle) calculated from swollen particle diameters. [d]Glass transition temperature (T_g) of quaternized undialyzed particles measured by MDSC technique. [e]Not measured. [f]Ref 30.

4.6.2 FTIR Spectra of Zonyl® TM and Latex Copolymers. Fourier-transform infrared (FTIR) spectra of fluoromonomer and latexes with and without fluoromonomer are shown in Figure 4.

Seen in Figure 2(a), IR absorption of fluoromonomer Zonyl monomer at 1641 cm^{-1} for characteristic peaks of C=C bond and 817 cm^{-1} for =C—H bending. The stretching vibration absorption of C—F bonds of Zonyl TM were at 1100 ~ 1243 cm^{-1}. IR absorption at 564 ~ 815 cm^{-1} were characteristic of CF_3 groups. The stretching vibration absorption of ester C=O groups was at 1730 cm^{-1}.

Seen in Figure 2 (c), IR absorption of copolymers with no fluoromonomer at 3457 cm^{-1} is a typical characteristic peak for -OH group from the adsorbed water. IR absorption at 2933 and 2879 cm^{-1} were from -CH_2 stretching vibration. IR absorption at 1267 cm^{-1} was from -CH_2Cl group of VBC monomer and peaks at 1241 & 1183 cm^{-1} are from C—O single bond of EHMA polymer. The stretching vibration adsorption at 1732 cm^{-1} was of C=O functional group.

Seen in Figure 2 (b & d), spectra correspond to copolymers with 10 and 30 wt% of Zonyl® TM. Both spectra are similar to the IR absorption spectrum of latex containing no fluoromonomer. IR absorption at 3430 cm^{-1} is for -OH group from the adsorbed water. Disappearance of IR absorption at 1641 cm^{-1} for C=C bond showed the participation of all acrylate and fluoromonomers in polymerization. Both spectra have characteristic peaks for C—F bond at 1100 ~ 1243 $cm^{-1}$and 564 ~ 815 cm^{-1} overlap with the stretching vibration band of C—O—C bonds of ester groups at ~1200 cm^{-1} and strong stretching vibration C=O absorption peak at 1720 cm^{-1}.

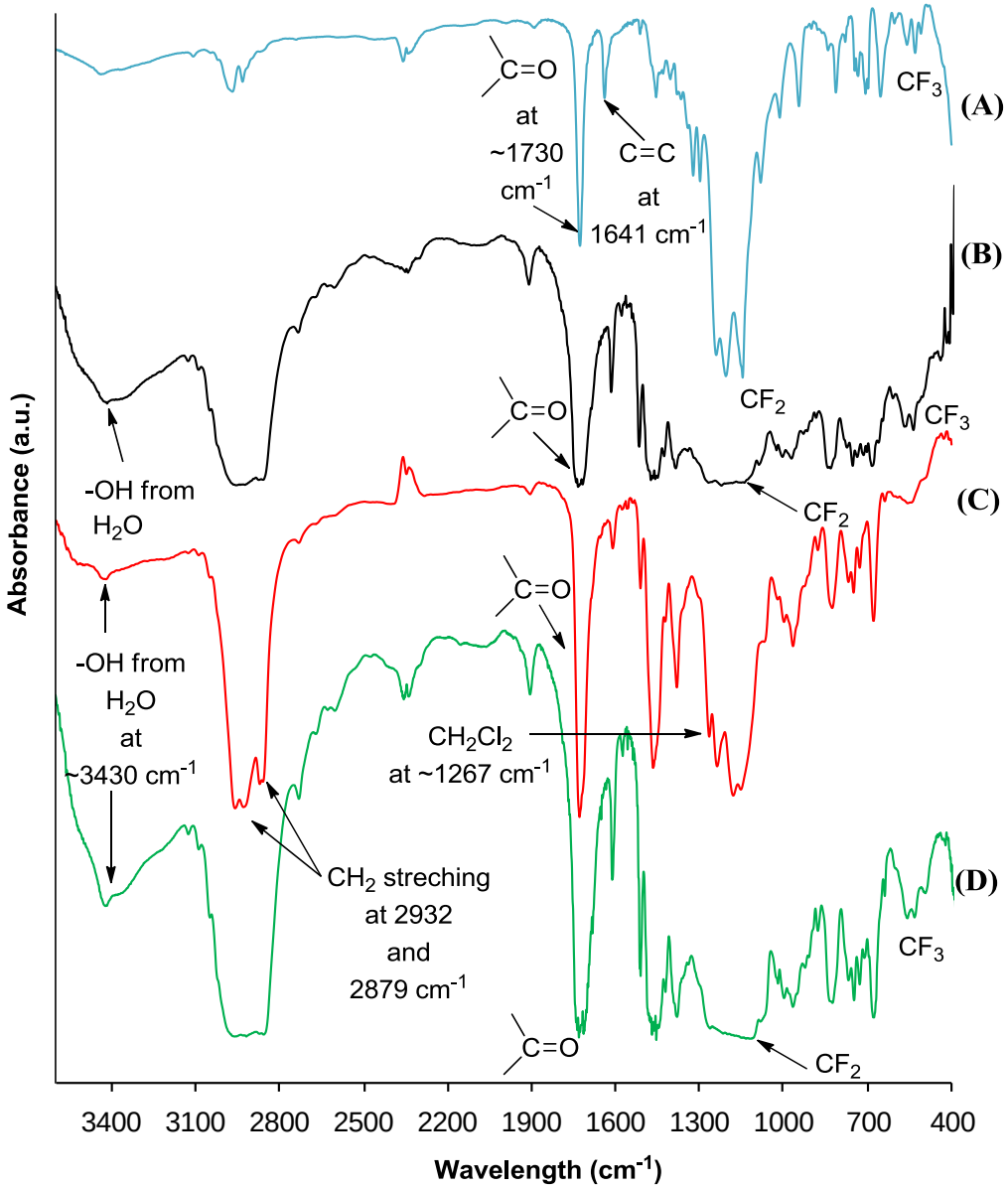

Figure 4. FTIR spectra of (A) Zonyl® TM fluoromonomer, (B) AF-22 copolymer with 10 wt% of Zonyl® TM, (C) copolymer with no FM, and (D) AF-24 copolymer with 30 wt% of Zonyl® TM.

The quaternization of copolymers was confirmed by the disappearance of a peak at 1267 cm^{-1} due to CH_2Cl of VBC in the FTIR spectra of AFQ-22 and AFQ-24. On the molar basis percent yield of quaternization was 50-70% for dialyzed samples and 95-97% for undialyzed latexes as reported in Table 2. The decrease in quaternization yield after the purification of latexes suggests that water soluble oligomers bearing quaternary ammonium ions, unreacted monomers, and surfactants were removed during the dialysis. The colloidal latexes had an average particle size of 70 nm measured by dynamic light scattering (DLS). The quaternized latexes have an average particle size of 82-120 nm measured by DLS are substantially larger than the copolymers due to the swelling of ionic copolymers in water. However, there is a little change in the diameters of the quaternized latexes before and after the dialysis compared to the unquaternized latexes in comparison to BK-6QF and BK-11QF samples reported in Table 2. In BKQ samples 73 wt% of VBC monomer is present in the core and 27 wt% in the shell, whereas in AF copolymers all of the VBC monomers are located in the shell with <1.0 wt% of ionic monomer (VBTMACl). Moreover, all AFQ copolymers are more hydrophobic in nature than all of the BKQ copolymers due to high F-monomer content. Thus, synergistic effects of ionic sites located in the core and limited equilibrium water uptake through the hydrophobic shell led AFQ copolymers to swell substantially in water. Thus, diameters of undialyzed BK-6QF and BK-11QF particles are twice the size of AFQ-22 and AFQ-24 latexes suggest that either AFQ particles have less ionic groups i.e. less quaternary ammonium ions or particles have less equilibrium water uptake due to the presence of more fluorine groups.

4.6.3 Differential Scanning Calorimetry. Glass transition temperatures (T_g) of the unquaternized and quaternized copolymers were measured by modulated differential scanning calorimetry (MDSC) with a ramp rate of 3 ^oC min^{-1}. The core of a particle contains low-T_g *2*-EHMA as a major monomer component and rest are high-T_g VBC with tiny amount of VBTMACl, whilst the shell has low-T_g poly(perfluoroalkyl methacrylate). T_g of unquaternized latexes AF-22 and AF-24 were 12 ^oC and 17 ^oC, well below room temperature, whereas quaternized latexes have higher T_g ca. 40 ^oC, due to the presence of large numbers of ionic repeat units. These ionic units have increased the intermolecular forces of attractions between polymer chains. The T_g's of homopolymers of *2*-EHMA and FA are inherently low. Only one glass transition temperature was observed for all copolymers in DSC thermograms implies a homogeneous composition. T_g of quaternized copolymers of newly synthesized latexes and latexes described in our previous study is reported in Table 2.

4.6.4 Elemental Analysis of Copolymers. We did elemental analyses on latexes before and after dialysis for F content in copolymers and is reported in Table 3. Elemental analyses for F in the precursor latexes before and after the dialysis were similar and within the range of 67-83 mol% of fluoromonomer compared to the calculated amount used for the reaction. These results suggest that most of the fluoromonomers are the part of the copolymer chains. On the other hand, BK-6F and BK-11F have 15 and 26 mol% of fluoromonomer incorporated in copolymer compared to the fluoromonomer used in the synthesis.

Table 3. Fluorine Analysis Data of AF and BK Samples

sample	weight (%) of Zonyl® TM in recipe	Zonyl® TM in recipe (mmol/g copolymers)	% of F content in copolymers[a]	Zonyl® TM in particle (mmol/g copolymers)	Zonyl® TM incorporated in copolymers (%)
AFQ-22	10	0.18	4.2	0.13	72
AFQ-24	30	0.53	14	0.44	83
AFQD-22	10	0.18	3.8	0.12	67
AFQD-24	30	0.53	14	0.44	83
BK-6QF	10	0.19	0.9	0.028	15
BK-11QF	25	0.47	3.8	0.12	26

[a]From elemental analysis of F-atom

4.6.5 Surface Characterization of Latex Coatings. The precursor and quaternized copolymers, before and after the dialysis, were applied to glass slides and annealed prior to contact angle measurements. Static contact angle was measured for unquaternized latexes whereas advancing/receding contact angles were obtained on quaternized undialyzed and dialyzed latexes. Atomic force microscopy (AFM) measurements were carried out on the same coatings used for contact angle measurements to elucidate the surface texture and roughness of the coatings.

4.6.5.1 Contact Angles of Water and Hexadecane on Latex Coatings. The evaluation of hydrobicity is made by measuring the contact angle of water on the surface of the substrate of interest. Surfaces with contact angles greater than 90 degrees are considered as hydrophobic and are superhydrophobic when greater than 150 degrees. Dynamic contact angle measurements can be used to estimate the quality of the surface in terms of roughness and inhomogenity in chemical composition of that surface.[41] Static contact angle is also called balanced contact angle. Advancing contact angle (θ_A)

demonstrates the wetting ability of a liquid on a solid surface whereas receding contact angle (θ_R) indicates the difficulty or ease to remove the liquid from the solid surface. In general, θ_A is larger than θ_R, due to roughness and inhomogeneity of the chemical composition of that surface.

Table 4 reports the static contact angles on drop coated annealed coatings made from precursor latexes and advancing/receding contact angles at 23 ± 2 ^oC of spin coated annealed films made from quaternized latexes before and after the dialysis. The static contact angles on annealed coatings made from precursor latexes were in the range of 117-121^o against water and 62-79^o against hexadecane. The static contact angle data on the precursor latexes against water are in good agreement with the literature values reported for perfluoroalkyl methacrylate and perfluoroalkyl acrylate homopolymers.[42,43] The *n*-hexadecane contact angle is generally accepted as the index of oleophobicity. For poly(1*H*,1*H*,2*H*,2*H*-perfluorododecyl methacrylate), this contact angle was found to be 83^o,[42] slightly higher than the static contact angle 62-79^o measured against hexadecane on annealed coatings of precursor latexes. A study on (perfluoroalkyl)ethyl methacrylate (Zonyl® TM) containing acrylic polymers were shown to be quite surface active in solution and as thin films. With levels at 1.5 wt% of (perfluoroalkyl)ethyl methacrylate monomer, water contact angles (advancing) of ~80-115° and hexadecane contact angles (advancing) of ~60-70° were observed.[44] These results are consistent with our contact angle data on highly fluorous AF acrylic copolymers. Upon annealing particle coatings in air the hydrophobic and oleophobic fluoroalkyl groups could migrate to the surface, and the hydrophilic quaternary ammonium ions could migrate beneath the surface. The hydrophobicity of coatings was checked manually by putting water droplets on the

coatings before and after the annealing. However, the final measurements were done on annealed coatings using ramé-hart instrument.

Table 4. Contact Angles on the Precursor and Quaternized Copolymer Coatings

polymer films (precursor)	polymer films (quaternized)	drop cast precursor latexes		spin coated quaternized latexes			
		water static 'θ' (deg)	hex[a] (deg)	thickness[b] (μm)	water θ_A[c] (deg)	water θ_R[d] (deg)	hex (deg)
AF-11	na	120	78	-	-	-	-
AF-12	na	120	79	-	-	-	-
AF-13	na	120	73	-	-	-	-
AF-22	AFQ-22	120	64	2.41	104	93	71
AF-23	na	117	62	na	na	na	na
AF-24	AFQ-24	121	75	0.98	116	92	66
AFD-22	AFQD-22	104[g]	-	0.92	104	86	61
AFD-24	AFQD-24	114[h]	-	0.46	106	102	55
BK-6F	BK-6QF-S120[e]	-	-	0.76	102	82	5
BK-11F	BK-11QF-S120 [f]	-	-	1.41	102	64	35

[a]Hexadecane. [b]Film thickness of quaternized latexes measured after annealing at 130 ^{o}C for 48 h. The average value of 6 readings is reported for static contact angle. [c,d]Advancing and receding contact angles ($\pm 2^{o}$) against water. The average value of 20 readings is reported for advancing and receding contact angles. [e,f]Details of samples are given in Ref 30. [g,h]Static contact angles of quaternized latex coatings.

Spin coated annealed quaternized latexes showed advancing and receding contact angles of 106-116^{o} against water and static contact angles of 55-71^{o} against hexadecane.

Thus, contact angle data of quaternized latexes suggest that quaternized annealed coatings are considerably hydrophobic and oleophobic in nature. The annealed films of quaternized latexes showed advancing and receding angles lower than the unquaternized latexes because of large number of hydrophilic quaternary ammonium chloride groups, limited mobility of fluoroalkyl groups, and random copolymer structures. Thus, the higher contact angles of on newly synthesized semi-fluorinated colloidal particle coatings (AF-22 and AF-24) compared with the previously reported[30] coatings (BK-6F and BK-11F)[30] are due to the higher amounts of fluorine on the particle surfaces.

4.6.5.2 Atomic Force Microscopy (AFM) of Coatings. Figure 5 shows height and phase images of spin coated films of quaternized latexes before and after the dialysis. The quaternized copolymer coatings were annealed at 130 ^{o}C for 48 h and analyzed by AFM under tapping mode. The AFM images of coatings prepared from undialyzed latexes show substantially rough surfaces. The process of film formation of polymers prepared by emulsion polymerization consists of three steps: (a) evaporation of water and formation of dense packing of polymer particles, (b) formation of continuous or pore-free polymer film due to deformation and coalescence of the polymer particles, if film is annealed above the glass transition temperature of the polymer, and (c) further gradual coalescence and fusion by interdiffusion of polymer between adjacent particles. The particle sizes measured on coatings of unquaternized latexes from AFM height images were 25-55 nm, smaller than the diameter calculated from dynamic light scattering data (DLS) of 70 nm. The larger diameters of wet than of dry latexes indicate substantial swelling in water. The surfaces of quaternized copolymer coatings annealed at 130 ^{o}C for 48 h were not uniform and showed oval shaped particles. AFM images on coatings of

unquaternized copolymers annealed at 130 ^{o}C for 48 h showed non uniform coatings, and particles are fused to the neighboring particles losing their inherent spherical shape and identity.

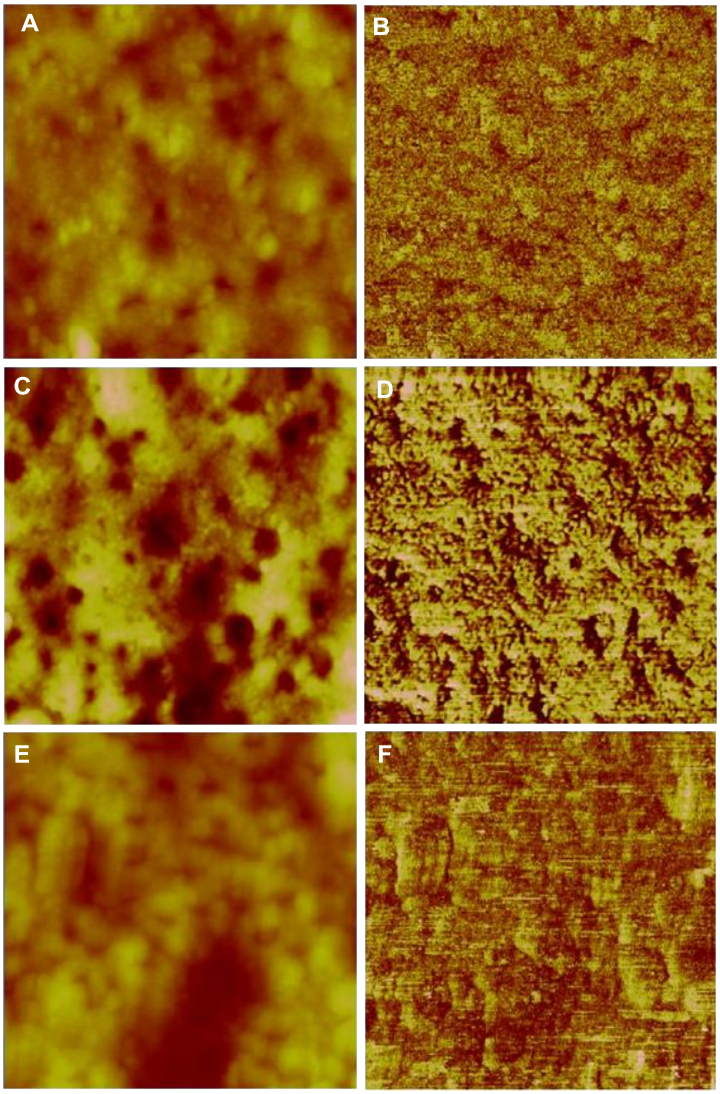

Height **Phase**

Figure 5. AFM images 1 μm × 1 μm of spin coated quaternized latexes annealed at 130 ^{o}C for 48 h for AFQ-22 (A and B), AFQ-24 (C and D), and AFQD-22 (E and F). Data scale for height, 30 nm.

We measured the surface roughness using two different statistical descriptors, (a) average surface roughness (R_a) and (b) root mean squared surface area roughness (R_q) or *RMS*, which provide the average variation of the surface height of the coating. Figure 6 is a schematic representation of surface roughness measurement parameters.

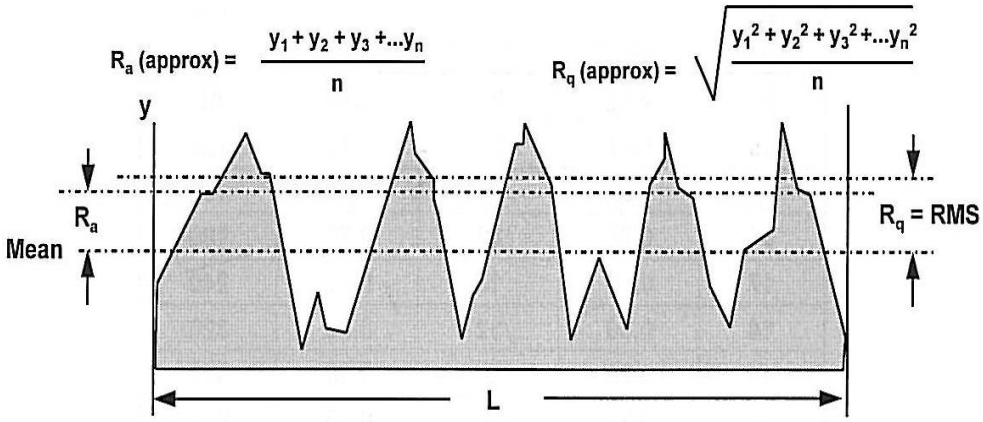

Figure 6. Surface roughness measurements- R_a and R_q.

R_a, R_q, and the surface texture were measured at 3 different places on the annealed coatings of quaternized and unquaternized copolymers shown in Figure 6. The average roughness measured at 3 different places of 1 μm × 1 μm at 30 nm height was less than 5 nm for all annealed coatings made with quaternized latexes before and after the purification apart from AFQD coatings. AFM images of annealed coatings on precursor and quaternized latexes show uniform coatings with an average surface roughness (R_a) and root-mean-square roughness (R_q) <5 nm except AFQD-24 which has R_a and R_q of 10 nm and 11 nm respectively. On the other hand AFM images of annealed spin coated films of quaternized latexes before and after the dialysis show non-uniform coatings with most of the particles having lost their identity and shape.

4.6.6 Hydrolysis of Paraoxon in Colloidal Particles. The cationic polymer colloids AFQ-22 and AFQ-24 which differ by the amounts of Zonyl® TM were tested as phase transfer catalysts for hydrolysis of Paraoxon under the basic conditions shown in Scheme 5. The acetonitrile solution of Paraoxon was prepared on the day of kinetics experiments and added quickly to the solution containing ion exchange catalysts in the polystyrene cuvette. The time between adding 74 μL of 2.5 mM Paraoxon in acetonitrile to the cuvette and data collection were less than 10 seconds in all cases. The experimental set up for the hydrolysis of Paraoxon using colloidal particles in 0.1 M NaOH solution is shown in Figure 7.

Scheme 5. Hydrolysis of Paraoxon

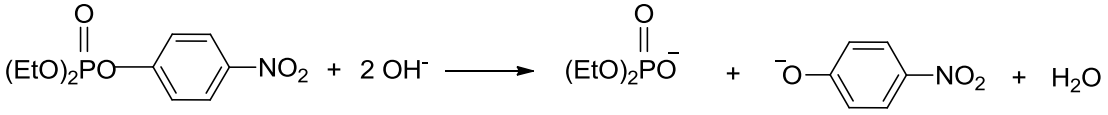

Paraoxon

p-nitrophenoxide (yellow)

Paraoxon was chosen for investigation because a wealth of literature is available on its hydrolysis using non-fluorinated latexes.[22,27,28,36,42] Hydrolyses were done in triplicate in absence of latex particles or coatings, in duplicate in presence of latex colloids, and only once for coatings because of difficulty of depositing quaternized latexes on the glass surfaces. Figures 8 and 9 show the absorbance at 400 nm of the hydrolysis product $PNPO^-$ against time with quaternized latexes AFQ-22 and AFQ-24 before and after the purification by dialysis. The amounts of particles are <0.5 mg/mL reaction mixture and the data follow pseudo-first-order kinetics. In case of latex particles before and after the

dialysis, the concentration of ion exchange sites ($[N^+]$ = (1.3-9.2) × 10^{-4}) exceeds the concentration of initial concentration of Paraoxon by 1.6-12 times. The half-lives of Paraoxon hydrolysis were 5.0-8.3 minutes for dispersion particles. Table 5 reports the conditions, mol% fluoromonomer in copolymers, $[N^+]$ concentration, half-lives, and first-order rate constant for the hydrolysis of Paraoxon using quaternized latexes before and after the dialysis.

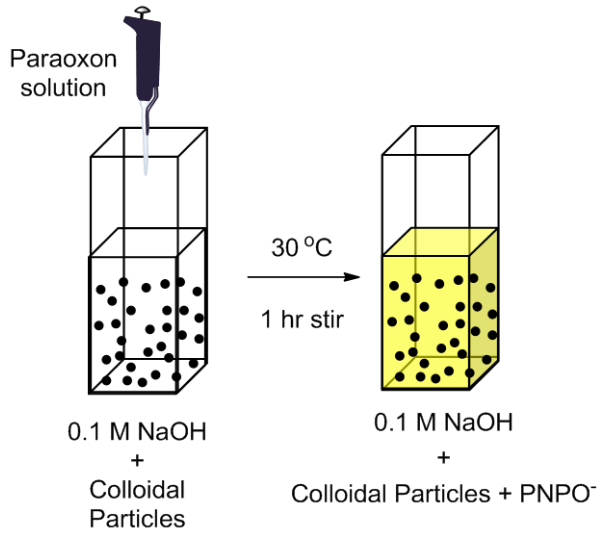

Figure 7. Hydrolysis of Paraoxon in colloidal particles dispersed in 0.1 M NaOH solution.

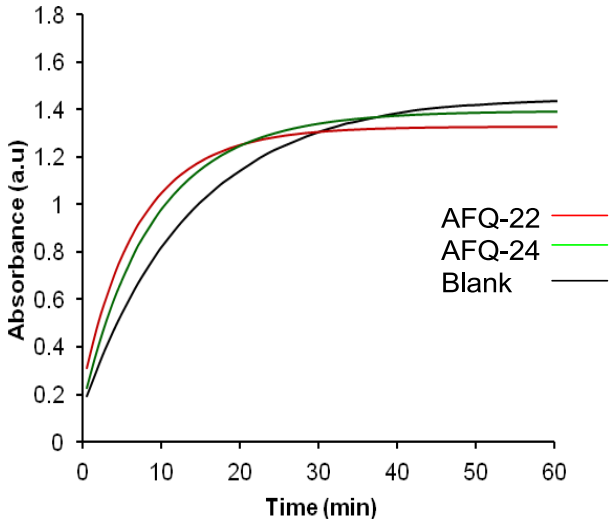

Figure 8. Change of absorbance at 400 nm due to $PNPO^-$ from hydrolysis of Paraoxon in 0.1 M NaOH solution at 30 ^oC in the presence of undialyzed particles.

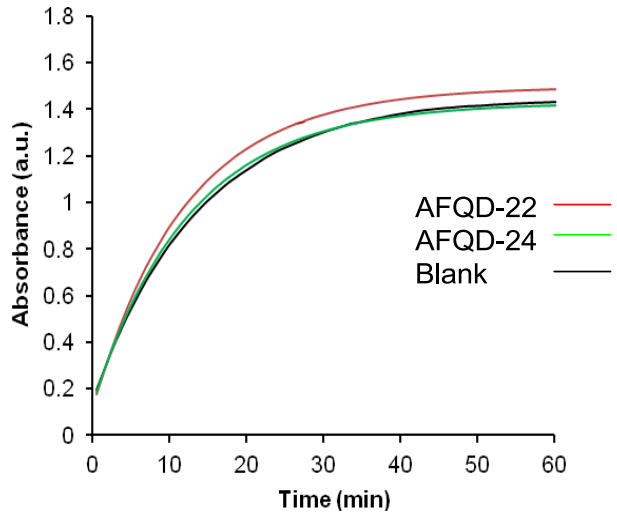

Figure 9. Change of absorbance at 400 nm due to $PNPO^-$ from hydrolysis of Paraoxon in 0.1 M NaOH solution at 30 ^oC in the presence of dialyzed particles.

Table 5. Kinetic Data Using Quaternized Particle Colloids

sample	mol % FM in copolymers	particles (mg)[b]	$[N^+]$ mmol/g	$[N^+]^c$ (M) x 10^{-4}	$[N^+]^d$ in shell (wt%)	vol. ratio[e]	k_1 (min^{-1})	$t_{1/2}$ (min)
AFQ-22	72	1.22	1.69	9.20	0.6	2.3	0.140 ± 0.004	5.0
AFQ-24	83	1.06	1.75	8.30	1.9	1.6	0.120 ± 0.003	5.8
AFQD-22	67	0.16	0.83	0.57	0.6	5.0	0.088 ± 0.003	7.9
AFQD-24	83	0.10	1.15	0.52	1.9	4.3	0.084 ± 0.003	8.3
BK-6QF	15	0.50	1.25	2.5	6.2	12.6	0.126	5.5
BK-11QF	26	0.64	0.63	1.8	6.2	7.6	0.173	4.0
Blank[a]		-		-		-	0.080 ± 0.002	9.0

[a]Hydrolysis of Paraoxon in 0.1 M NaOH solution in the absence of polymer catalysts. [b,c]In 2.29 mL of dispersion. [d]AF samples $[N^+]$ corresponds to VBTMACl ions, the only ion sites present in the shell, whereas for BK samples, $[N^+]$ in the shell includes VBTMACl and VBC, we assumed all VBC monomer are quaternized. [e](Volume of quaternized polymer particle)/(volume of precursor polymer particle) calculated from swollen particle diameters.

4.6.7 Hydrolysis of Paraoxon in Latex Coatings. All latexes before and after dialyses were spun coated on glass and annealed at 130 ^oC for 48 h. We measured the advancing and receding contact angles on coatings and used them further for kinetic

experiments. The coatings were inserted into the 0.1 M NaOH solution next to the cuvette side wall away from the path of the light, keeping the films exposed to the reactive solutions as shown in Figure 10. Plots of absorbance at 400 nm versus time after adding Paraoxon to the cuvette are shown in Figures 11 and 12. Table 6 reports the conditions, % fluoromonomer in copolymers, [N^+] concentration, half-lives, and first-order rate constant for the hydrolysis of Paraoxon using latex coatings before and after the dialysis. The concentration of Paraoxon in the reaction mixture is 1.4-2.3 times higher than the concentration of ion exchange sites for coatings made from the latexes before and after the dialysis. In all cases the rate constants were calculated from the data acquired during the first 60% conversion. The kinetic results on the hydrolysis of Paraoxon using AF-latex coatings as catalysts have a low rate of hydrolysis of Paraoxon due to highly flourous particle shell which either repel Paraoxon or reduces the diffusion of Paraoxon through shell to reach the ion exchange sites located in the core of the particles.

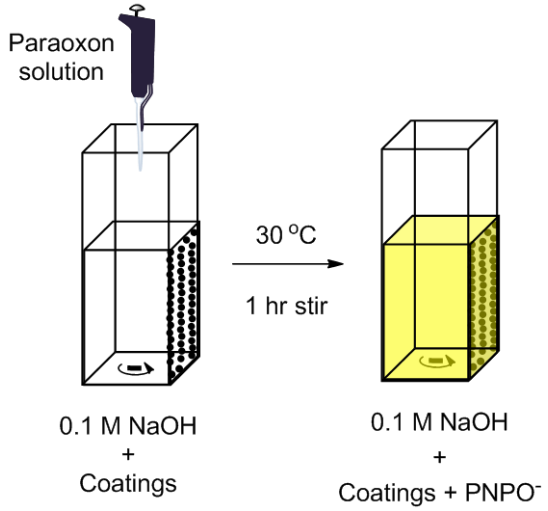

Figure 10. Hydrolysis of Paraoxon in the presence of latex coatings in 0.1 M NaOH solution.

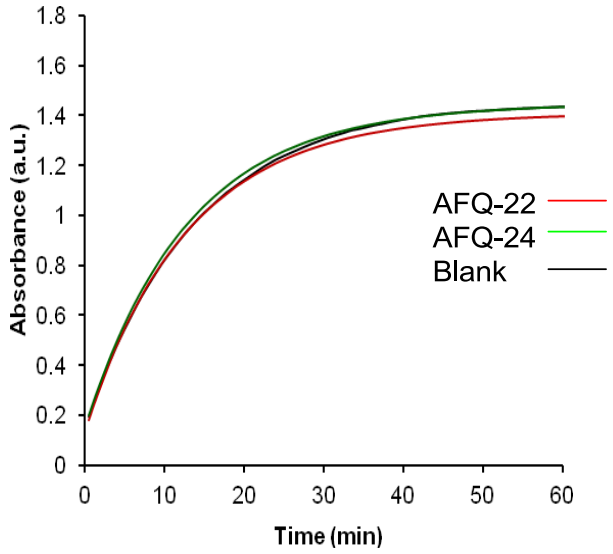

Figure 11. Change of absorbance at 400 nm due to PNPO- from hydrolysis of Paraoxon in 0.1 M NaOH solution at 30 ^{o}C in the presence of undialyzed latex coatings.

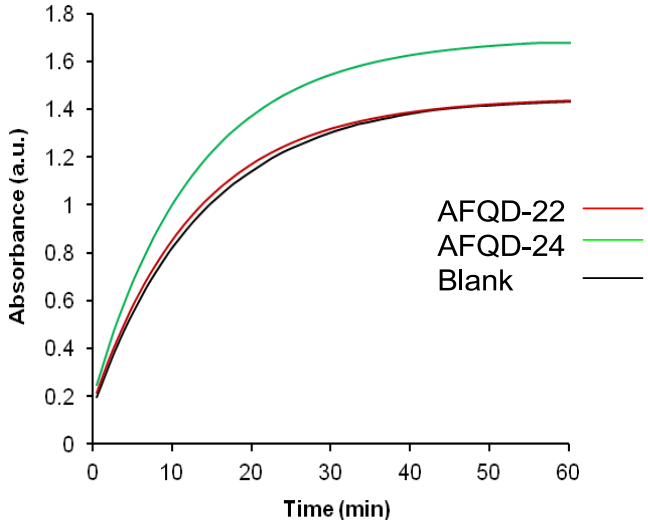

Figure 12. Change of absorbance at 400 nm due to PNPO- from hydrolysis of Paraoxon in 0.1 M NaOH solution at 30 ^{o}C in the presence of dialyzed latex coatings.

Table 6. Kinetic Data Using Quaternized Latex Coatings

sample	mol% FM in copolymer	particles (mg)[a]	coating thickness[b] (μm)	$[N^+]$ mmol/g	$[N^+]$ (M) x 10^{-4}	k_1 (min^{-1})	$t_{1/2}$ (min)
AFQ-22	72	0.42	2.41	1.69	3.20	0.082	8.5
AFQ-24	83	0.17	0.98	1.75	1.30	0.075	9.2
AFQD-22	67	0.16	0.92	0.83	0.59	0.080	8.7
AFQD-24	83	0.10	0.46	1.15	0.35	0.081	8.6
BK-6QF	15	0.50	0.76	1.25	2.7	0.072	2.7
BK-11QF	26	0.64	1.14	0.63	1.14	0.077	3.0
Blank[c]		-		-		0.080 ± 0.002	9.0

[c]In 2.29 mL of dispersion. [b]All coatings were annealed at 130 ^oC for 48 h. All coatings were covered by aluminum foil during annealing. [a]Hydrolysis of Paraoxon in 0.1 M NaOH solution in the absence of polymer catalysts.

The amounts of $PNPO^-$ in the solution after completion of hydrolysis of Paraoxon were determined by filtering the solution through a 0.2 µm PTFE filter, washing the filter with 1 mL of DI water, and measuring the total volume and absorption at 400 nm of the combined filtrates. The $PNPO^-$ in the particles was displaced from the particles into the solution by washing with 500 molar excess of perchlorate ions. The total molar amounts of hydrolysis product $PNPO^-$ were 76-94% of the amounts of the starting Paraoxon. The amounts of $PNPO^-$ recovered suggest high conversion of Paraoxon to $PNPO^-$ ions. The details of $PNPO^-$ ions in the solutions and particles are reported in Table 7.

Table 7. Amount of $PNPO^-$ Ions in Solution and Particles

sample	% $PNPO^-$ in solution	% $PNPO^-$ in particles
AFQ-22 (colloid)	77	11
AFQ-22 (coating)	76	0
AFQ-24 (colloid)	80	9
AFQ-24 (coating)	94	0

4.7 Discussion. The colloidal particles and coatings studied in this work for promoting the hydrolysis of Paraoxon were devised by two-stage emulsion polymerization to have >98% of the quaternary ammonium ions inside the particle covered with highly fluorous shell. Our previous work[30] on similar systems with less fluorous surface showed that the semifluorinated quaternary ammonium ion latexes have the same high phase transfer catalytic activity as the nonfluorinated analogues for basic hydrolysis of *p*-nitrophenyl hexanoate (PNPH) and Paraoxon in particle dispersions, and the films are almost as catalytically active as the particles for hydrolysis of Paraoxon. Substantial differences in fluoroalkyl methacrylate monomer, size, and quaternary ammonium ion content of the particles made little difference in rates of hydrolysis of Paraoxon. In comparison, newly synthesized latexes containing high amount of F on the particle surface as reported in Table 3 are not active either as particles or coatings in promoting hydrolysis of Paraoxon under the basic conditions. The major differences between the previously reported[30] catalytically active particles or coatings and catalytically inactive particles or coatings reported here are the following: (1) Previously synthesized samples had substantial amounts of catalytic sites or N^+Cl^- groups on the shell whereas samples reported in this paper have >98% N^+Cl^- groups in the core. (2) The shells of the old samples were less

fluorous compared to the shells of newly synthesized samples. (3) Particle diameters of quaternized latexes for AFQ and AFQD were 82-120 nm, less than the half of the diameters 207-279 nm for BK-6Q and BK-11Q quaternized undialyzed latexes.

Quaternized undialyzed colloids AFQ-22 and AFQ-24 gave Paraoxon half-lives of 5.0 and 5.8 min, similar to the most catalytically active samples BK-6QF and BK-11QF reported in Table 4, even though the concentration of ion exchange sites, $[N^+]$, in AFQ the mixture is higher at least by a factor of 3 to BK-6Q and BK-11Q samples. These results suggest that fluorine rich AFQ colloids hindered the penetration of Paraoxon to reach the catalytic sites present in the core. The dialyzed latexes AFQD-22 and AFQD-24 contain 18 times lesser amounts of ion exchange sites, $[N^+]$, compared to the undialyzed latexes due to lower amount of particles/mL and have longer half-lives ($t_{1/2}$) among all colloidal latexes. This slower in hydrolysis could be due to the combined effect of fluorous surface and the presence of lesser number of ion exchange sites for hydroxide ions exchange. The first order rate constants (k_1) reported in Table 5 are similar for BKQ samples and undialyzed AFQ samples even though AFQ colloids have substantially higher amounts of catalytic sites (8.3-9.2 M) than BKQ (1.8-2.5 M) samples. Colloids correspond to AFQD samples have first order rate constant similar to the value obtained from the blank experiment in absence of particles. Samples used previously[30] for kinetics experiments of hydrolysis of Paraoxon and *p*-nitrophenyl hexanoate (PNPH) were not dialyzed, but in this work we studied the undialyzed and dialyzed latexes in the forms of both particles and coatings for kinetic studies of hydrolysis of Paraoxon. Dialyses removed soluble by-products, unreacted and reactive monomers, and oligomers from the latexes. Thus, we argue that the catalytic hydrolysis of Paraoxon by dialyzed semi-

fluorinated latex particles and coatings are due to catalytic sites [N^+] immobilized on the particles. The catalytic hydrolyses of CWA simulants with latexes reported in our previous publication[30] were due to the combined effects of catalytic sites [N^+] immobilized on the particles and dissolved in the latex mixture. Smaller catalyst particles have higher surface area and shorter diffusion paths for reactants to the active sites per unit weight of catalysts. The diameters of quaternized latexes before and after the dialysis were 82-120 nm which are less than the half of 207-279 nm diameters of quaternized undialyzed latexes BK-6QF and BK-11QF reported previously.[30] The smaller path length AFQ or AFQD latex particles did not promote Paraoxon hydrolysis. We conjecture that flouorous shell repelled the Paraoxon to diffuse through the shell to active sites located in the core of particles.

All coatings made from AFQ latexes before and after the dialyses gave Paraoxon half-lives of 8.5-9.2 min, same as the blank experiment in the absence of polymer catalysts, reported in Table 6. AFQ-22 film of thickness 2.41 μm contains slightly higher amounts of catalyst sites than the BK-6QF and BK-Q11F coatings but the half-life of AFQ-22 is 8.5 min, three times higher than the BK coatings. AFQ-24 film has a coating thickness of 0.98 μm, slightly thicker than BK-6QF and twice the number of catalyst sites, but the half-life is three times longer than the BK-6QF and BK-Q11F coatings. The amounts of AFQD coatings on the glass were very low compared to BKQ and AFQ coatings. Therefore, coating thickness was less then BKQ coatings and hence smaller amounts of [N^+] were deposited. The AFQD coatings consist of 10-time smaller amount of catalyst sites than all coatings reported in Table 6 with half-lives similar to the blank experiment. AFQD-24 coatings have similar half-lives as AFQ designated coatings but

three times longer than BKQ latex coatings, although the thickness of AFQD coatings is half of the other coatings. Thus, coatings of quaternized latexes before and after the dialysis are less active than dispersions for Paraoxon hydrolysis. One important difference between AFQ and BKQ coatings is the distribution of VBC monomers between the core and shell. BKQ samples contain 77 wt% of VBC in the core and 23 wt% in the shell whereas in AFQ samples all the VBC units are located in the core, shell of AFQ samples contain 0.6 wt% and 2 wt% of VBTMACl units. In order to promote the rate of hydrolysis of organophosporous esters by more fluorinated latexes under basic conditions, the toxic organic compounds need to penetrate the fluorous shell to reach the catalytic sites located in the core of particles. All hydrolysis experiments have followed first-order kinetics.

In newly synthesized latexes most of the quaternary ammonium ions that might promote Paraoxon hydrolysis are present beneath the fluorous surface. More than 95% of quaternary ammonium ions come from quaternization of VBC monomer using trimethylamine, and less than 5% come from the ionic monomer VBTMACl. Compared to coatings reported in our earlier work,[30] AF latexes contain no VBC monomer in the shell. The shells of colloidal particles contain 10-30 wt% of FA and 0.6 to 1.9 wt% of reactive monomer (VBTMACl) which is the only available ion exchange sites present for promoting the hydrolysis reaction, in situation where the diffusion of organophosphrous esters to the core is limited due to fluorous surface of the shell. The kinetic hydrolysis of Paraoxon depends on the intrinsic activity at the [N^+] sites of latexes and on transport of both Paraoxon and hydroxide ions through the shell to the core of the particle.

4.8 Conclusions

In conclusions, semi-fluorinated latexes with quaternary ammonium ion groups were synthesized and tested for the promotion of hydrolysis of Paraoxon under basic conditions. Elemental analysis of dry precursor latexes revealed that 67 to 83 mol% of fluoromonomers (Zonyl® TM) were incorporated into the copolymers. Films of unquaternized copolymers with 10-30 wt% Zonyl® TM had static contact angles of 119-121^{o} against water and 62-79^{o} against hexadecane, which were same as those of homopolymers of perfluoroalkyl acrylates and perfluoroalkyl methacrylates. The T_g of unquaternized copolymers was below room temperature. AFM images on annealed films of copolymers show non-uniform coating surfaces. AFM images of annealed coatings of quaternized latexes indicated that the particles after annealing did not coalescence completely but lost their inherent spherical identity. Newly synthesized nanosize colloidal particles, which featured highly fluorous surfaces, did not promote the hydrolysis of Paraoxon due to the limited diffusion of Paraoxon through the shell to the catalyst sites [N^+] present in the core of the colloidal particles. Thus, hydrophobicity greatly influences the diffusion of Paraoxon into the core where most of the quaternary ammonium sites are located, and semi-fluorinated colloidal particles are ineffective in promoting the rate of hydrolysis. Elemental analyses for fluorine, contact angle data, and kinetics results support the argument that particles contain high amount of fluoralkyl groups on their surface, which repel Paraoxon, and hence newly synthesized latexes are catalytically inactive, both as colloidal particles and as coatings. Therefore, semi-fluorinated latexes can either act as phase transfer catalysts for hydrolysis of organophosporous compounds or repel the compound, but cannot do both.

References

1. Satterfield, C. N., *Mass Transfer in Heterogeneous Catalysis*. M.I.T. Press: Cambridge, 1970.
2. Hodge, P.; Sherrington, D. C., In *Polymer-Supported Reactions in Organic Synthesis*, Wiley: Chichester, 1980.
3. Ford, W. T., *Polymeric Reagents and Catalysts*. In *Am. Chem. Soc. Symp. Ser.*, 1986; Vol. 308.
4. Hodge, P., *Ind. Eng. Chem. Res.* **2005,** *44*, 8542-8553.
5. Lu, J.; Toy, P. H., *Chem. Rev.* **2009,** *109*, 815–838.
6. Kaur, I.; Kumari, V.; Dhiman, P. K., *J. Appl. Polym. Sci.* **2011,** *121*, 3185–3191.
7. Clapham, B.; Reger, T. S.; Janda, K. D., *Tetrahedron* **2001,** *57*, 4637-4662.
8. Ottewill, R. H., *Emulsion Polymerizaton*. Piirma, I., Ed. Academic Press: New York, 1982.
9. Ford, W. T., *React. Funct. Polym.* **2001,** *48*, 3-13.
10. Ford, W. T.; Tomoi, M., *Adv. Polym. Sci.* **1984,** *55*, 49-104.
11. Tomoi, M.; Ford, W. T., *J. Am. Chem. Soc.* **1980,** *102*, 7140–7141.
12. Tomoi, M.; Ford, W. T., *J. Am. Chem. Soc.* **1981,** *103*, 3821–3828.
13. Yang, Y. C.; Baker, J. A.; Ward, J. R., *Chem. Rev.* **1992,** *92*, 1729-1743.
14. Wagner, G. W.; Yang, Y. –C., *Ind. Eng. Chem. Res.* **2002,** *41*, 1925-1928.
15. Talmage, S. S.; Watson, A. P.; Hauschild, V.; Munro, N. B.; King, J., *Curr. Org. Chem.* **2007,** *11*, 285-298.
16. Bizzigotti, G. O.; Castelly, H.; Hafez, A. M.; Smith, W. H. B.; Whitmire, M. T., *Chem. Rev.* **2009,** *109*, 236-256.

17. Wagner, G. W.; Bartram, P. W.; Koper, O. B.; Klabunde, K. J., *J. Phys. Chem. B.* **1999,** *103*, 3225-3228.

18. Wagner, G. W.; Koper, O. B.; Lucas, E.; Decker, S.; Klabunde, K. J., *J. Phys. Chem. B.* **2000,** *104*, 5118-5123.

19. Wagner, G. W.; Procell, L. R.; O'Connor, R. J.; Munavalli, S.; Carnes, C. L.; Kapoor, P. N.; Klabunde, K. J., *J. Am. Chem. Soc.* **2001,** *123*, 1636-1644.

20. Hirakawa, T.; Sato, K.; Komano, A.; Kishi, S.; Nishimoto, C. K.; Mera, N.; Kugishima, M.; Sano, T.; Ichinose, H.; Negishi, N.; Seto, Y.; Takeuchi, K., *J. Phys. Chem. C* **2010,** *114*, 2305–2314.

21. Bromberg, L.; Hatton, T. A., *Polymer* **2007,** *48*, 7490-7498.

22. Bao, Y. T.; Pitt, C. G., *J. Polym. Sci. A Polym. Chem.* **1990,** *28*, 741-758.

23. Hammond, P. S.; Forster, J. S., *J. Appl. Polym. Sci.* **1991,** *43*, 1925-1931.

24. Bromberg, L.; Hatton, T. A., *Ind. Eng. Chem. Res.* **2005,** *44*, 7991-7998.

25. Bromberg, L.; Hatton, T. A., *Ind. Eng. Chem. Res.* **2007,** *46*, 3296-3303.

26. Bromberg, L.; Schreuder-Gibson, H.; Creasy, W. R.; McGarvey, D. J.; Fry, R. A.; Hatton, T. A., *Ind. Eng. Chem. Res.* **2009,** *48*, 1650–1659.

27. Gutch, P. K.; Singh, R.; Acharya, J., *J. Appl. Polym. Sci.* **2011,** *121*, 2250–2256.

28. Marciano, D.; Goldvaser, M.; Columbus, I.; Zafrani, Y., *J. Org. Chem.* **2011,** *76*, 8549–8553.

29. Zhu, Y.; Ford, W. T., *Langmuir* **2009,** *25*, 3435-3439.

30. Kaur, B.; McBride, S. P.; Paul, A.; Ford, W. T., *Langmuir* **2010,** *26*, 15779–15785.

31. Starks, C. M., *J. Am. Chem. Soc.* **1971,** *93*, 195–199.

32. Bunton, C. A.; Savelli, G., *Adv. Phys. Org. Chem.* **1987,** *22*, 213-309.

33. Murugan, E.; Sherman Jr., R. L.; Spivey, H. O.; Ford, W. T., *Langmuir* **2004,** *20*, 8307-8312.

34. Miller, P. D.; Ford, W. T., *Langmuir* **2000,** *16*, 592-596.

35. Miller, P. D.; Spivey, H. O.; Copeland, S. L.; Sanders, R.; Woodruff, A.; Gearhart, D.; Ford, W. T., *Langmuir* **2000,** *16*, 108-114.

36. Seabolt, E. E.; Ford, W. T., *Langmuir* **2003,** *19*, 5378–5382.

37. Regen, S. L., *J. Am. Chem. Soc.* **1975,** *97*, 5956-5957.

38. Cinouini, M.; Colonna, S.; Molinari, H.; Montanari, F., *J. Chem. Soc., Chem. Commun.* **1976,** (11), 394-396.

39. Ha, J. -W.; Park, I. J.; Lee, S. -B.; Kim, D. -K., *Macromolecules* **2002,** *35*, 6811-6818.

40. Linemann, R. F.; Malner, T. E.; Brandsch, R.; Bar, G.; Ritter, W.; Mulhaupt, R., *Macromolecules* **1999,** *32*, 1715-1721.

41. Gao, L.; McCarthy, T. J., *Langmuir* **2006,** *22*, 6234-6237.

42. Tsibouklis, J.; Graham, P.; Eaton, P. J.; Smith, J. R.; Nevell, T. G.; Smart, J. D.; Ewen, R. J., *Macromolecules* **2000,** *33*, 8460-8465.

43. Gupta, M.; Gleason, K. K., *Langmuir* **2006,** *22*, 10047-10052.

44. Thomas, R. R.; Anton, D. R.; Graham, W. F.; Darmon, M. J.; Sauer, B. B.; Stika, K. M.; Swartzfager, D. G. *Macromolecules* **1997**, 30, 2883-2890.

VITA

Abhijit Paul

Candidate for the Degree of

Doctor of Philosophy

Thesis: POLYMER FUNCTIONALIZED SINGLE-WALLED CARBON NANOTUBE COMPOSITES AND SEMI-FLUORINATED QUATERNARY AMMONIUM POLYMER COLLOIDS AND COATINGS

Major Field: Chemistry

Biographical:

Personal Data: Born in Silchar, Assam, On December 31, 1979, Son of Arabinda Mohan Paul and Manju Rani Paul.

Education: Graduated from Kendriya Vidyalaya Silchar, Assam in May, 1998; received Bachelor of Science degree in Chemistry from Assam University, Silchar, Assam in 2001; received Master of Science degree in Polymer Science from Tezpur University, Tezpur, Assam in 2003, respectively. Completed the requirements for the Doctor of Philosophy in Chemistry at Oklahoma State University, Stillwater, Oklahoma in July, 2012.

Experience: Employed by United Rubber Industries (I) Pvt. Limited, Mumbai, India as Quality Assurance Engineer July 2003-February 2005; employed by Asian Paints Ltd., Mumbai, India, as Polymer Technologist, March 2005-July, 2007; employed by Oklahoma State University, Department of Chemistry as graduate research and teaching assistant, 2007 to present.

Professional Memberships: American Chemical Society

ACS, Polymer Chemistry Division
ACS, Division of Polymeric Materials: Science and Engineering

Name: Abhijit Paul Date of Degree: July, 2012

Institution: Oklahoma State University Location: Stillwater, Oklahoma

Title of Study: POLYMER FUNCTIONALIZED SINGLE-WALLED CARBON NANOTUBE COMPOSITES AND SEMI-FLUORINATED QUATERNARY AMMONIUM POLYMER COLLOIDS AND COATINGS

Pages in Study: 194 Candidate for the Degree of Doctor of Philosophy

Major Field: Chemistry

Scope and Method of Study: Current study focused on understanding of "*wetting*" and "*dewetting*" phenomena between surfaces of single-walled carbon nanotubes (SWCNT) which are lightly grafted with polymer chains by reversible-deactivation radical polymerization, when they are mixed with matrix chains of the same architecture as grafts. Effects of grafts to matrix chain lengths on SWCNT dispersion in matrix polymers were studied by measuring electrical conductivity, glass transition temperature, and storage and loss moduli of nanocomposites. Another area of work was to design semi-fluorinated copolymers with core-shell morphology by emulsion polymerization, study their catalytic activities for hydrolyses of Paraoxon, a toxic insecticide, in the forms of both colloidal dispersions and films, and to characterize the surfaces of the films by atomic force microscopy and by dynamic contact angle measurements.

Findings and Conclusions: The glass transition temperature (T_g) of polystyrene (PS) filled with SWCNT grafted with PS of different lengths increased from 99 to 109 ^oC at 6 wt% of SWCNT followed by a plateau. The heat capacity (ΔC_p) at T_g continued to decrease only for the smallest chain length grafted PS nanocomposites. SWCNT/PS nanocomposites had low electrical conductivity and showed no percolation threshold due to the thick polymer coatings. A key finding was that the SWCNT surface can accommodate only a fixed numbers of styrene units. Similar results on change in T_g were obtained for SWCNT/PMMA nanocomposites when molecular weight of matrix (M_{matrix}) $\geq$ molecular weight of grafts (M_{graft}). No change in ΔC_p was observed for SWCNT/PMMA nanocomposites. "W*etting*" to "*dewetting*" occurred $M_{matrix}/M_{graft} \approx 1$. For $M_{matrix} > M_{graft}$, electrical conductivity of nanocomposites reached the value of 10^{-9} S cm^{-1} at 1.0 wt% nanotube loading and had percolation threshold of electrical conductivity at ~0.25 wt% SWCNT. Raman and UV-vis-NIR data confirmed that grafting methods have little effect on inherent electronic properties of SWCNT. A key observation was that the behavior of polymer-SWCNT composites is analogous to polymer thin films containing two different lengths of chemically same polymers. On the other hand, semifluorinated copolymers had hydrophobic and lipophilic properties similar to homopolymers of poly(perfluoroalkyl methacrylates), but were not active in detoxification of Paraoxon. Therefore, semi-fluorinated latexes can either act as phase transfer catalysts for hydrolysis of organophosporous compounds or repel the compound, but cannot do both.

ADVISER'S APPROVAL: Warren T. Ford